

AD A 056293

12
P.S.

LEVEL II

AD-E430054

TECHNICAL REPORT ARBRL-TR-02064

TWO-DIMENSIONAL COMPUTATIONS OF OBLIQUITY
EFFECTS ON THE PENETRATION PROCESS

V. Kucher

May 1978

DDC
RECEIVED
JUL 18 1978
RCB



US ARMY ARMAMENT RESEARCH AND DEVELOPMENT COMMAND
BALLISTIC RESEARCH LABORATORY
ABERDEEN PROVING GROUND, MARYLAND

Approved for public release; distribution unlimited.

16 005

Destroy this report when it is no longer needed.
Do not return it to the originator.

Secondary distribution of this report by originating
or sponsoring activity is prohibited.

Additional copies of this report may be obtained
from the National Technical Information Service,
U.S. Department of Commerce, Springfield, Virginia
22161.

The findings in this report are not to be construed as
an official Department of the Army position, unless
so designated by other authorized documents.

*The use of trade names or manufacturers' names in this report
does not constitute endorsement of any commercial product.*

UNCLASSIFIED

SECURITY CLASSIFICATION OF THIS PAGE (When Data Entered)

REPORT DOCUMENTATION PAGE		READ INSTRUCTIONS BEFORE COMPLETING FORM	
1. REPORT NUMBER TECHNICAL REPORT ARBRL-TR-02064	2. GOVT ACCESSION NO.	3. RECIPIENT'S CATALOG NUMBER	
4. TITLE (and Subtitle) TWO-DIMENSIONAL COMPUTATIONS OF OBLIQUITY EFFECTS ON THE PENETRATION PROCESS		5. TYPE OF REPORT & PERIOD COVERED FINAL	
7. AUTHOR(s) V. / Kucher		8. CONTRACT OR GRANT NUMBER(s)	
9. PERFORMING ORGANIZATION NAME AND ADDRESS U. S. Army Ballistic Research Laboratory (ATTN: DRDAR-BLT) Aberdeen Proving Ground, MD 21005		10. PROGRAM ELEMENT, PROJECT, TASK AREA & WORK UNIT NUMBERS 1L161102AH43	
11. CONTROLLING OFFICE NAME AND ADDRESS U. S. Army Armament Research & Development Command U. S. Army Ballistic Research Laboratory (ATTN: DRDAR-BL) Aberdeen Proving Ground, MD 21005		12. REPORT DATE MAY 1978	
14. MONITORING AGENCY NAME & ADDRESS (if different from Controlling Office)		13. NUMBER OF PAGES 149	
		15. SECURITY CLASS. (of this report) UNCLASSIFIED	
16. DISTRIBUTION STATEMENT (of this Report) Approved for public release; distribution unlimited.		15a. DECLASSIFICATION/DOWNGRADING SCHEDULE	
17. DISTRIBUTION STATEMENT (of the abstract entered in Block 20, if different from Report) B			
18. SUPPLEMENTARY NOTES			
19. KEY WORDS (Continue on reverse side if necessary and identify by block number) Penetration Mechanics Hypervelocity Impact Shaped-Charge Penetration Two-Dimensional Computer Code Eulerian Computer Code			
20. ABSTRACT (Continue on reverse side if necessary and identify by block number) A two-dimensional computer study, simulating the oblique impact of a copper rod on a steel target, was made of the edge-on impact of a semi-infinite copper plate on an infinite steel plate. The obliquity angles included 0°, 45°, 60°, and 75°. Obliquity effects are noted in the pressure peaks, penetration histories, hole or cut growth, and penetrator-target deformations.			

TABLE OF CONTENTS

	Page
LIST OF ILLUSTRATIONS.	5
I. INTRODUCTION	7
II. COMPUTER CODE.	7
III. PENETRATOR-TARGET CONFIGURATION.	8
IV. COMPUTATIONAL GRID	8
V. ONE-DIMENSIONAL THEORY	9
VI. COMPUTER RESULTS	9
A. Description of Graphical Output.	9
B. 0° Obliquity	9
C. 45° Obliquity.	10
D. 60° Obliquity.	11
E. 75° Obliquity.	12
VII. DISCUSSION	12
ACKNOWLEDGMENTS.	13
DISTRIBUTION LIST.	147

DATE		✓
BY		
DISTRIBUTION		
Dist.	APPROV.	SERIAL
A		

LIST OF ILLUSTRATIONS

Figure		Page
1.	Computational Grid with an Outline of the Penetrator-Target Configuration.	15
2-25.	Pressure Field and Penetrator-Target Deformation for 0° Oblique Impact	16-39
26.	Comparison of Penetration Histories for 0° Oblique Impact.	40
27.	Comparison of Hole Growth for 0° Oblique Impact	41
28-57.	Pressure Field and Penetrator-Target Deformation for 45° Oblique Impact.	42-71
58.	Penetration History for 45° Oblique Impact.	72
59.	Growth of the Front Face Cut for 45° Oblique Impact . . .	73
60-89.	Pressure Field and Penetrator-Target Deformation for 60° Oblique Impact.	74-103
90.	Penetration History for 60° Oblique Impact.	104
91.	Growth of the Front Face Cut for 60° Oblique Impact . . .	105
92-129.	Pressure Field and Penetrator-Target Deformation for 75° Oblique Impact.	106-143
130.	Penetration History for 75° Oblique Impact.	144
131.	Growth of the Front Face Cut for 75° Oblique Impact . . .	145

I. INTRODUCTION

It would be of considerable value for an armor designer to be familiar with the details of the phenomena that occur when a long, slender rod impacts at hypervelocity upon an oblique target. Details of this three-dimensional problem could be obtained by using hydrodynamic computer codes; however, at this time, three-dimensional codes are just starting to be productive.^{1,2,3,4,5} In this report, a two-dimensional hydrodynamic code was used to treat the three-dimensional problem of oblique impact as a two-dimensional oblique impact problem by representing the semi-infinite rod by a semi-infinite plate striking the target edge-on. Since the rod diameters in this report and in References 1-5 are different, a comparison of the results of the two studies was not made.

Although the pressure history in the penetrator-target configuration material will be considerably different for the two and three-dimensional treatments of the oblique impact problem, the material flow obtained from the two-dimensional treatment could provide some details of the penetration process that might be useful in improving armor design. Through the use of the tracer particle option available in the code, the flow of penetrator and target materials can be observed for various obliquities. The material in this report will be used for comparisons with three-dimensional computations when they become available.

II. COMPUTER CODE

The DORF-9 code⁶ was used in this study. The code is a continuous, two-dimensional, multimaterial, Eulerian, hydrodynamic code coupled with

1. Wallace E. Johnson, "Three-Dimensional Computations on Penetrator-Target Interactions," Ballistic Research Laboratory Contractor Report No. 338, April 1977. (AD #A041058)
2. W. Johnson and V. Kucher, "Three-Dimensional Computations, Volume I: 30° Oblique Impact," Ballistic Research Laboratory Contractor Report No. 344, July 1977. (AD #A043295)
3. W. Johnson and V. Kucher, "Three-Dimensional Computations, Volume II: 45° Oblique Impact," Ballistic Research Laboratory Contractor Report No. 354, Nov 1977. (AD #A051296)
4. W. Johnson and V. Kucher, "Three-Dimensional Computations, Volume III: 60° Oblique Impact," Ballistic Research Laboratory Contractor Report ARBRL-CR-355, Dec 1977. (AD #A051350)
5. W. Johnson and V. Kucher, "Three-Dimensional Computations, Volume IV: 77.5° Oblique Impact," Ballistic Research Laboratory Contractor Report ARBRL-CR-356, Dec 1977. (AD #A051092)
6. W. E. Johnson, "Development and Application of Computer Programs Related to Hypervelocity Impact," Systems, Science and Software, SSR-749, AD 889143, July 1971.

an elastic-plastic strength model. An option of cylindrically symmetric (r,z) or Cartesian (x,y) coordinates is available in the code. The latter were used in this study. Tracer particles can be used to provide a Lagrangian look to the plotted output. This feature of the code was used to provide material flow patterns during the impact process. The code was run on the high-speed digital computer, BRLESC-2, which is located at the Ballistic Research Laboratory.

III. PENETRATOR-TARGET CONFIGURATION

The penetrator was a semi-infinite copper plate, 6-mm thick, impacting edge-on at 7.5 km/s upon an infinite steel plate, 12.7-mm thick. The obliquity angle, the angle between the normal to the target and the penetrator plate, was varied for each computer run. The obliquity angles were 0°, 45°, 60°, and 75°.

IV. COMPUTATIONAL GRID

The computational grid, which was used for all the obliquity cases in this study, was laid out to cover the cross-sectional region of interest of the penetrator-target configurations. The sides of the penetrator plate were parallel to the y-axis and the initial motion of this plate was in the positive y-direction. The 6-mm thickness of the penetrator was 6 cells wide.⁷ The bottom boundary of the grid was transmittive, allowing the penetrator material to be fed into the grid as a simulation of a semi-infinite plate. The left, top, and right boundaries were also transmittive, simulating an infinite target plate. Figure 1 shows the computational grid with an outline of the 45° penetrator-target configuration. In all the obliquity cases in this study, the initial position of the penetrator plate was the same; the target was rotated relative to the penetrator to obtain the proper obliquities. The overall physical dimensions of the grid was $x = 100$ mm by $y = 250$ mm with a corresponding grid size of 50 by 100 cells.

The cells initially occupied by the penetrator material were given the following input:

1. Density = 8.9 Mg/m³.
2. Pressure = 0.0 Mbar.
3. x-component of velocity = 0.0 km/s.
4. y-component of velocity = 7.5 km/s.
5. Specific internal energy = 0.0 J/g.

Similar conditions were given to the cells initially occupied by the target material except that the density was 7.86 Mg/m³ and the

7. V. Kucher, "Preliminary Computer Computations for Slender Rod Impact Problems," Ballistic Research Laboratory Report No. 1957, Feb 1977. (AD #A036995)

y-component of velocity was zero. The yield stresses in shear that were used for copper and steel were 1.275 and 6.8 kbar, respectively.

V. ONE-DIMENSIONAL THEORY

Using one-dimensional shock wave theory and Tillotson's equation of state⁸ for copper and steel, as used in the DORF-9 code, we find that the region of the penetrator-target interface is shocked to a pressure of 3.0 Mbar, the particle velocity is 3.92 km/s, and the shock wave is moving toward the rear of the target at 9.8 km/s. These conditions prevail in the interface region until the rarefaction waves from the free surfaces of the penetrator reach the center plane of the penetrator. This occurs at 0.34 μ s after impact. This information is used in the analysis of the computer output.

VI. COMPUTER RESULTS

A. Description of Graphical Output

The computer output is presented graphically as pressure fields and their corresponding tracer particle plots. The pressure field is plotted on the xy-plane with the pressure plotted from the center of each cell. An outline of the penetrator-target configuration is shown in each pressure field plot. Figure 2 is an example of a pressure field at the time of initial impact. Corresponding to this figure is Figure 3, a tracer particle plot. The copper material is represented by triangular symbols; the steel, by square symbols. The outline of the penetrator-target configuration was line plotted by using tracer particles which were set on the boundaries of the penetrator and target but were not identified by symbols. When the distance between adjacent tracer particles becomes great, long plotting lines connect these particles as illustrated in Figure 129.

B. 0° Obliquity

The pressure field, penetrator-target outline, and tracer particle positions are shown in Figures 2 and 3 at the instant of impact. At $\frac{1}{4}$ μ s (Figure 4) the maximum pressure is about 4 Mbar compared to the 3 Mbar pressure determined from one-dimensional shock wave theory. Such an overpressure was not evident for the case of a 6-mm copper rod impacting on a 7.5-mm or a 37.5-mm steel plate. These problems were run as two-dimensional, axisymmetric problems.⁹ Other comparisons will be

8. J. H. Tillotson, "Metallic Equations of State for Hypervelocity Impact," Gulf General Atomic, GA-3216, July 1962.

9. V. Kucher, "Computer Study of the Effects of Rod Diameter and Target Thickness on the Penetration Process," Ballistic Research Laboratory Technical Report, ARBRL-TR-02046, 1978.

made to these problems. By $\frac{1}{2} \mu\text{s}$ (Figure 6), the peak pressure has dropped to 2.5 Mbar since the rarefaction wave from the free surfaces of the penetrator had reached the center plane of the penetrator at $0.34 \mu\text{s}$, as estimated previously. The peak pressure continues to decay for the remainder of the computer run. Between 1 and $1\frac{1}{2} \mu\text{s}$ (Figures 11 and 13, respectively), the shock wave reaches the back surface of the target as evidenced by the bulge on the back surface in Figure 13.

Figure 14 ($2 \mu\text{s}$) shows pressure peaks on either side of the central pressure region. These peaks move to the left and right in the target, away from the central pressure region. At $4 \mu\text{s}$ (Figure 18), another set of pressure peaks, which are at the penetrator-target interface region, have appeared.

Figure 26 shows the time relation for the foremost part of the penetrator for three different impact cases. Two axisymmetric coordinate runs were made using 6-mm copper rods impacting normally on 7.5-mm and 37.5-mm steel plates.⁹ The third case is the 0° obliquity impact which is being reported here. During the first $1\frac{1}{2} \mu\text{s}$, the velocities (slopes of the curves) for the three cases are nearly the same; thereafter the velocity of the 6-mm plate increases due to the pressure release from the back surface located at 12.7 mm. This occurs for the case of the 6-mm rod impacting on a 37.5-mm plate at about $9 \mu\text{s}$. For the case of the 6-mm rod impacting on a 7.5-mm plate, this increase in velocity does not occur until after the front of the penetrator passes the original back surface.

Hole growth is shown in Figure 27 where D is the diameter of the hole at the front surface of the target or the width of the cut across the front surface, and D_0 is the initial rod diameter or penetrator width. The rate at which D increases is greater for the plate penetrator than the rod penetrators.

C. 45° Obliquity

Figures 28-57 show the pressure fields and their corresponding tracer particle position plots with the initial conditions shown in Figures 28 and 29. The shock wave from the impact reaches the back surface of the target at about $2 \mu\text{s}$ as evidenced from the pressure field in Figure 34 and the slight bulge on the back surface in Figure 35. This bulge continues to grow, as shown in the continuous tracer particle plots, and, for the most part, is positioned on the down or left side of the target with respect to the penetrator.

At $1 \mu\text{s}$ (Figure 33) the penetrator material in the vicinity of the interface region is flowing to the up or right side of the target. By $2 \mu\text{s}$ (Figure 35), the left triangular column shows a flow to the left in the interface region. This flow continues to the left for the remainder of the computer run. Figure 45 ($7 \mu\text{s}$) shows the center triangular column

to be flowing leftward in the interface region and continuing leftward for the remainder of the computer run. The right triangular column in the interface region continues its rightward flow for the entire run.

The pressure fields show that, after the shock wave has reached the back surface of the target, most of the pressure region is in the upside of the target or in the foremost part of the penetrator. For example, see Figure 46.

Figure 58 shows a penetration-time relation obtained from measuring the position of the foremost part of the penetrator relative to its initial position as a function of time. For the first 2 or 3 μ s, the penetrator is trying to get a bite on the target. Thereafter, until the penetrator exits the back face of the target, the penetration rate agrees with the estimated one-dimensional particle velocity. The slope of the curve then starts to approach the initial velocity of the penetrator. Note that the "back of the target" is where the center plane of the penetrator intersects the back surface. The left and right sides of the penetrator intersect the back surface, respectively, at 3 mm before and 3 mm after the 21-mm position indicated.

The width, D , of the cut across the front surface of the target as a function of time is shown in Figure 59 where the width is rationalized with respect to the width of the penetrator, D_0 .

D. 60° Obliquity

Figures 60-89 show the pressure fields and their corresponding tracer particle position plots for the 60° oblique impact. The initial conditions are shown in Figures 60 and 61. As evidenced by the bulge on the back surface of the target (Figure 69), the shock wave reached this surface between 2 and 3 μ s. As the penetration process continues, most of the bulge is shown on the down side of the target relative to the penetrator.

The flow of the foremost part of the penetrator is rightward until 4 μ s (Figure 71), when the left triangular column in the interface region bends to the left. The leftward flow begins at about 9 μ s (Figure 81) for the center triangular column.

The pressure fields show that, after the shock wave has reached the back surface of the target, most of the pressure region is in the upside of the target or in the foremost part of the penetrator. For example, see Figure 86.

Figure 90 shows a penetration-time relation obtained from measuring the position of the front of the penetrator, that is penetrating the target, relative to its initial position as a function of time. For the first 4 or 5 μ s, the penetrator is trying to get a bite on the target. Thereafter, until the penetrator exits the back face of the target, the

penetration rate agrees with the estimated one-dimensional particle velocity. The slope of the curve then starts to approach the initial velocity of the penetrator. Note that the "back of the target" is where the center plane of the penetrator intersects the back surface. The left and right sides of the penetrator intersect the back surface, respectively, at 5.2 mm before and 5.2 mm after the 30.6-mm position indicated.

The width, D , of the cut across the front surface of the target as a function of time is shown in Figure 91 where the width is rationalized with respect to the width of the penetrator, D_0 .

E. 75° Obliquity

Pressure fields and their corresponding tracer particle position plots for the 75° oblique impact are shown in Figures 92-129. Figures 92 and 93 show the initial conditions. A bulge on the back surface of the target is detected at about 3 μ s (Figure 101), and it continues to grow for the remainder of the run.

For the first 6 or 7 μ s (Figures 95-109), the front of the penetrator flows in a rightward direction; at about 7 μ s (Figure 109), the top of the left triangular column starts to bend to the left, followed by the center column at 14 μ s (Figure 119) and the right column at 22 μ s (Figure 127).

The pressure fields show that, after the shock wave has reached the back surface of the target, most of the pressure region is in the upside of the target or in the foremost part of the penetrator. For example, see Figure 112.

Figure 130 shows a penetration-time relation obtained from measuring the position of the front of the penetrator, that is penetrating the target, relative to its initial position as a function of time. For the first 6 or 7 μ s, the penetrator is trying to get a bite on the target. Thereafter, until the penetrator exits the back face of the target, the penetration rate agrees with the estimated one-dimensional particle velocity. The slope of the curve then starts to approach the initial velocity of the penetrator. Note that the "back of the target" is where the center plane of the penetrator intersects the back surface. The left and right sides of the penetrator intersect the back surface, respectively, at 11.2 mm before and 11.2 mm after the 60.6-mm position indicated.

The width, D , of the cut across the front surface of the target as a function of time is shown in Figure 131 where the width is rationalized with respect to the width of the penetrator, D_0 .

VII. DISCUSSION

From observations of the graphs of penetrator-target deformations

and pressure fields, several trends are noted.

The pressure field plots for 0° , 45° , 60° , and 75° oblique impacts show that, immediately after impact, a pressure pulse moves normally toward the back face of the target and at the same time spreads in the left and right directions in the target. During this period, the pressure peak is greatest for the 0° oblique impact and the least for the 75° oblique impact, except at $\frac{1}{2} \mu s$. After the pressure wave reaches the back face of the target, most of the pressure region is in the upside of the oblique targets and in the foremost part of the penetrator. Now the greatest pressure peak occurs for the 75° oblique impact; the least pressure peak, for the 0° impact.

There are times, such as at $7 \mu s$ (Figures 45, 77, and 109), when the shape of the cut in the oblique targets seems to suggest that the target was impacted normally.

A bulge forms at the back face of the target after the shock wave reaches this surface. The approximate times of the initial formation of the bulges for the 0° , 45° , 60° , and 75° oblique impacts are between 1 and $1\frac{1}{2}$, 1 and 2, 2 and 3, and 2 and 3 μs , respectively. At any given time, the amplitude of the bulge decreases with increasing obliquity angles.

ACKNOWLEDGEMENTS

The author acknowledges Allen Delp, Eugene Cudmore, and Terry Lough for their computer and graphical support.

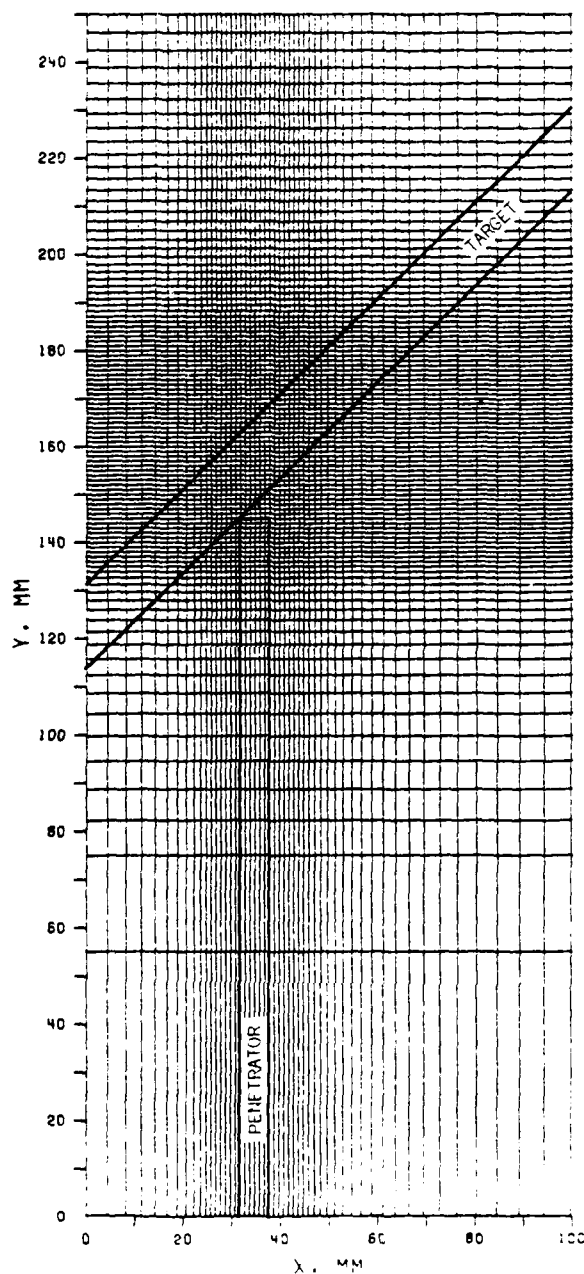


Figure 1. Computational Grid with an Outline of the Penetrator-Target Configuration

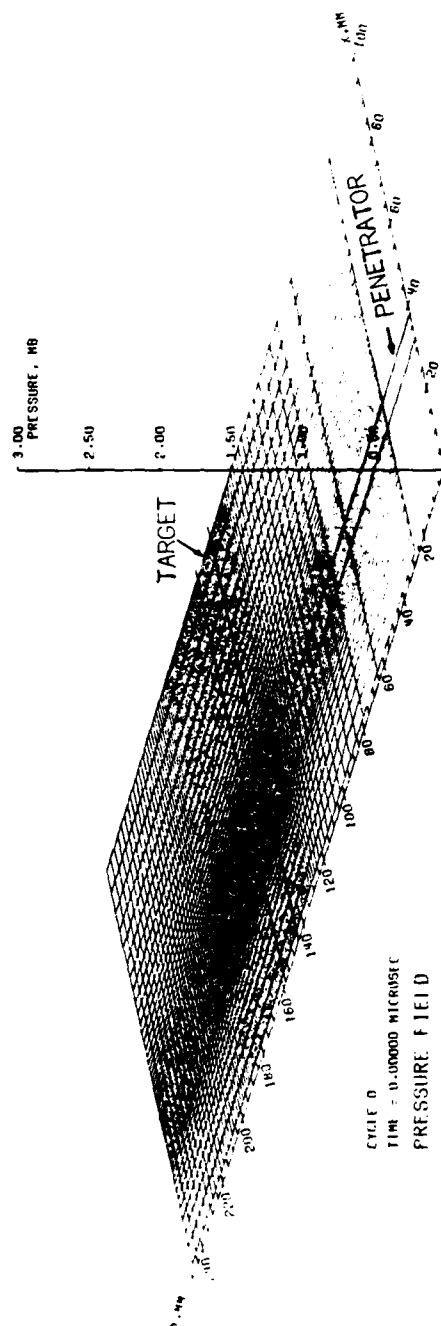


Figure 2. Pressure Field for 0° Oblique Impact

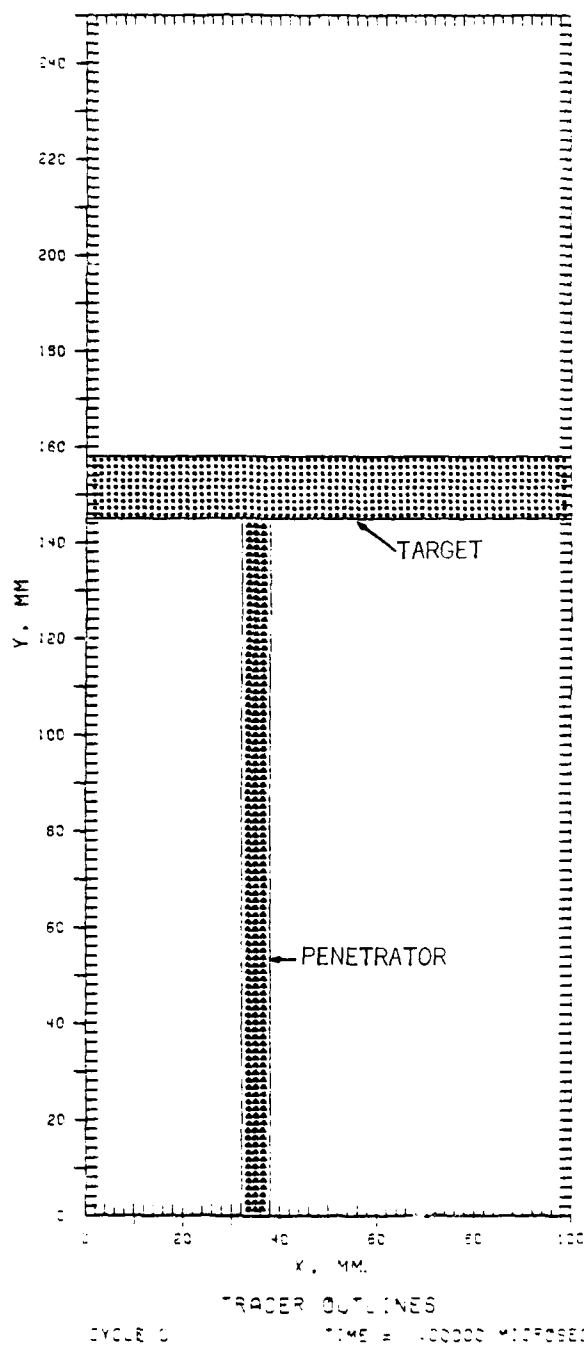


Figure 3. Penetrator-Target Deformation for 0° Oblique Impact

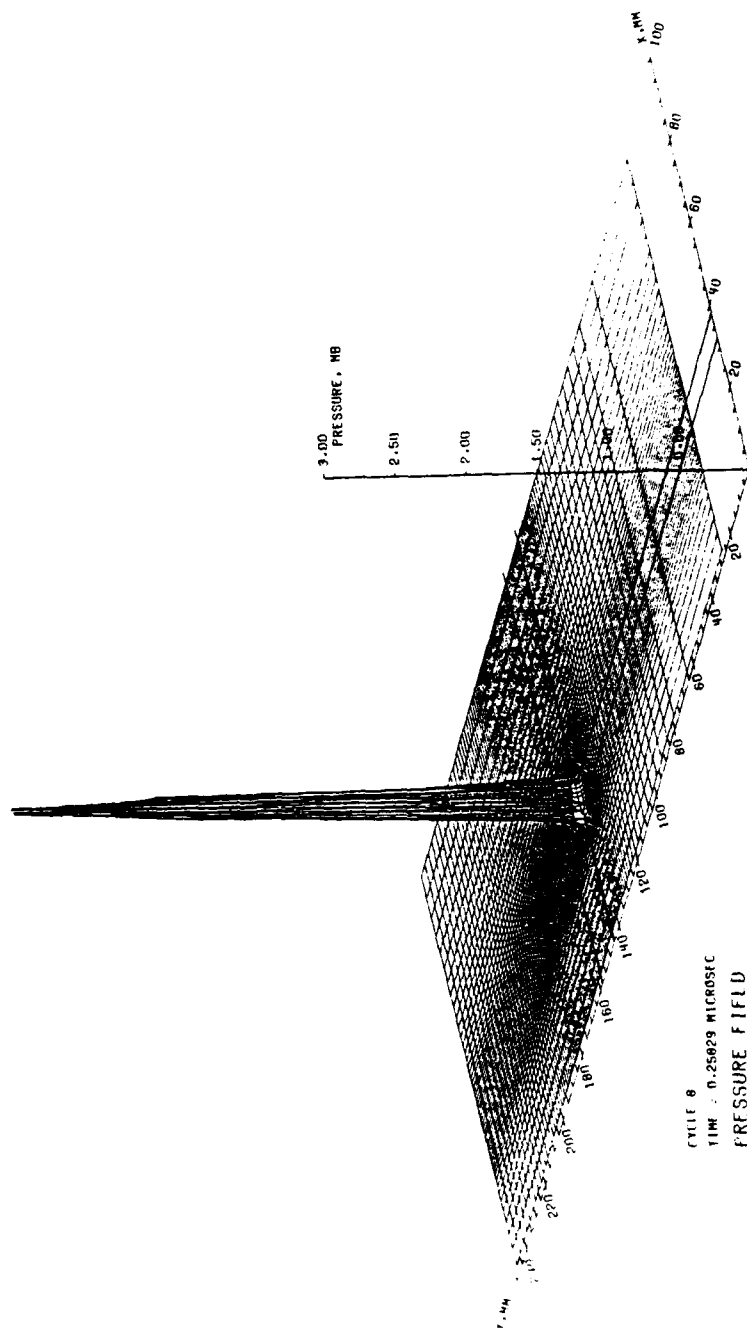


Figure 4. Pressure Field for 0° Oblique Impact

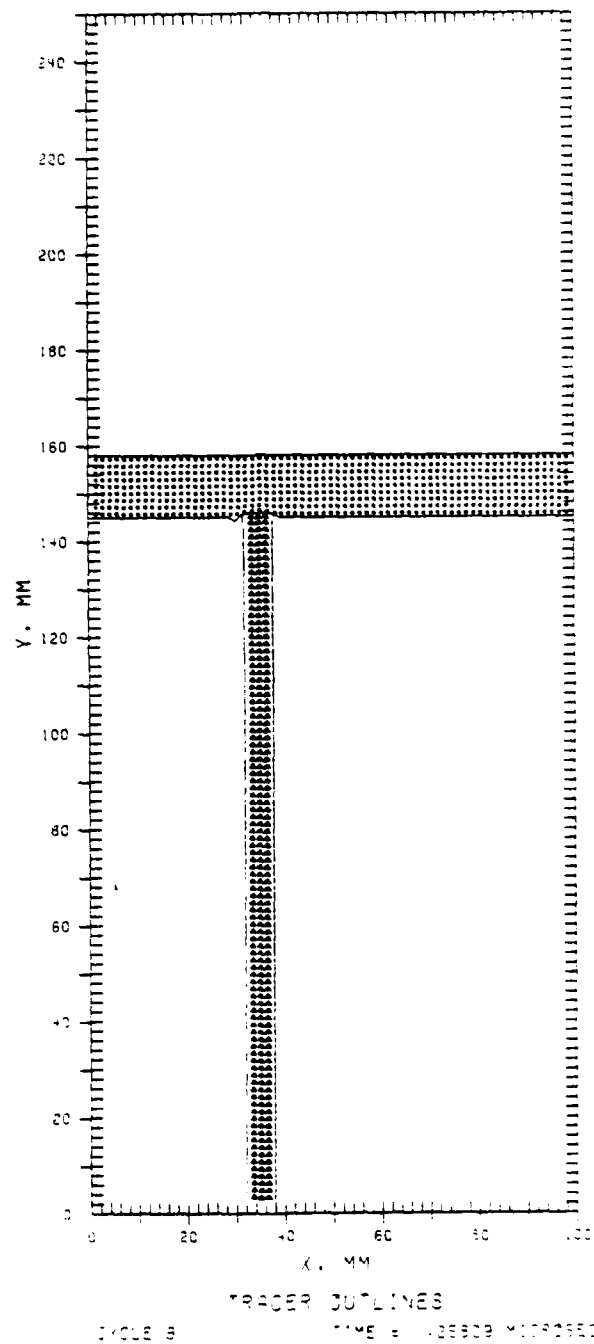


Figure 5. Penetrator-Target Deformation for 0° Oblique Impact

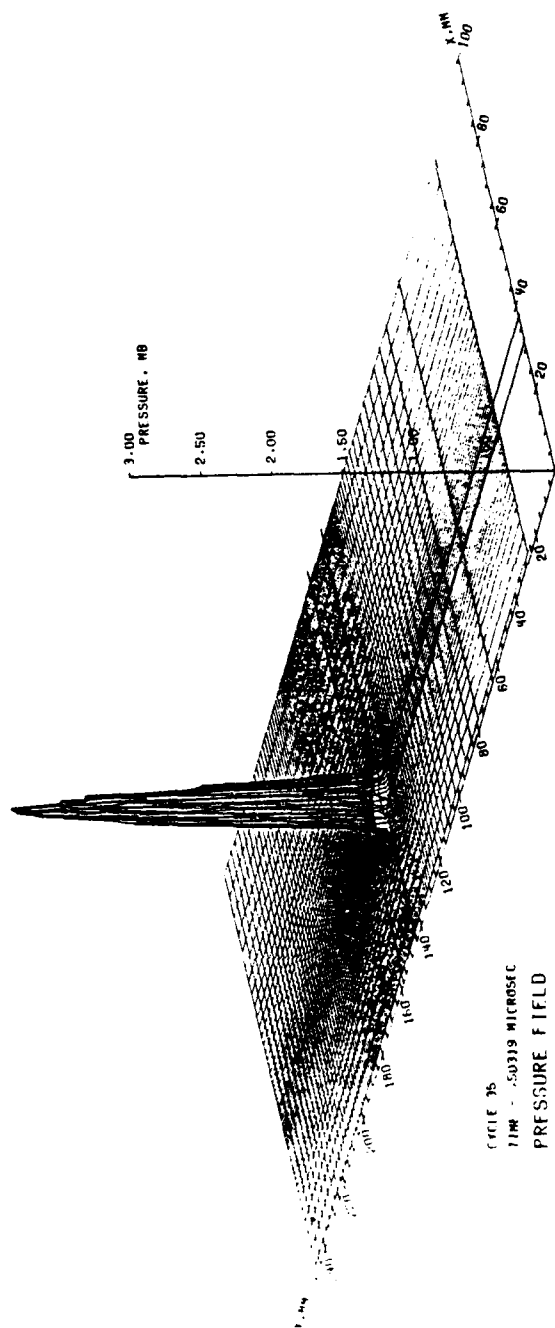


Figure 6. Pressure Field for 0° Oblique Impact

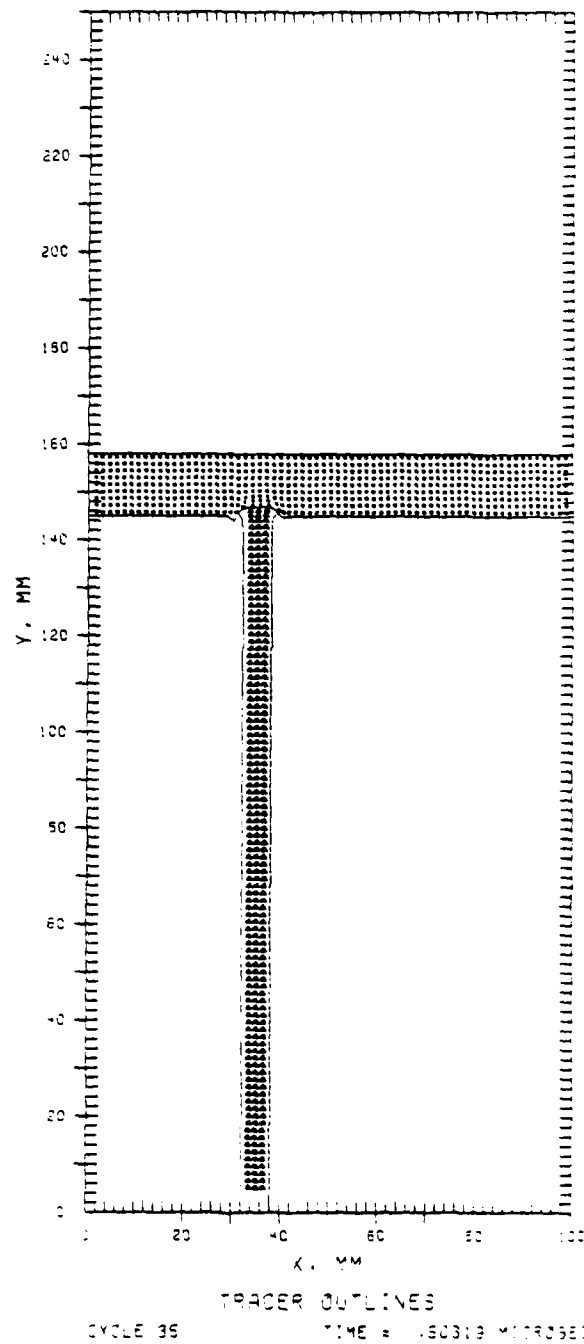


Figure 7. Penetrator-Target Deformation for 0° Oblique Impact

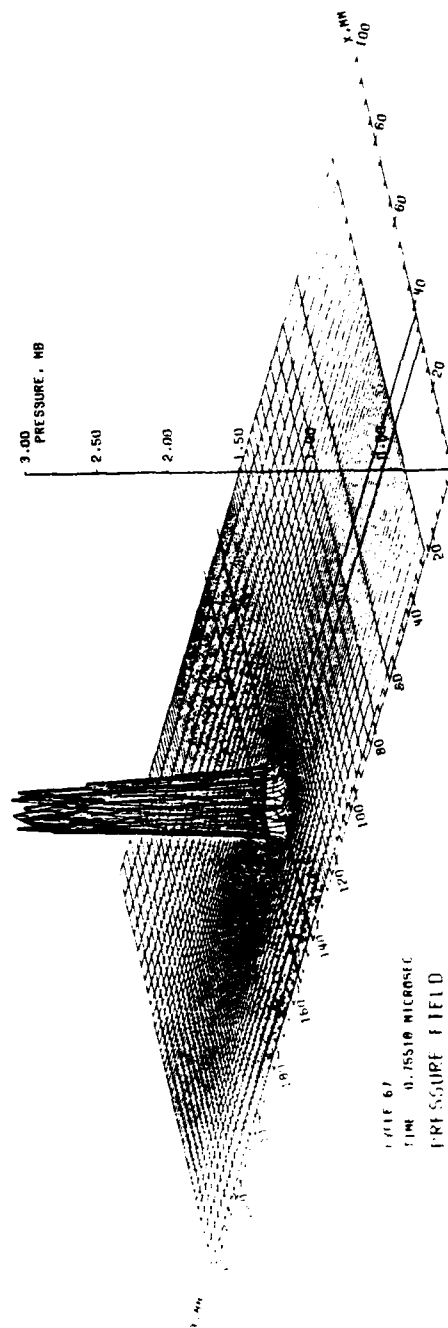


Figure 8. Pressure Field for 0° Oblique Impact

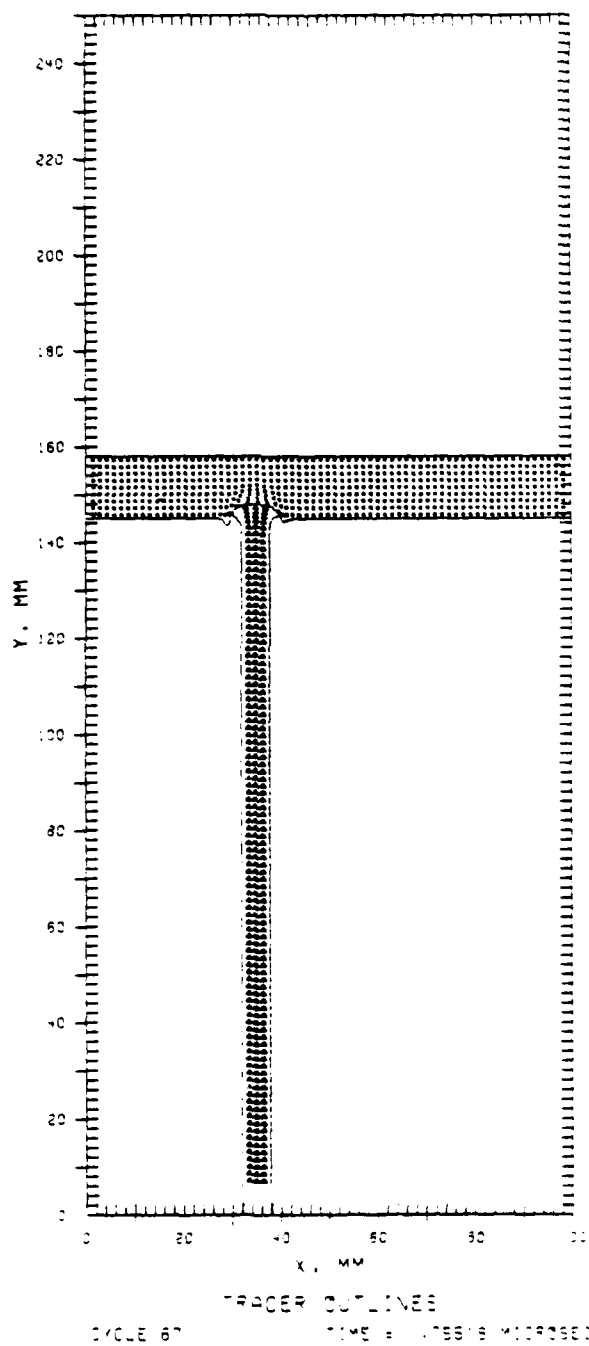


Figure 9. Penetrator-Target Deformation for 0° Oblique Impact

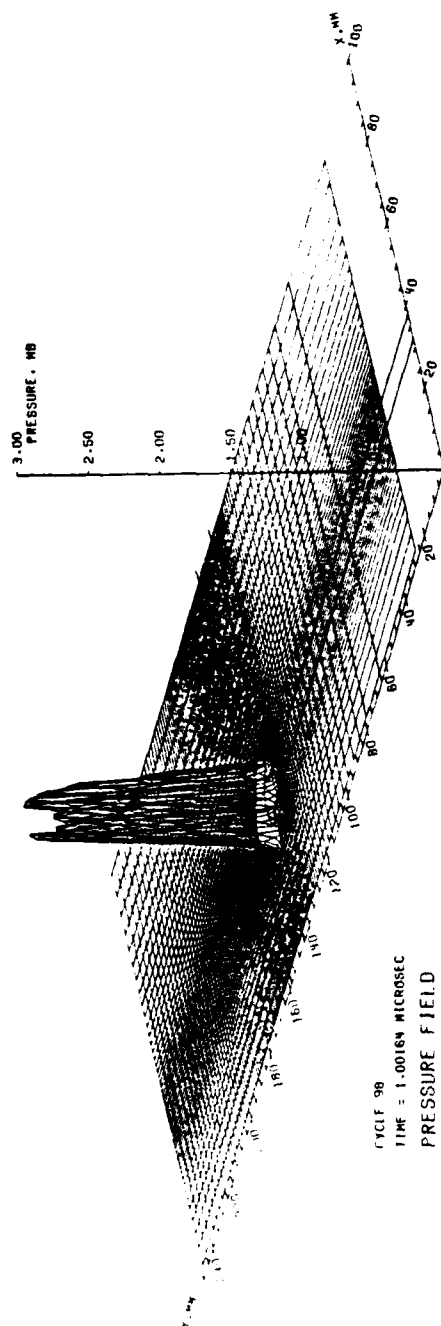


Figure 10. Pressure Field for 0° Oblique Impact

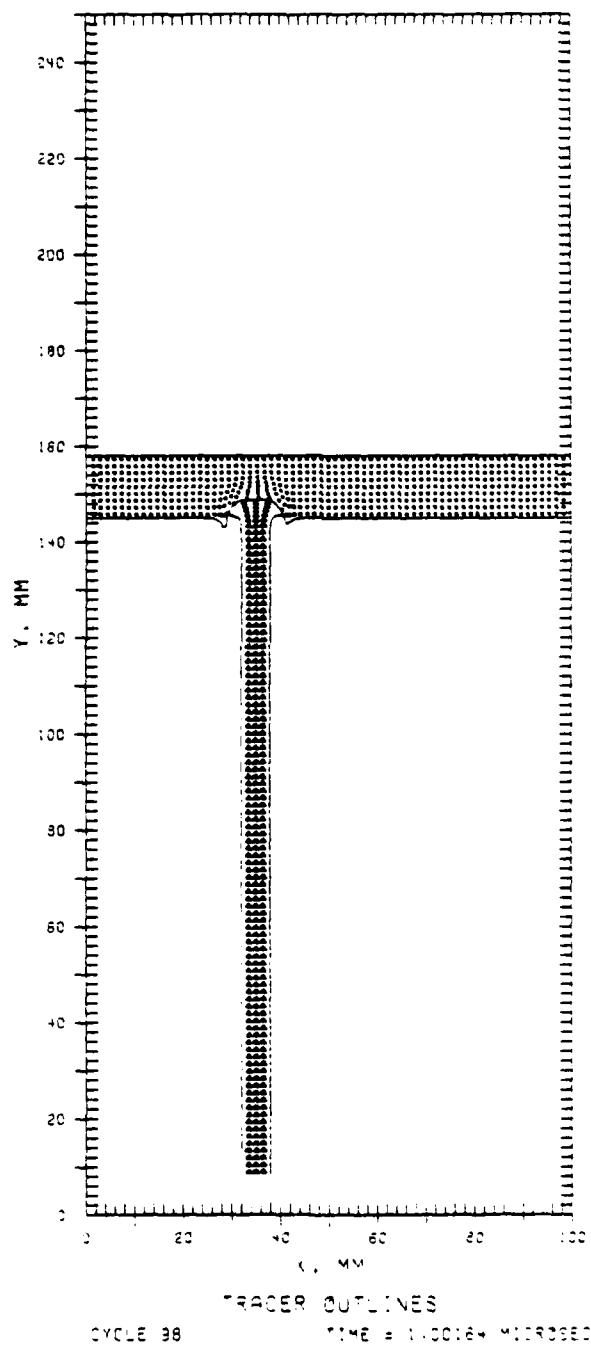


Figure 11. Penetrator-Target Deformation for 0° Oblique Impact

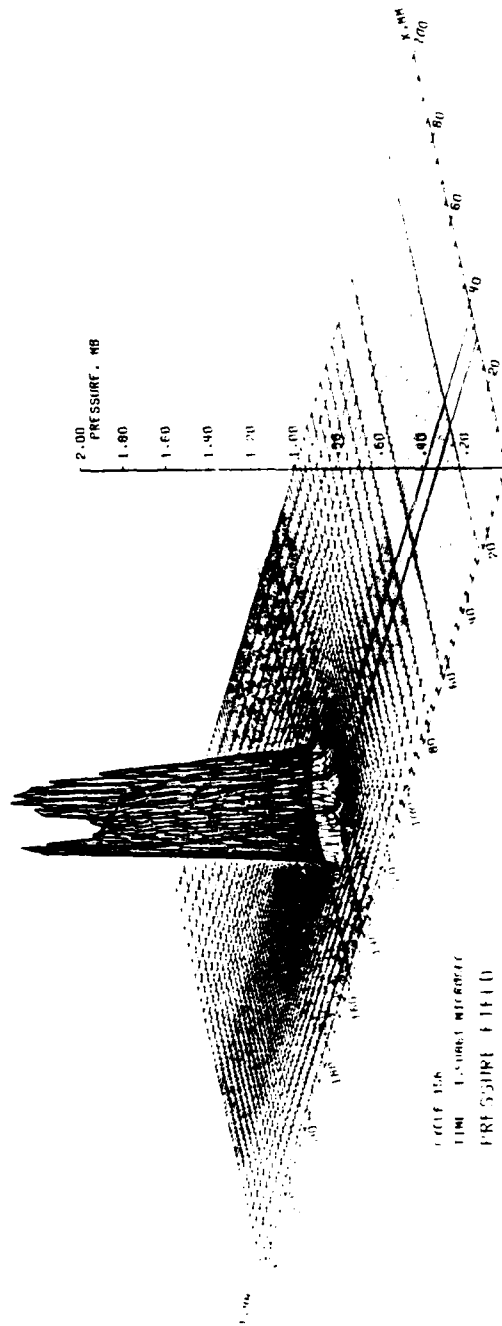


Figure 12. Pressure Field for 0° Oblique Impact

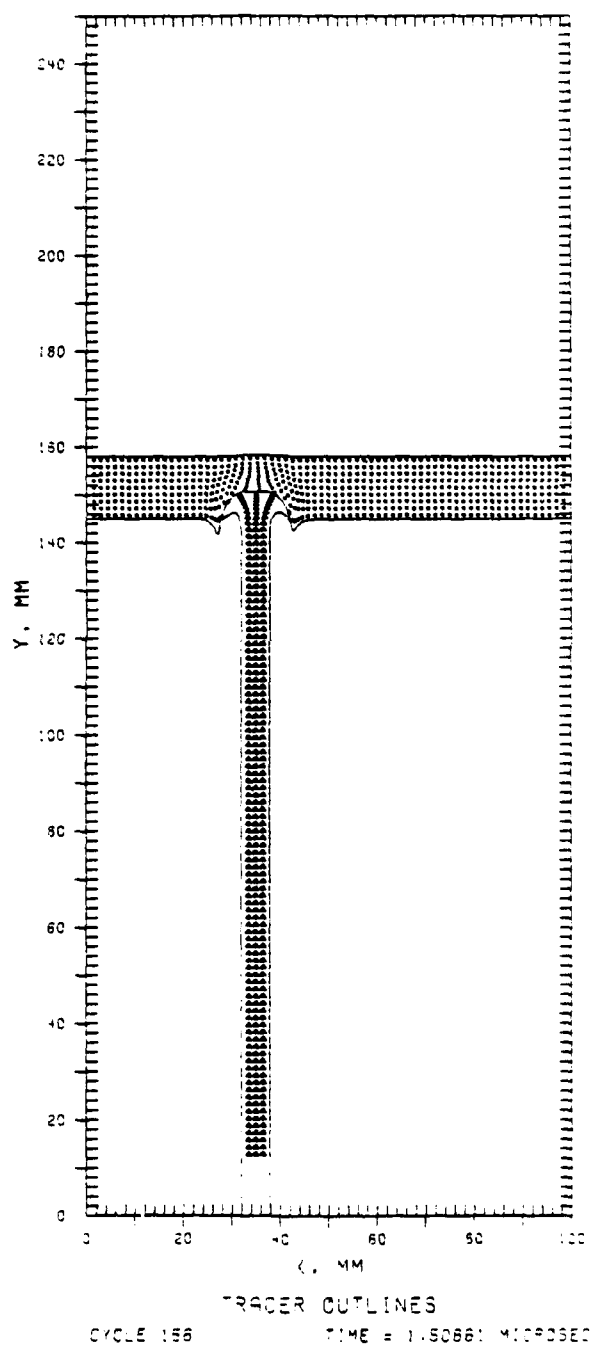


Figure 13. Penetrator-Target Deformation for 0° Oblique Impact

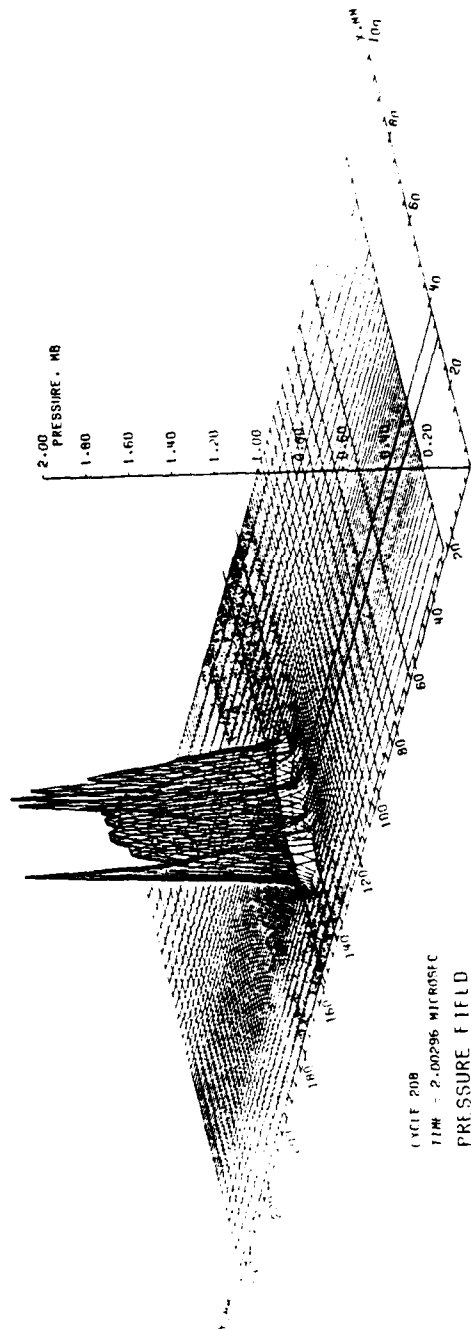


Figure 14. Pressure Field for 0° Oblique Impact

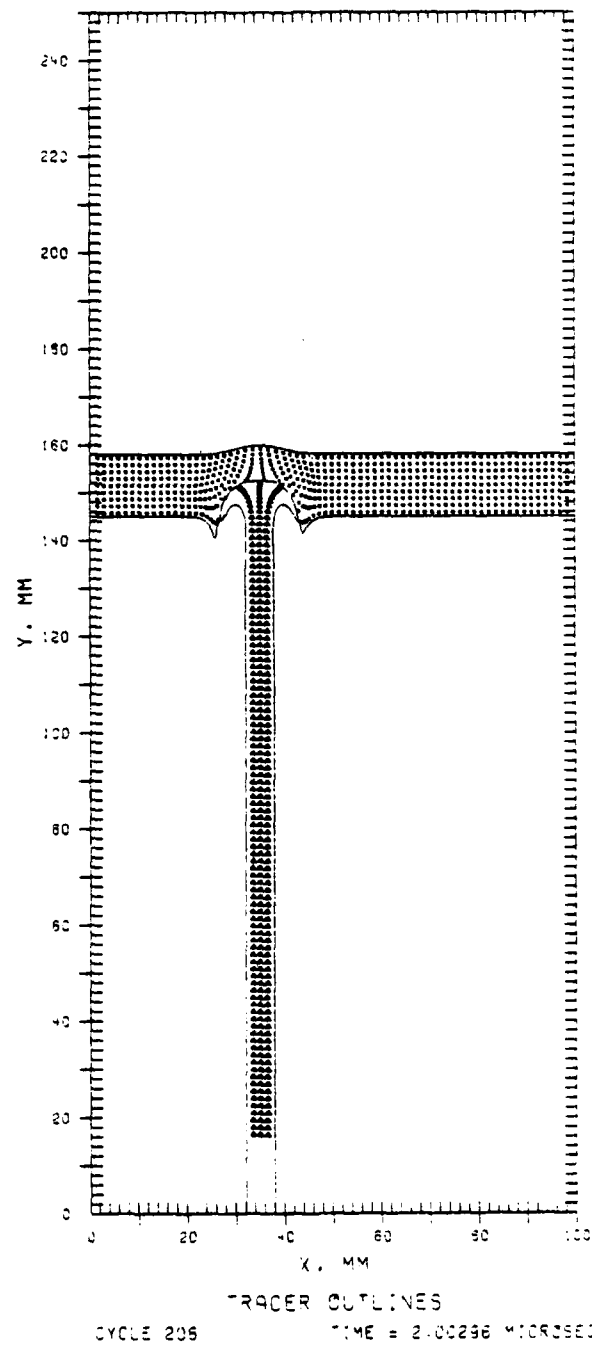


Figure 15. Penetrator-Target Deformation for 0° Oblique Impact

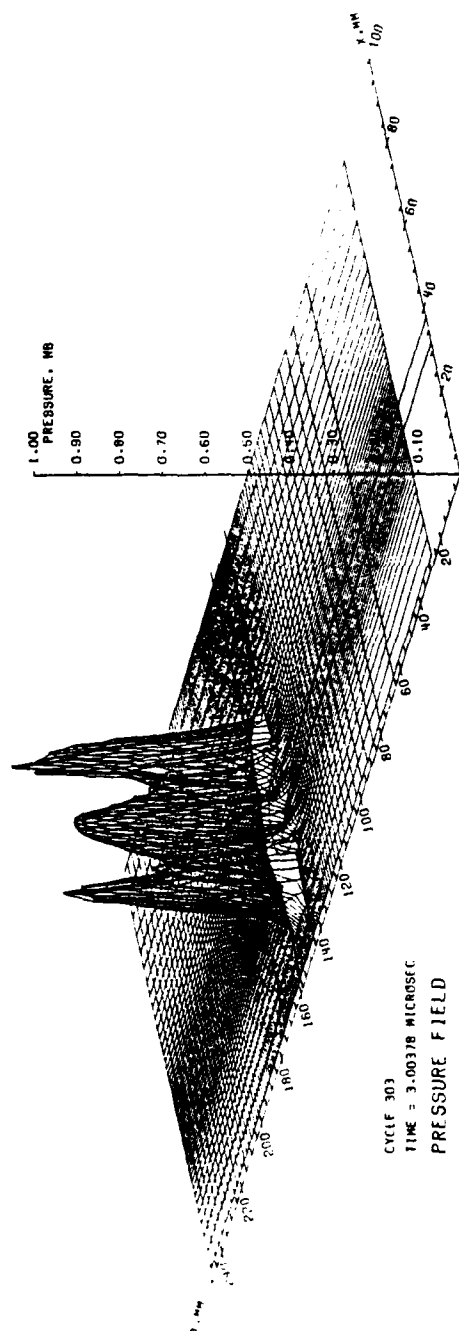


Figure 16. Pressure Field for 0° Oblique Impact

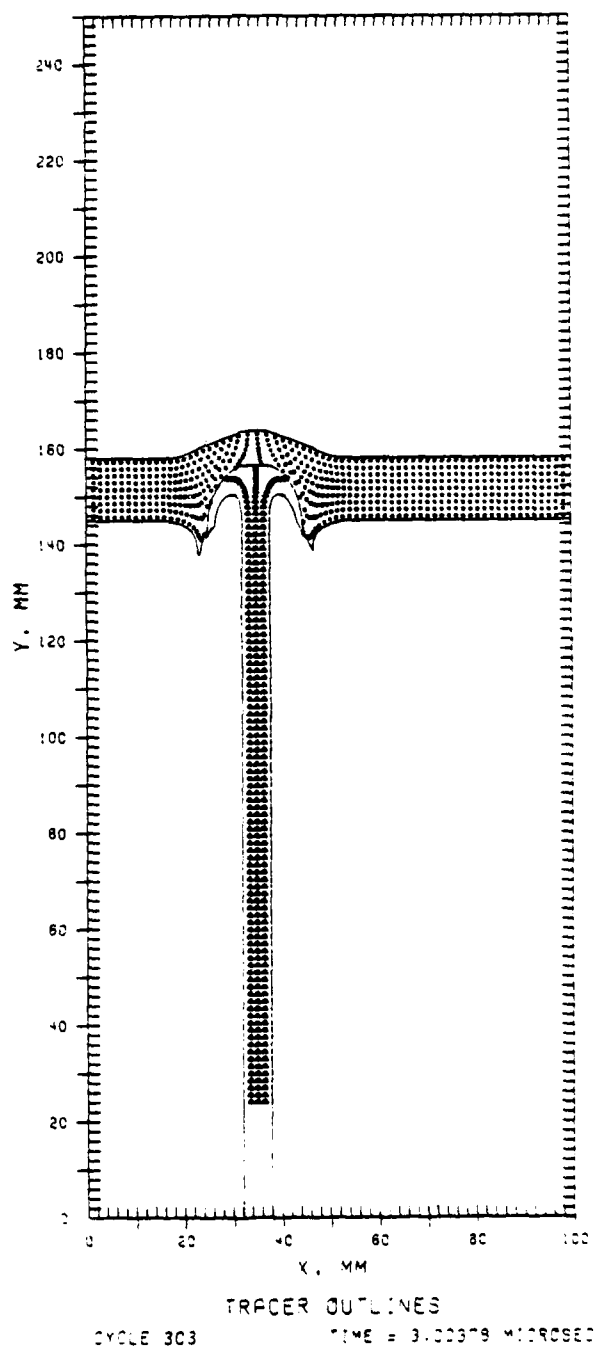


Figure 17. Penetrator-Target Deformation for 0° Oblique Impact

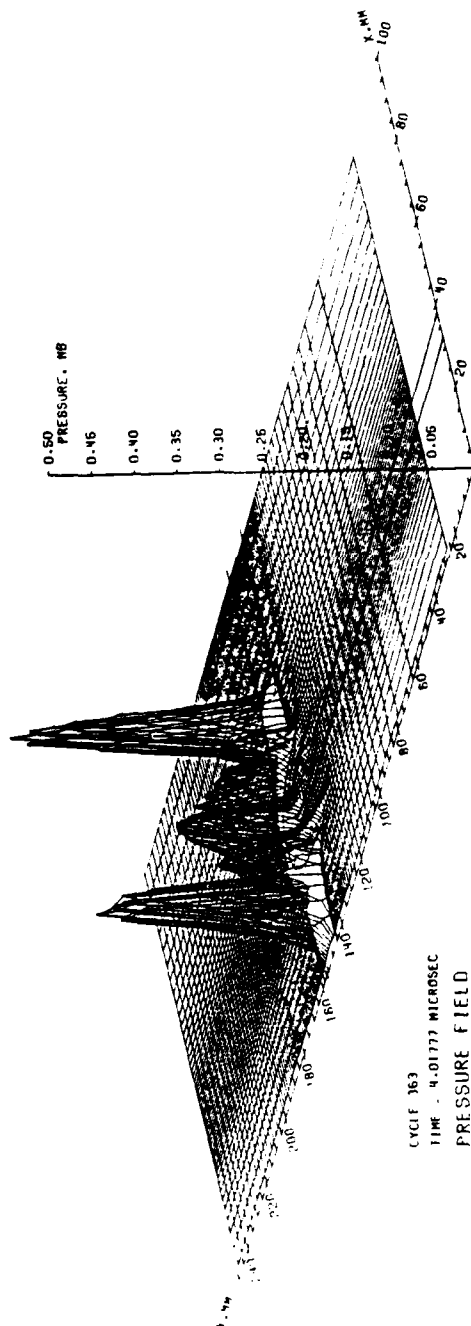


Figure 18. Pressure Field for 0° Oblique Impact

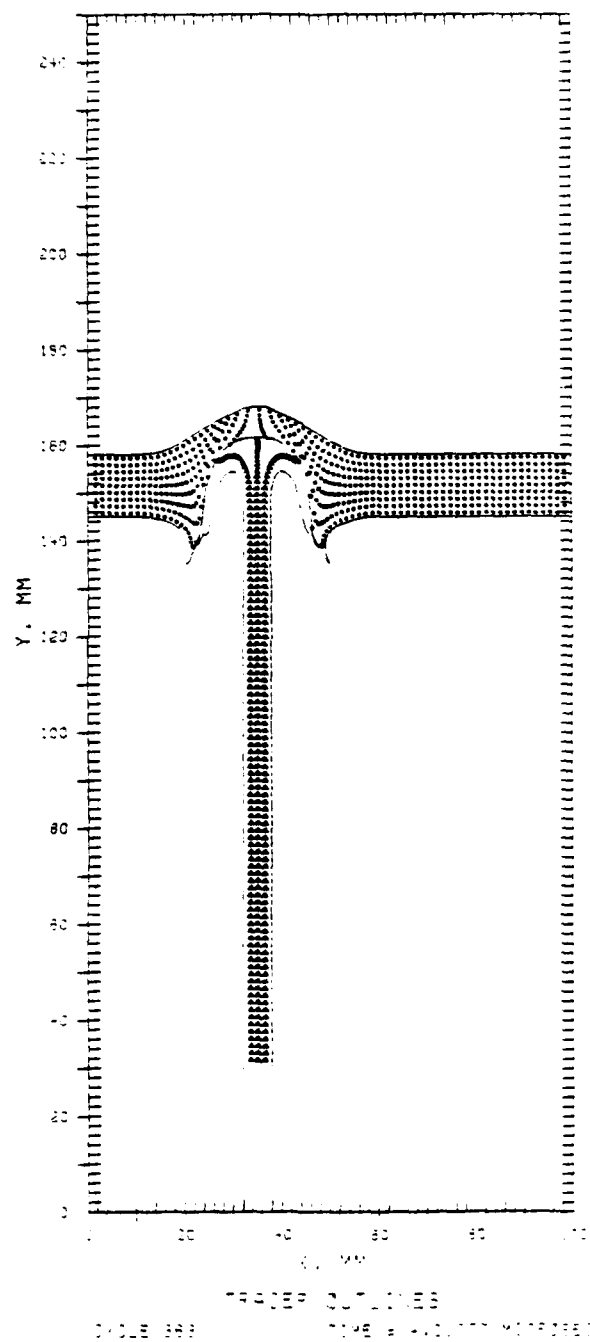


Figure 19. Penetrator-Target Deformation for 0° Oblique Impact

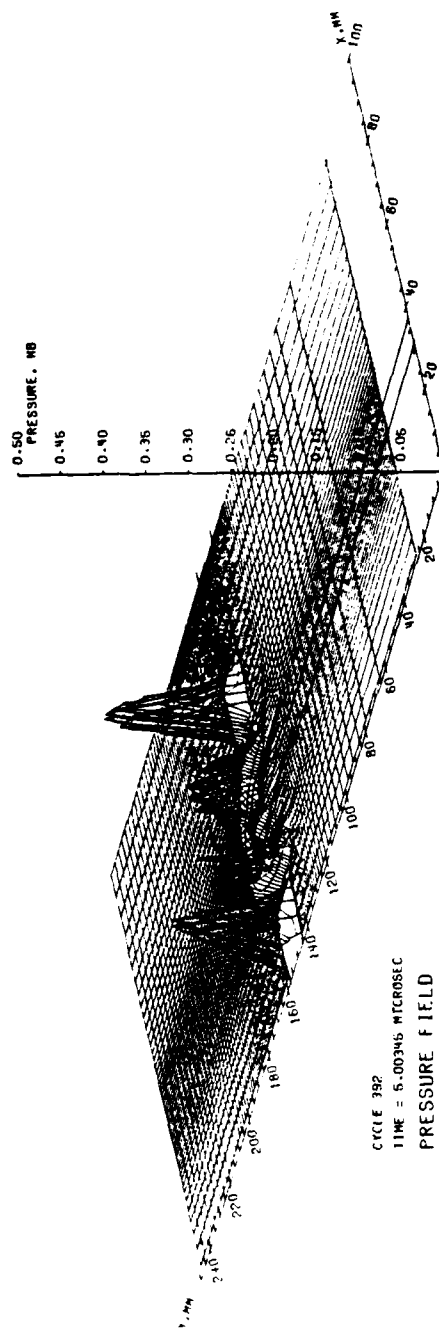


Figure 20. Pressure Field for 0° Oblique Impact

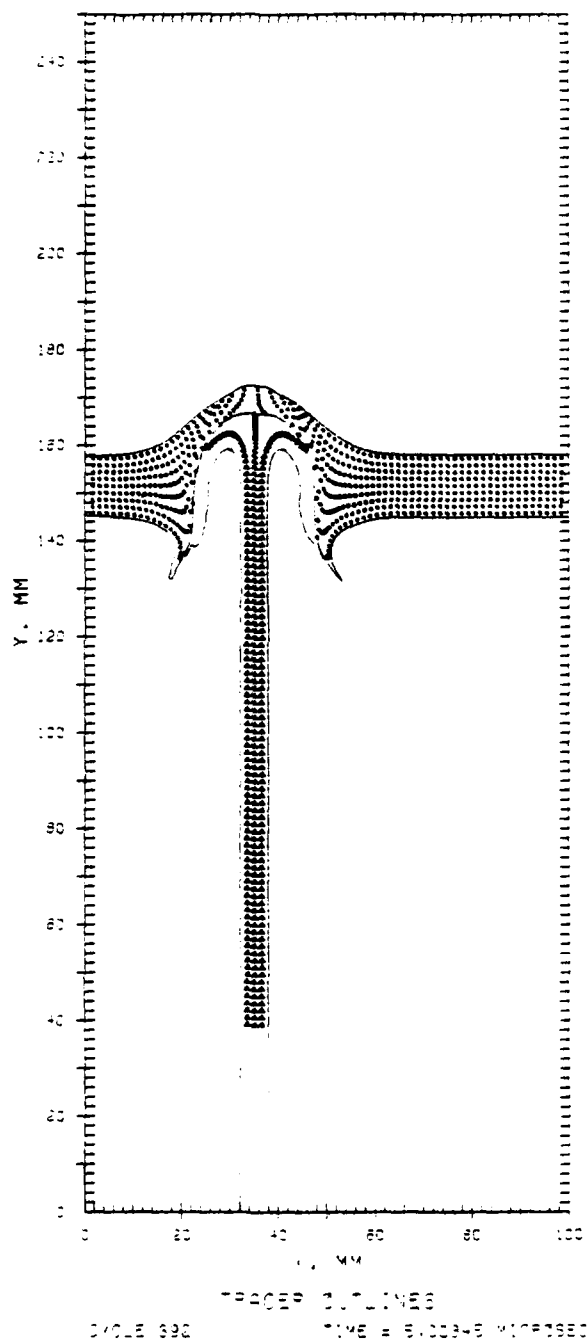


Figure 21. Penetrator-Target Deformation for 0° Oblique Impact

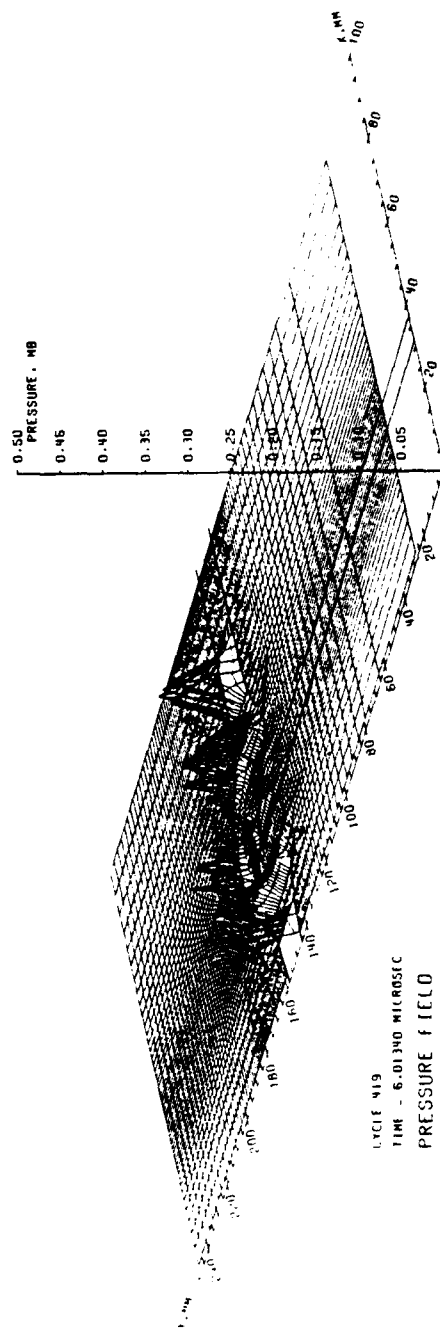


Figure 22. Pressure Field for 0° Oblique Impact

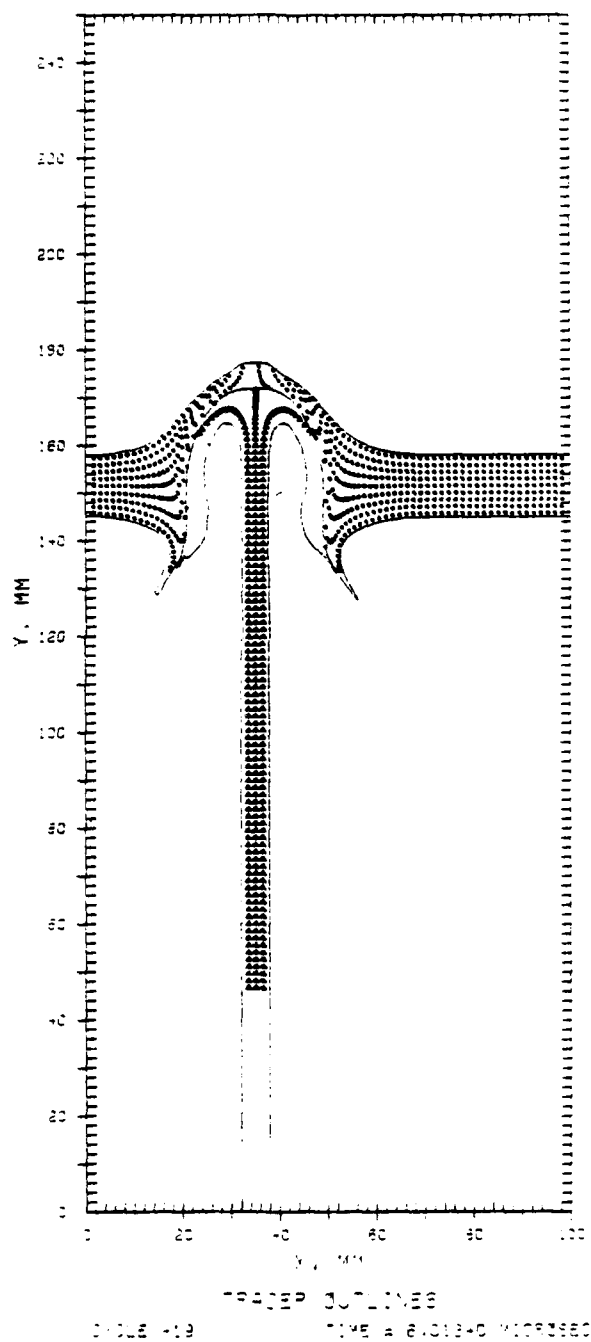


Figure 23. Penetrator-Target Deformation for 0° Oblique Impact

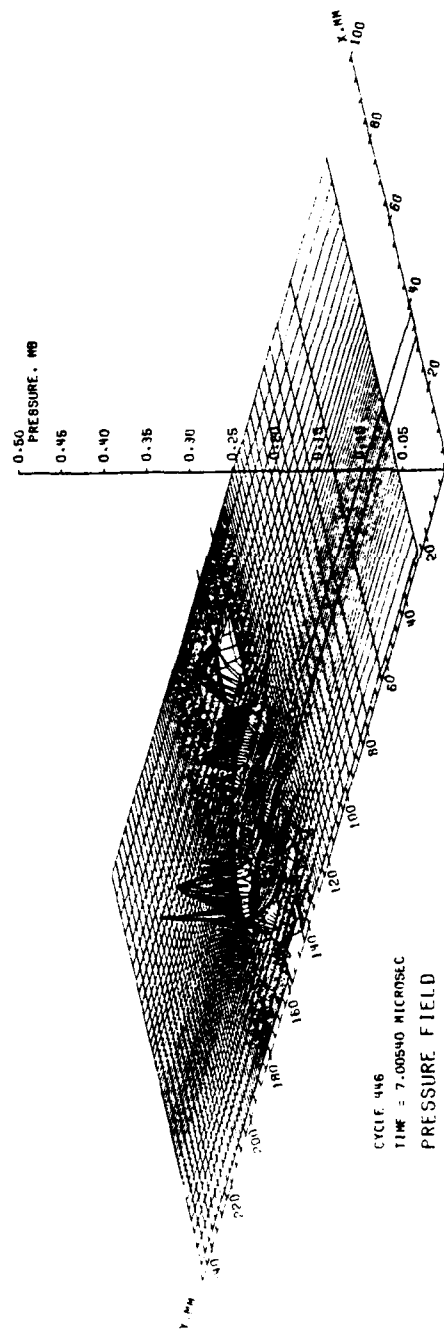


Figure 24. Pressure Field for 0° Oblique Impact

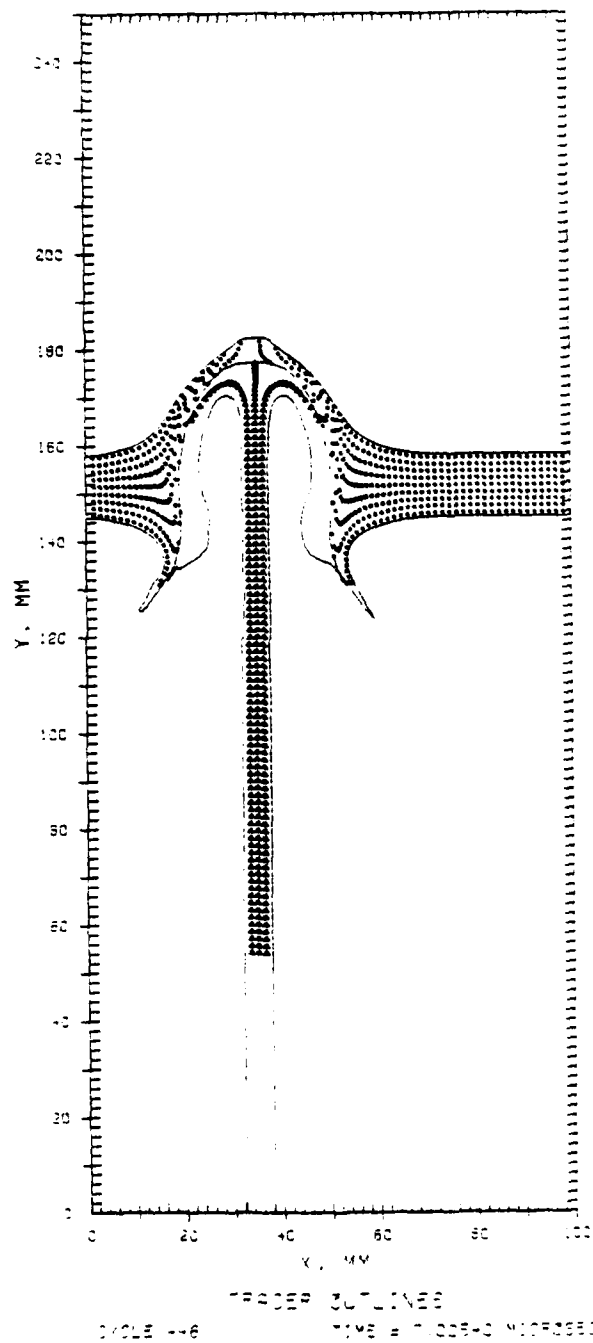


Figure 25. Penetrator-Target Deformation for 0° Oblique Impact

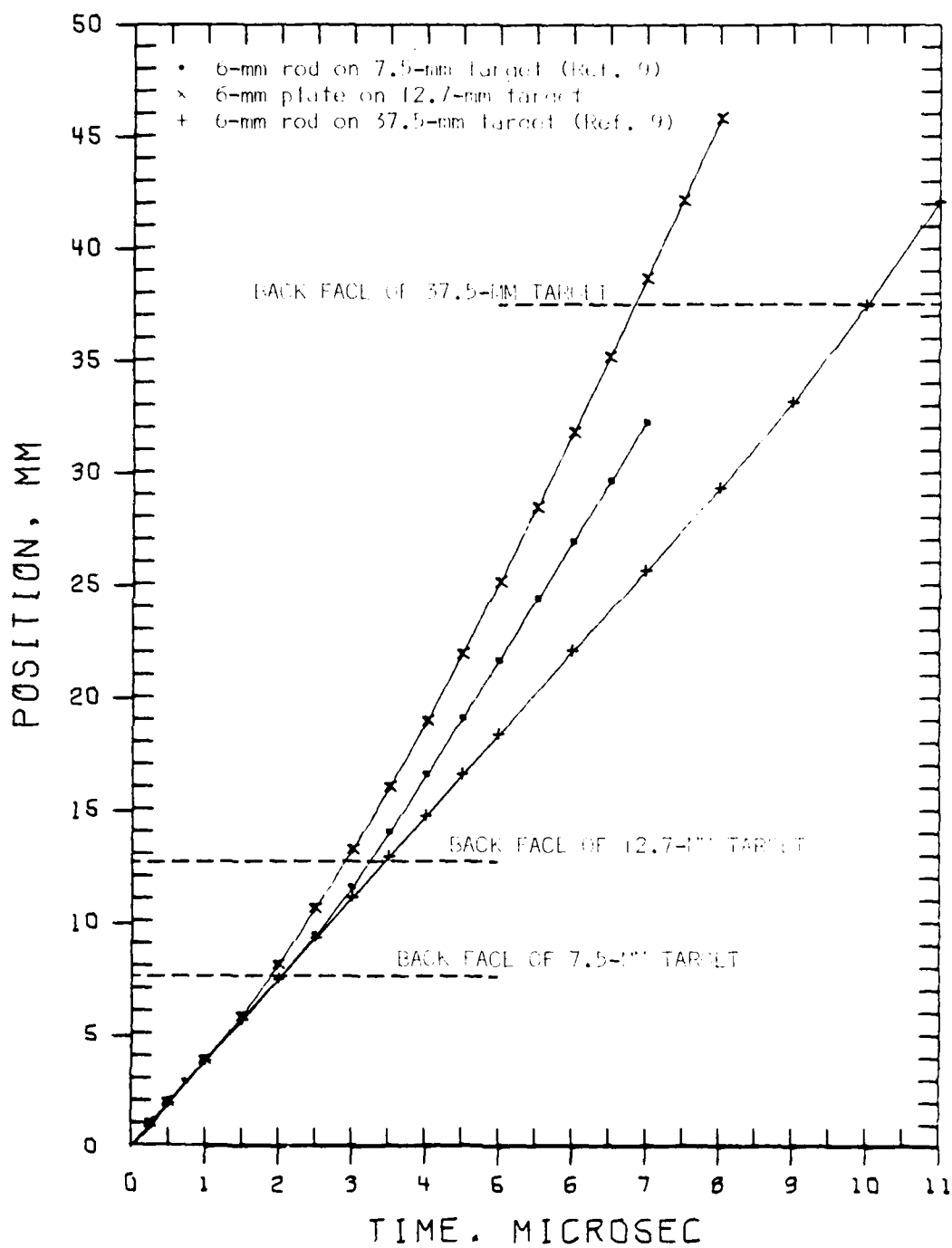


Figure 26. Comparison of Penetration Histories for 0° Oblique Impact

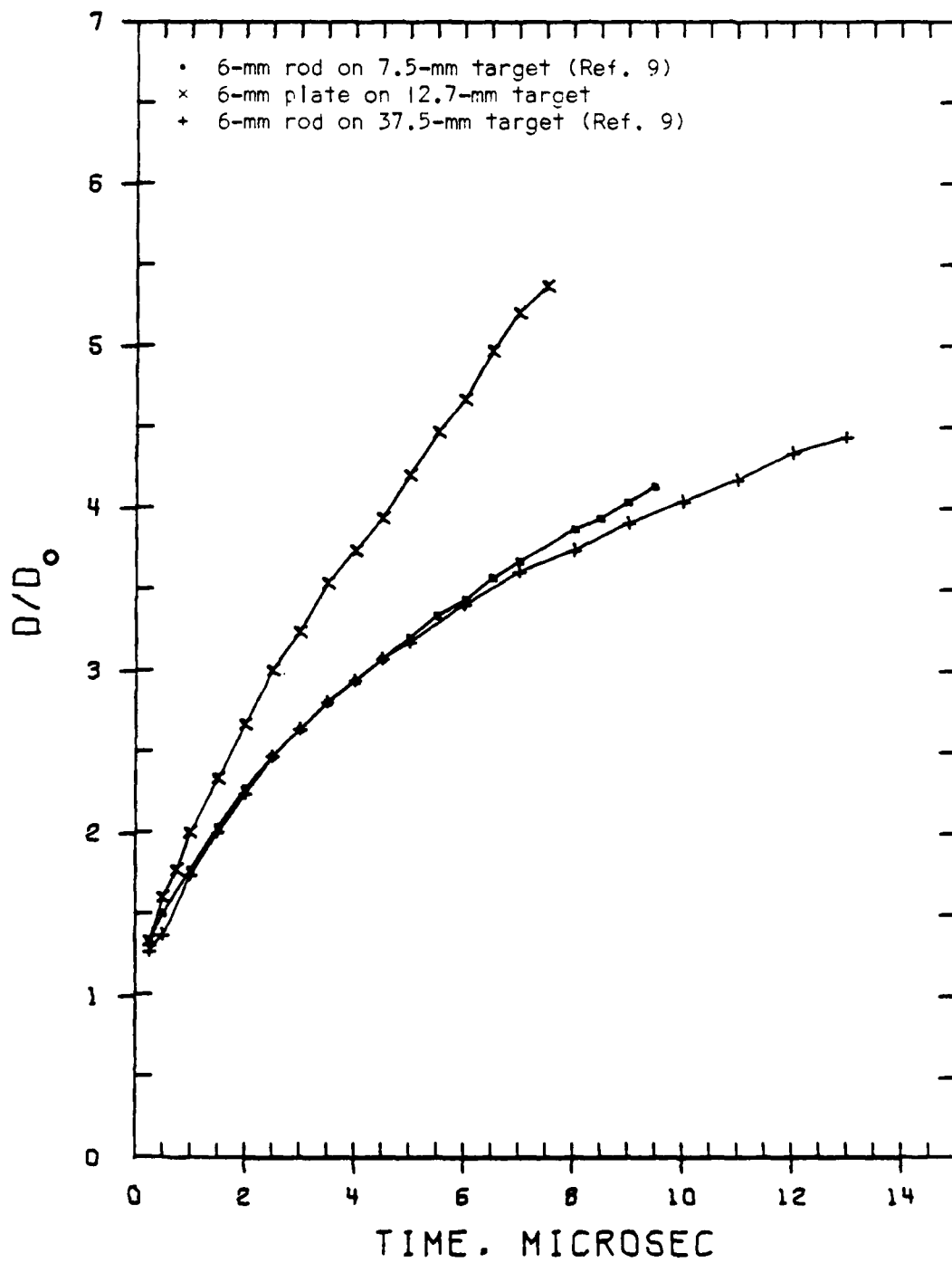


Figure 27. Comparison of Hole Growth for 0° Oblique Impact

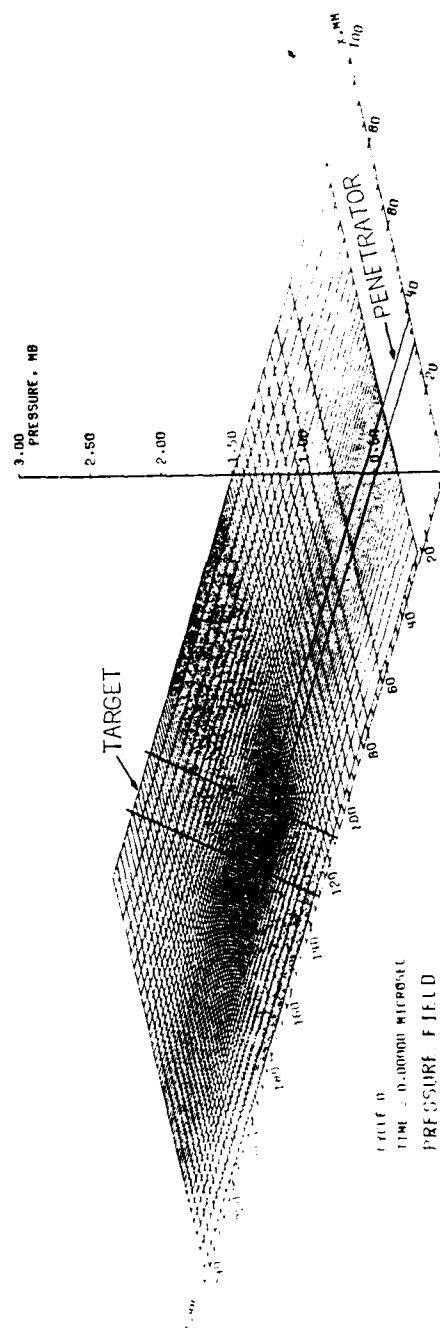


Figure 28. Pressure Field for 45° Oblique Impact

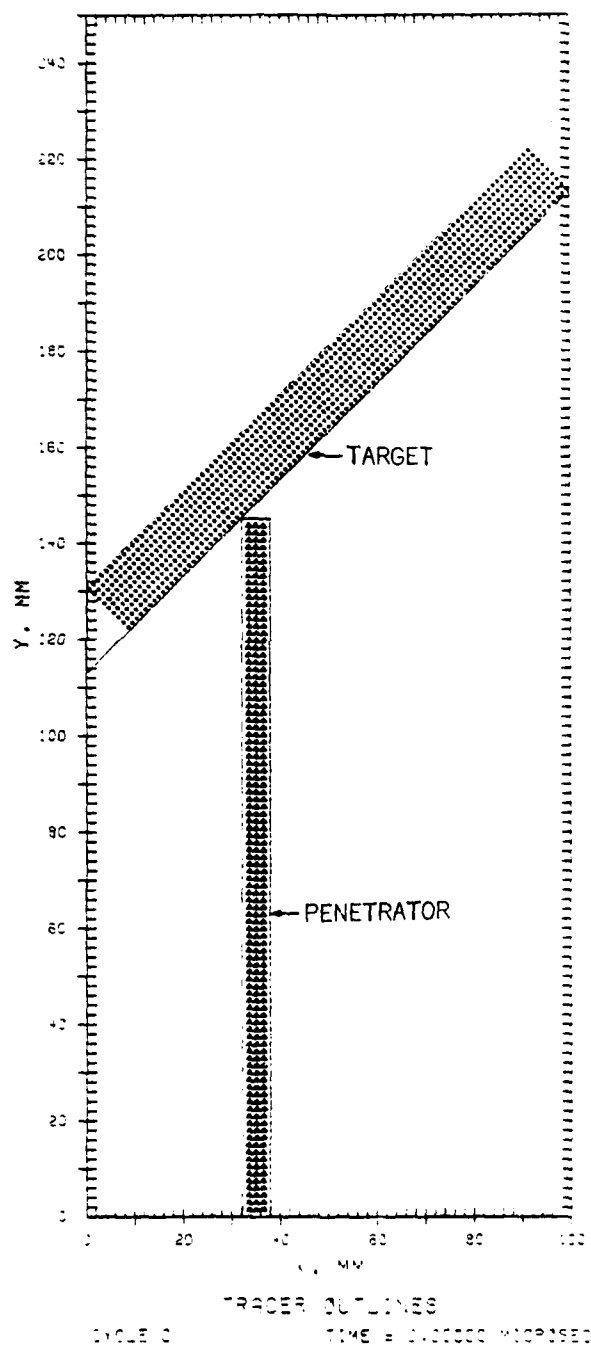


Figure 29. Penetrator-Target Deformation for 45° Oblique Impact

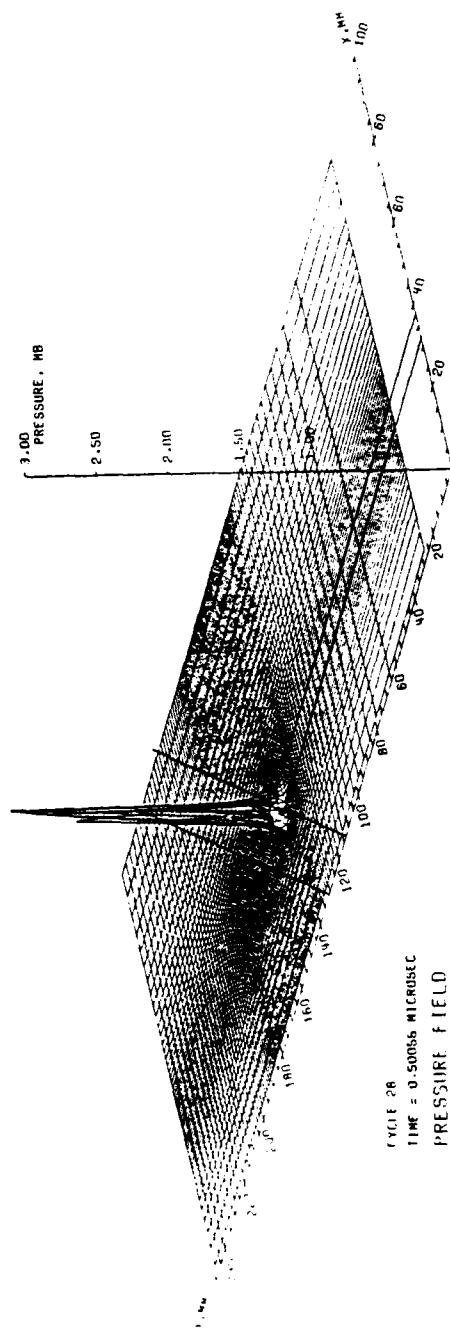


Figure 30. Pressure Field for 45° Oblique Impact

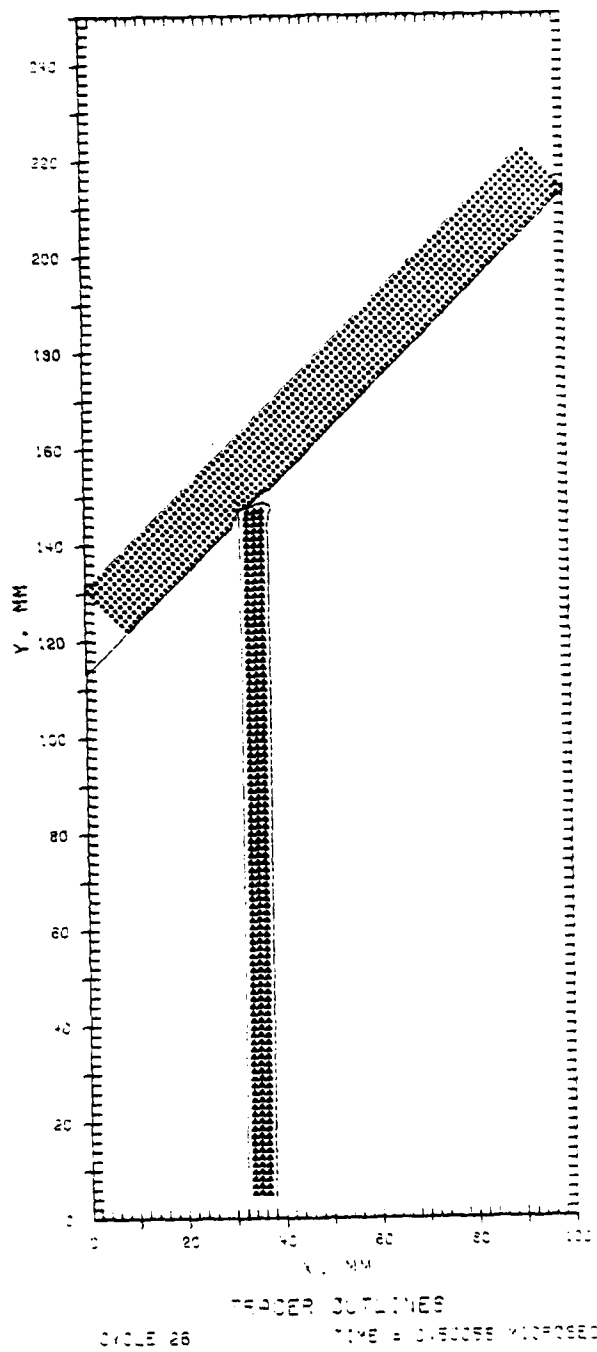


Figure 31. Penetrator-Target Deformation for 45° Oblique Impact

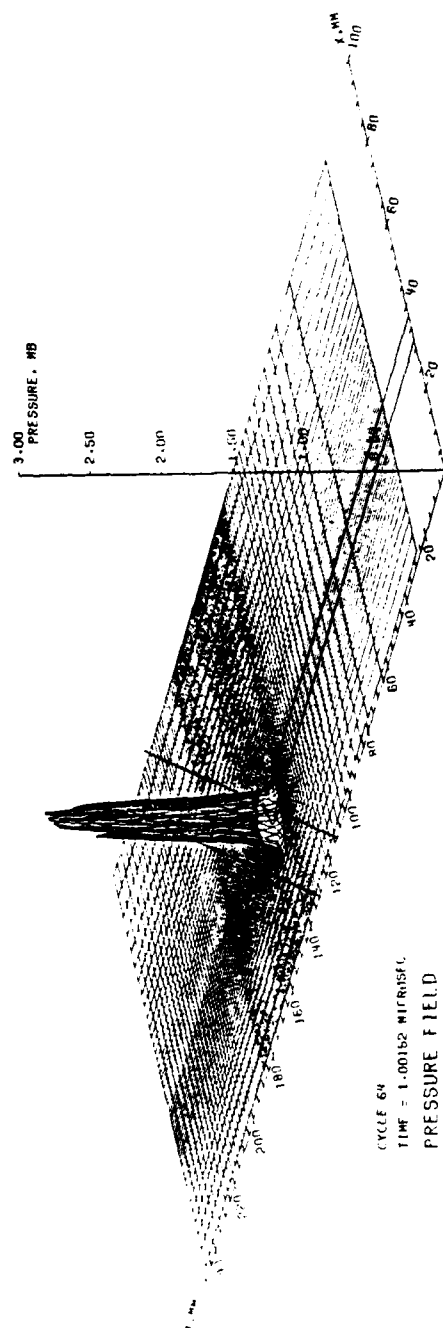


Figure 32. Pressure Field for 45° Oblique Impact

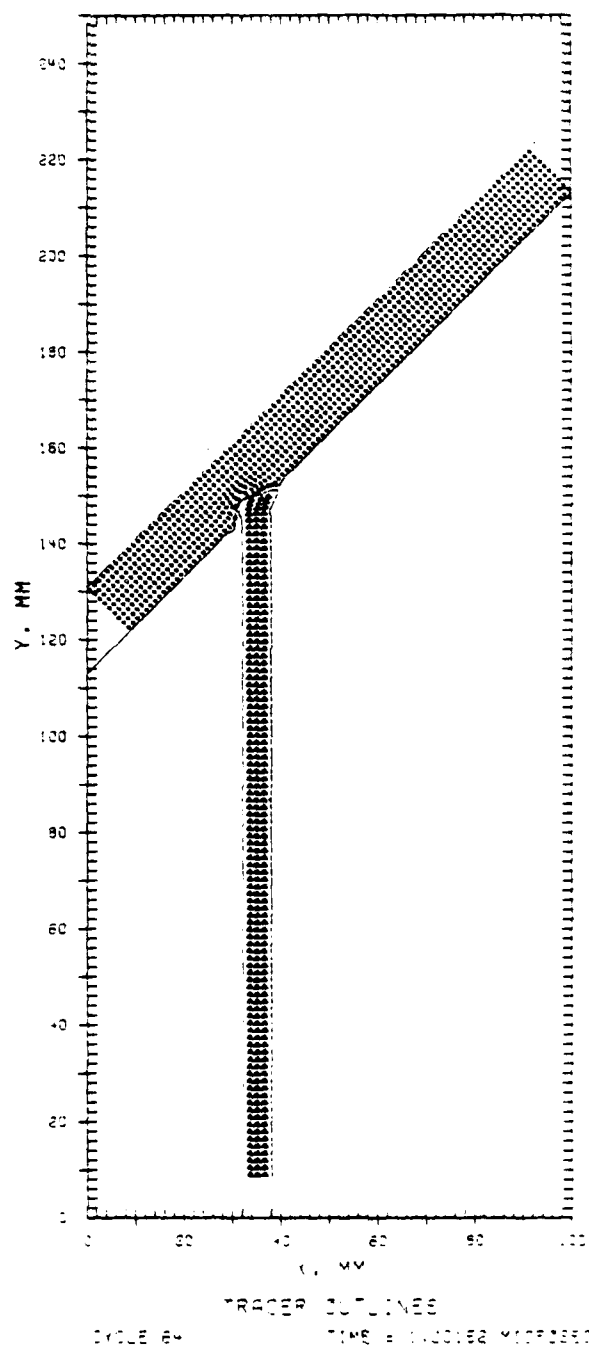


Figure 33. Penetrator-Target Deformation for 45° Oblique Impact

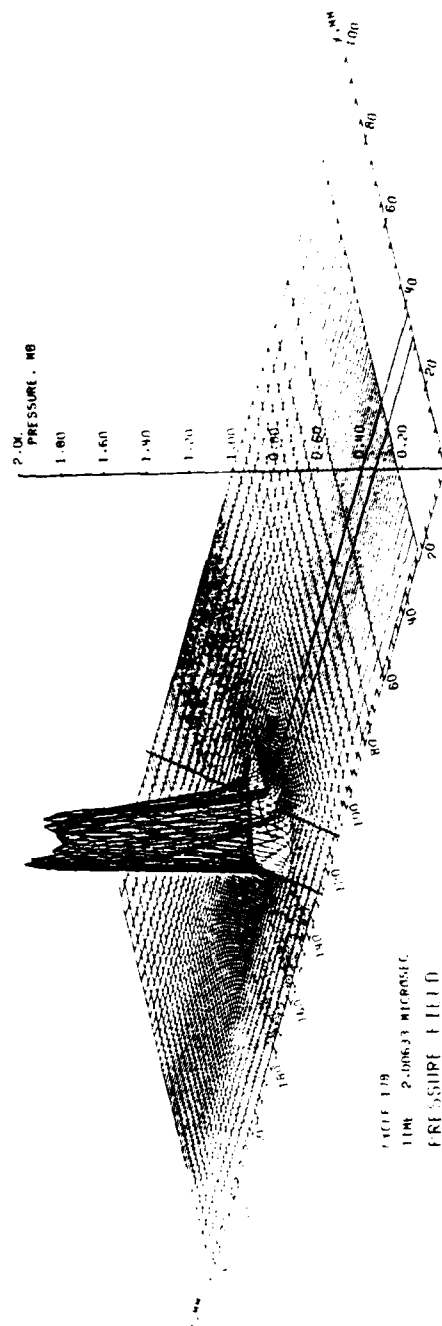


Figure 34. Pressure Field for 45° Oblique Impact

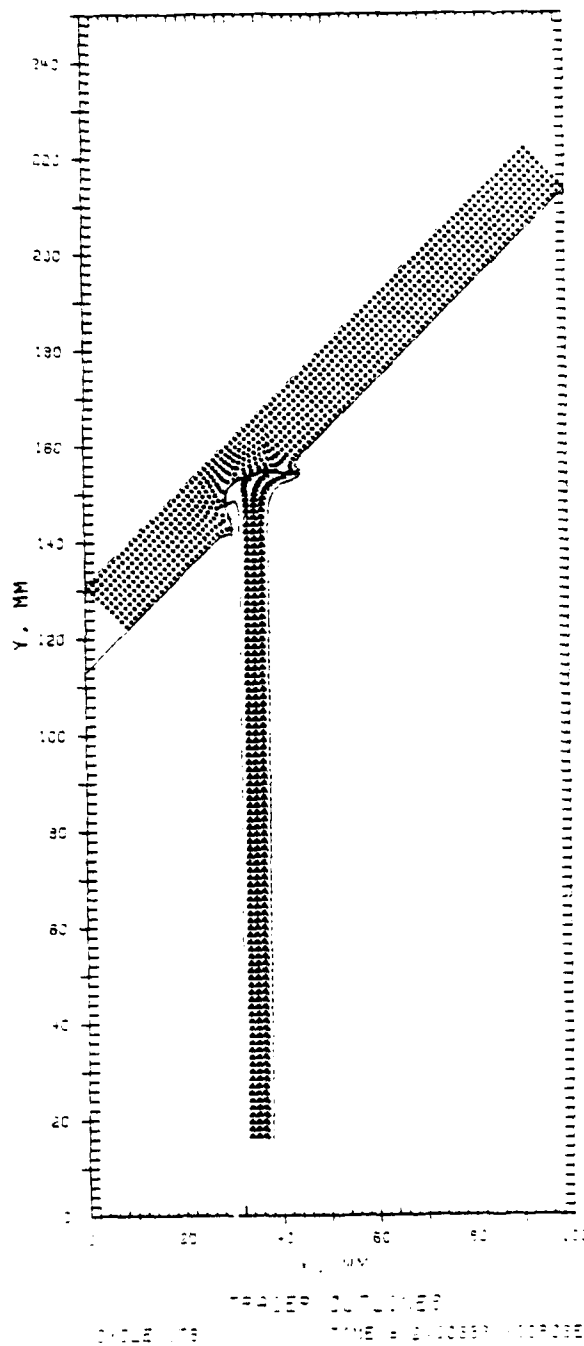


Figure 35. Penetrator-Target Deformation for 45° Oblique Impact

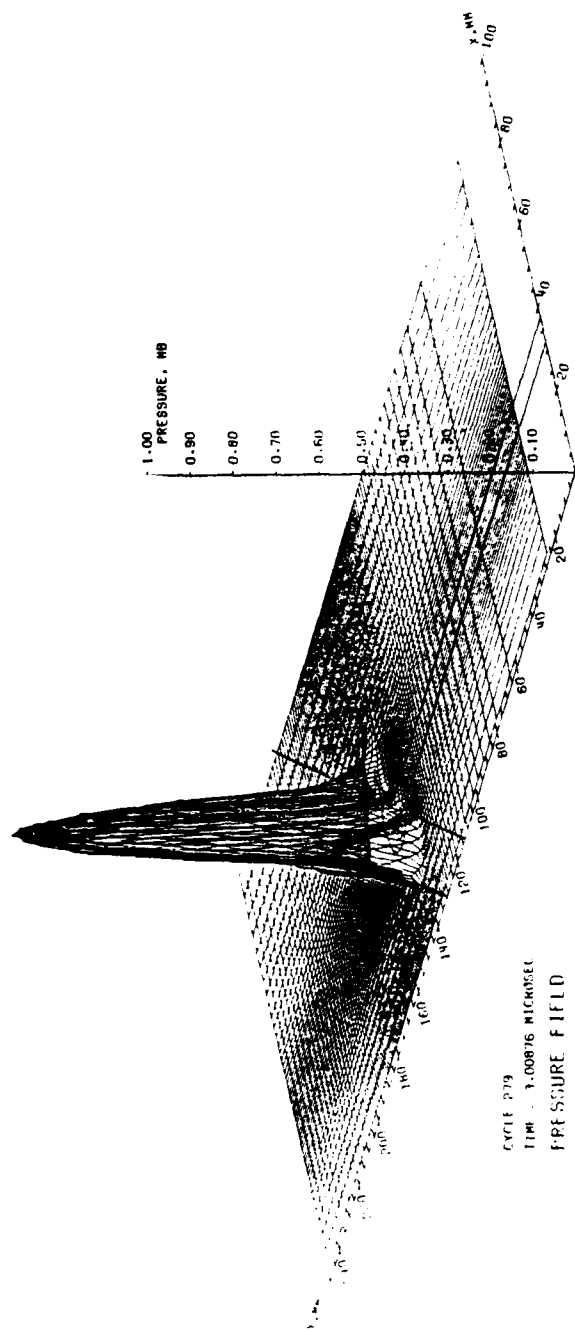


Figure 36. Pressure Field for 45° Oblique Impact

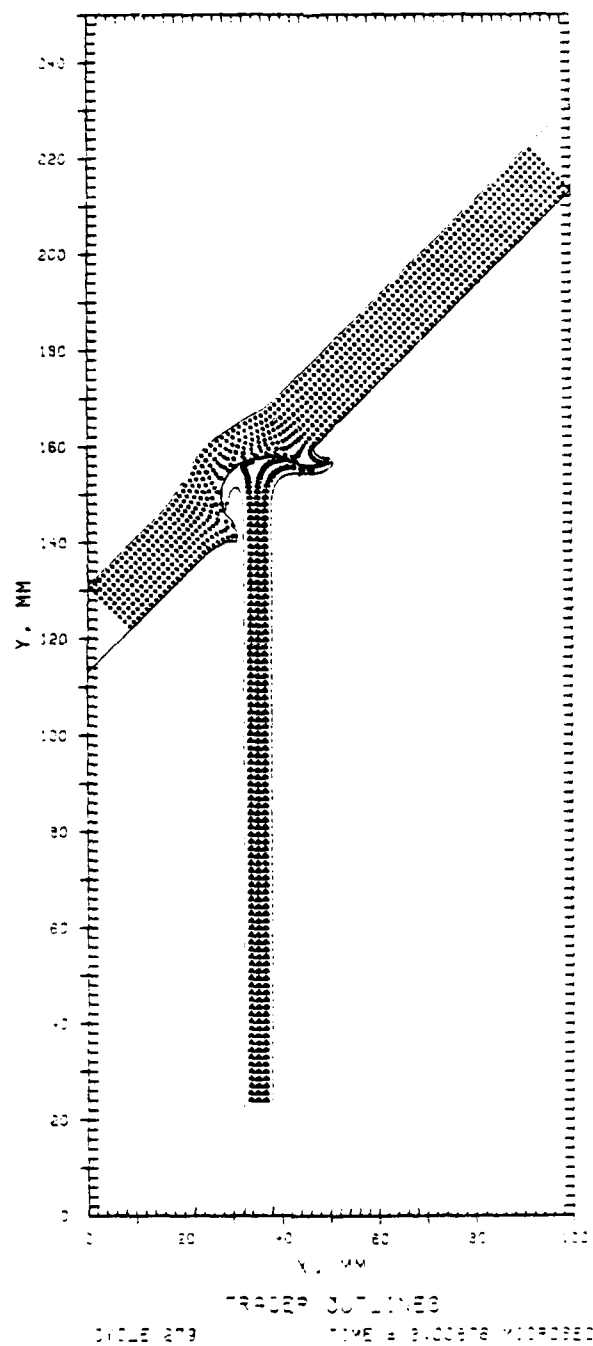


Figure 37. Penetrator-Target Deformation for 45° Oblique Impact

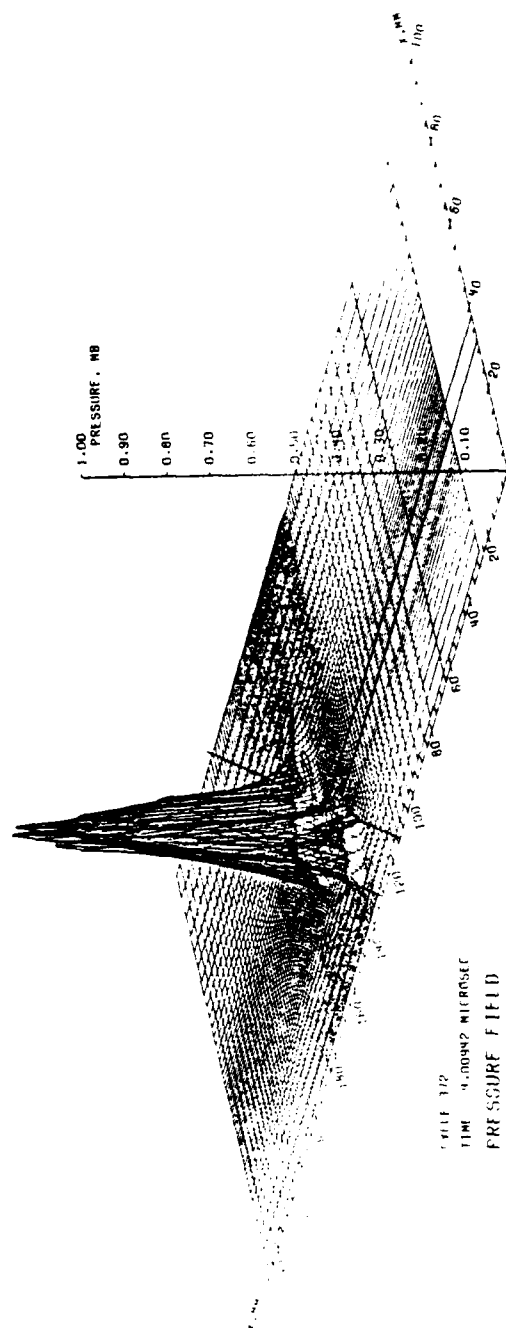
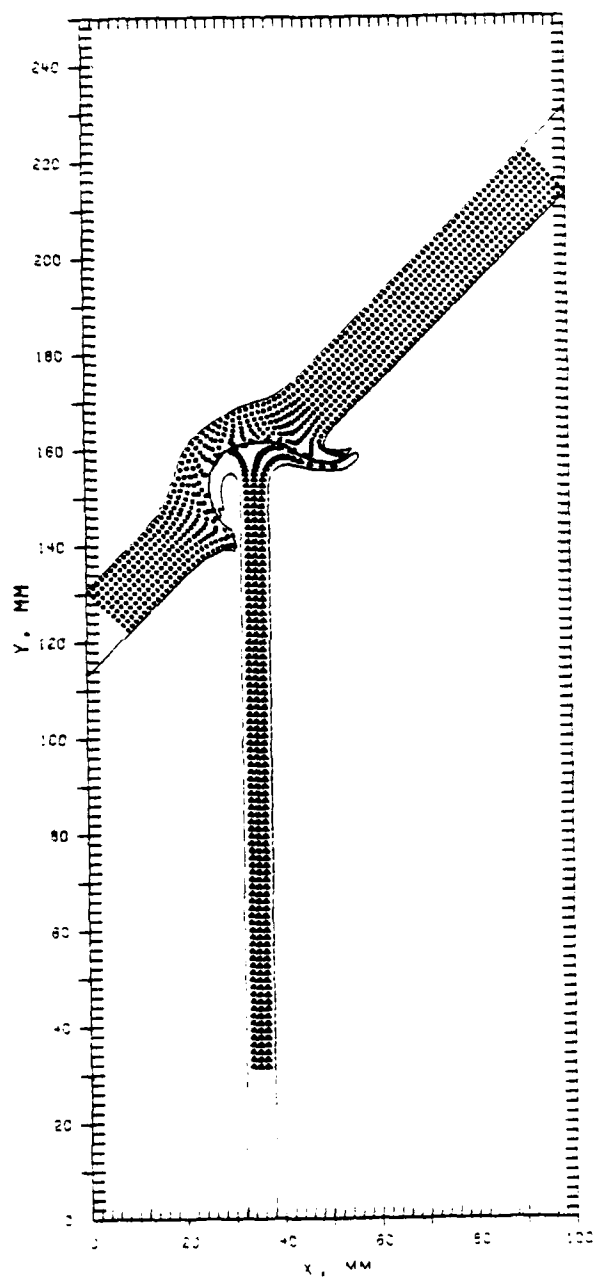


Figure 38. Pressure Field for 45° Oblique Impact



TRACER OUTLINES
CYCLE 372 TIME = 4.1029-2 MICROSECS

Figure 39. Penetrator-Target Deformation for 45° Oblique Impact

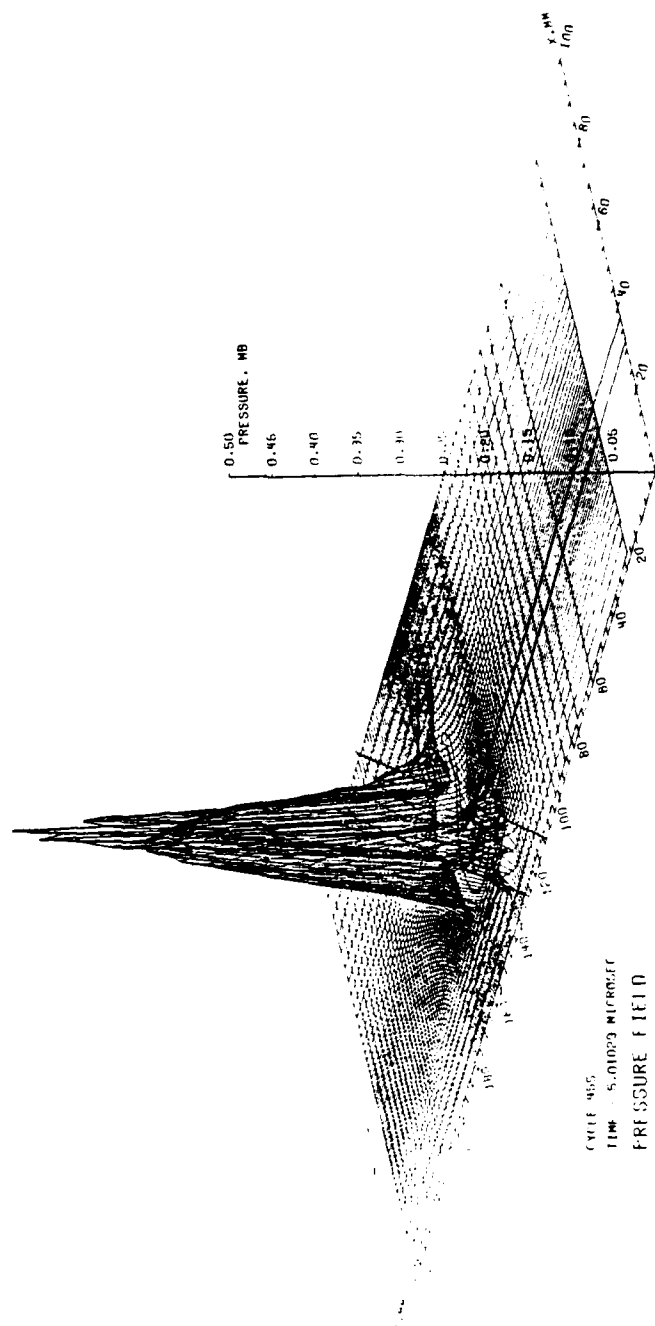


Figure 40. Pressure Field for 45° Oblique Impact

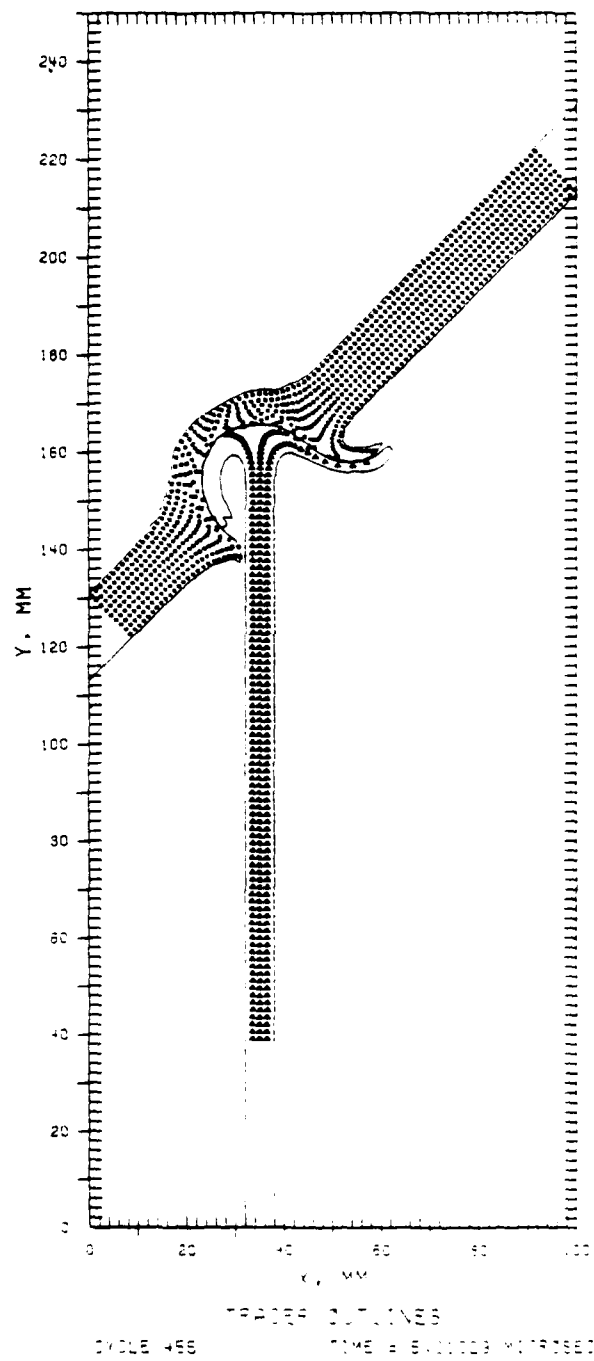


Figure 41. Penetrator-Target Deformation for 45° Oblique Impact

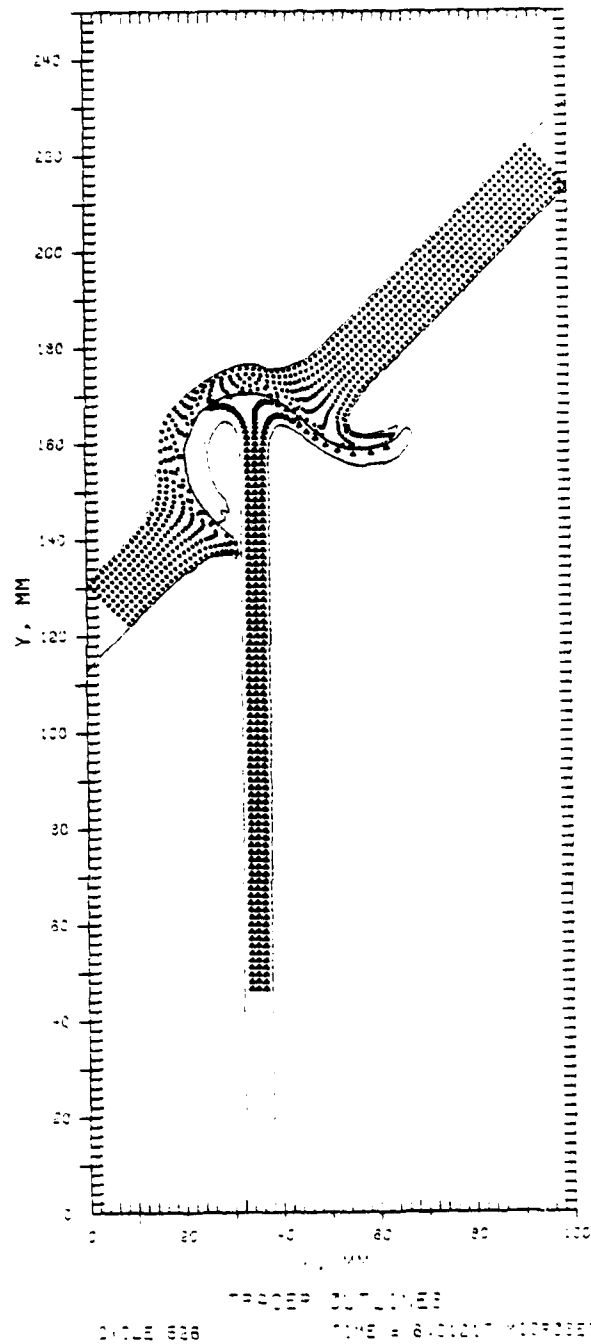


Figure 43. Penetrator-Target Deformation for 45° Oblique Impact

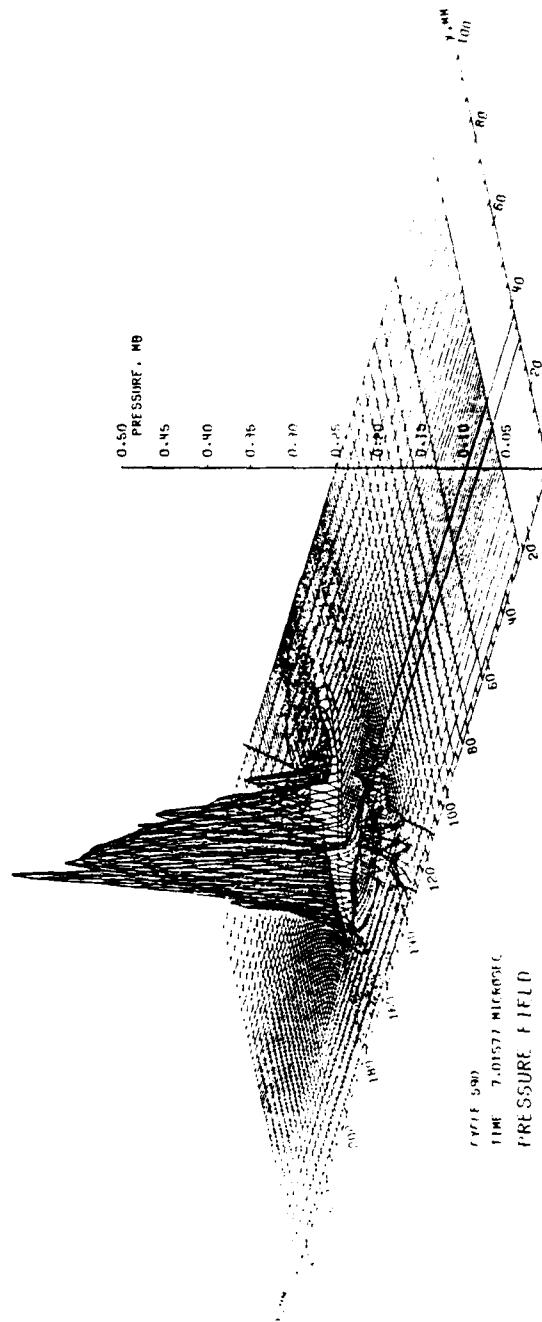


Figure 44. Pressure Field for 45° Oblique Impact

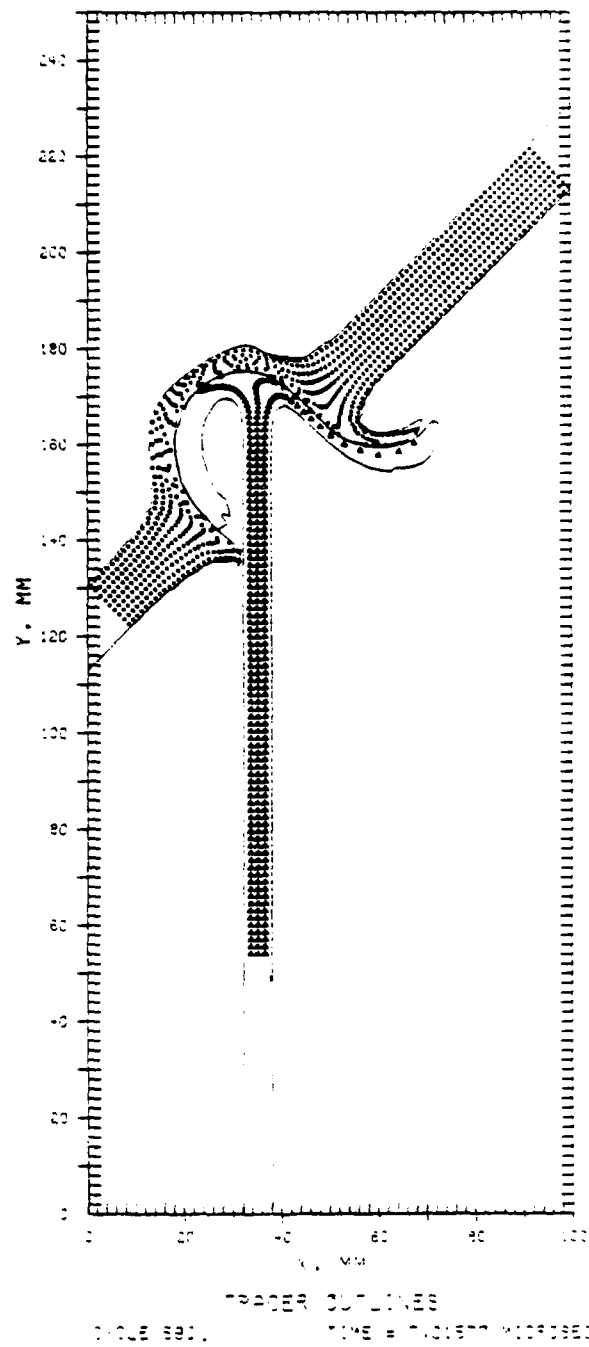


Figure 45. Penetrator-Target Deformation for 45° Oblique Impact

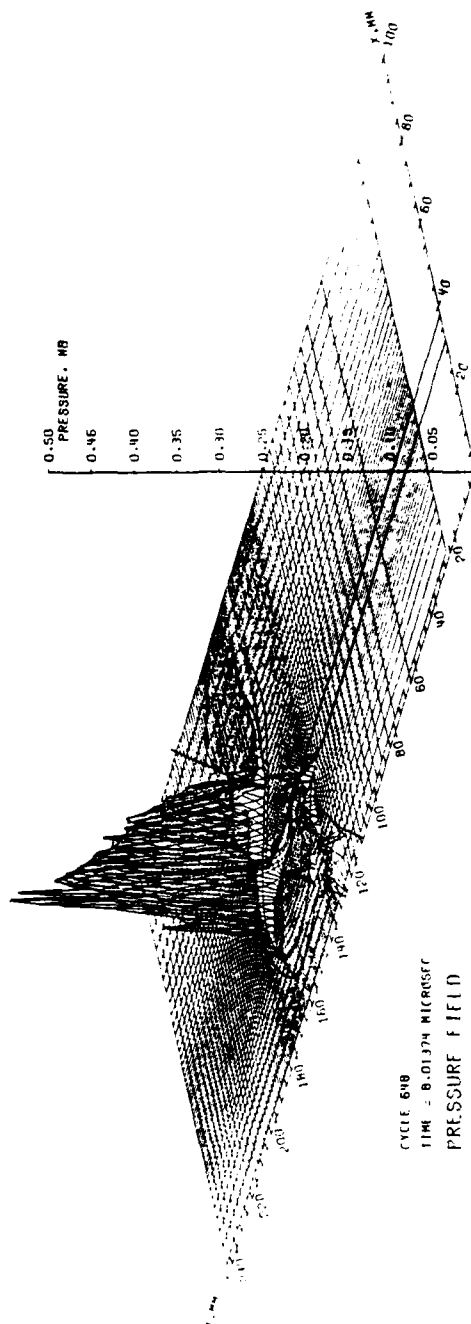


Figure 46. Pressure Field for 45° Oblique Impact

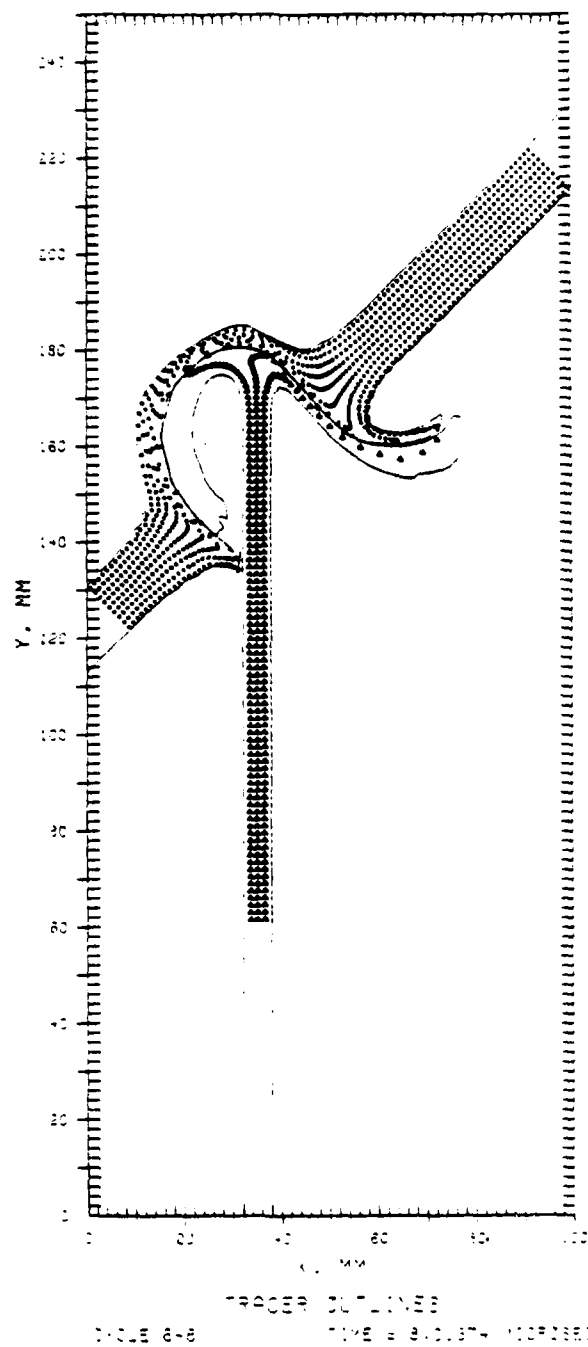


Figure 47. Penetrator-Target Deformation for 45° Oblique Impact

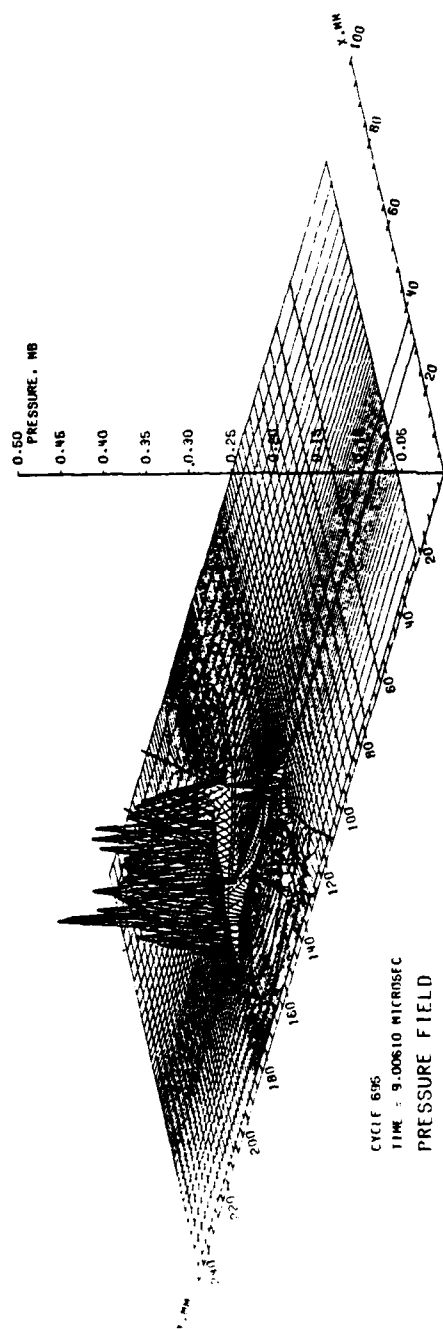


Figure 48. Pressure Field for 45° Oblique Impact

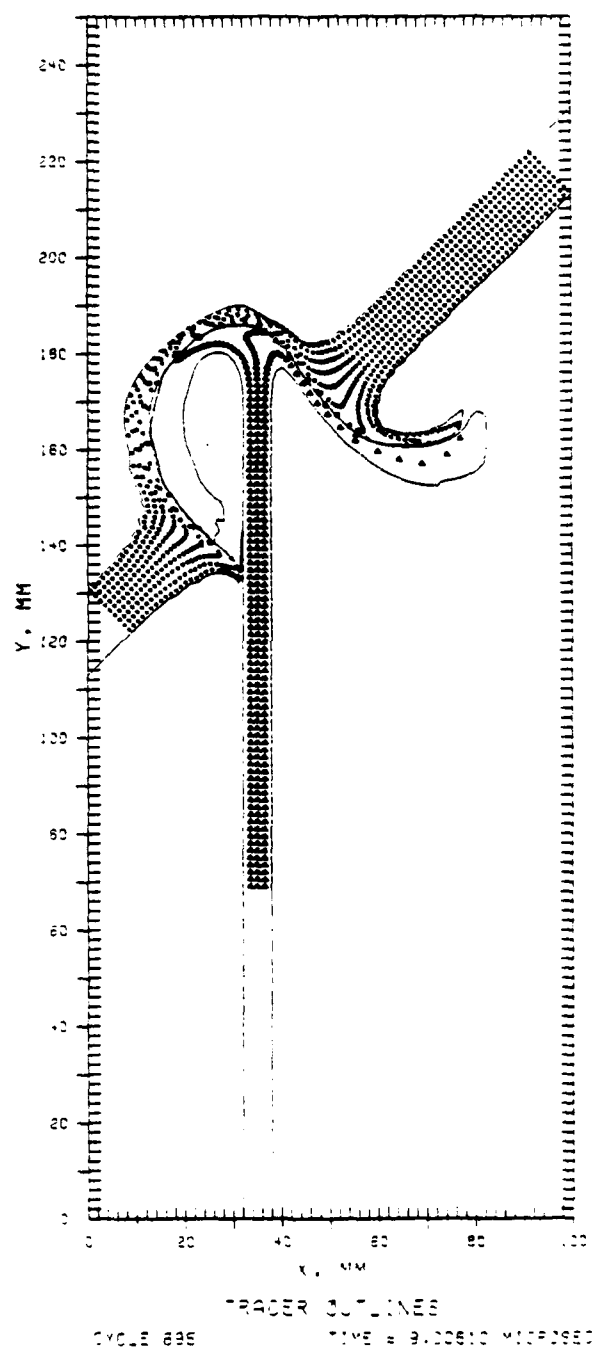


Figure 49. Penetrator-Target Deformation for 45° Oblique Impact

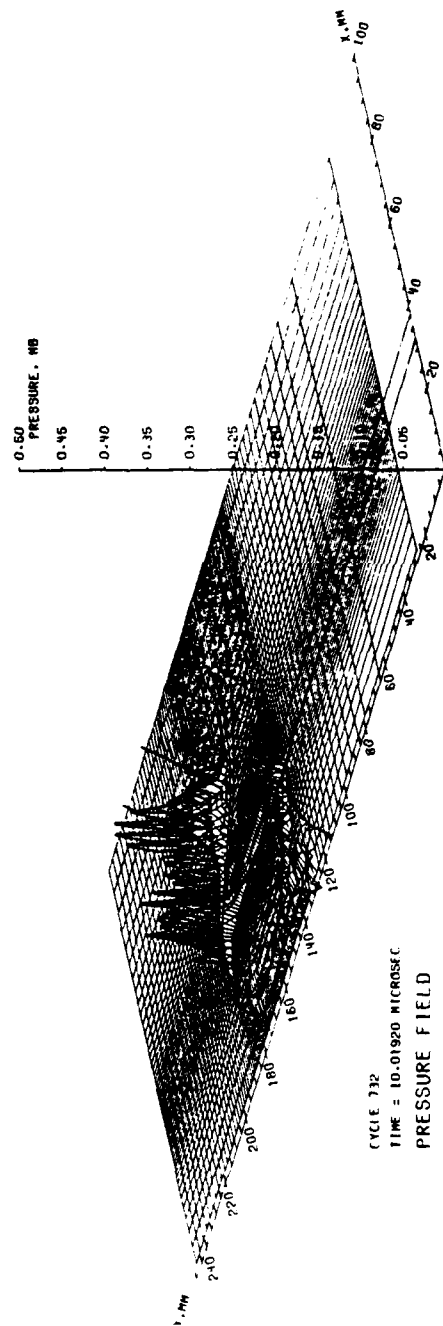


Figure 50. Pressure Field for 45° Oblique Impact

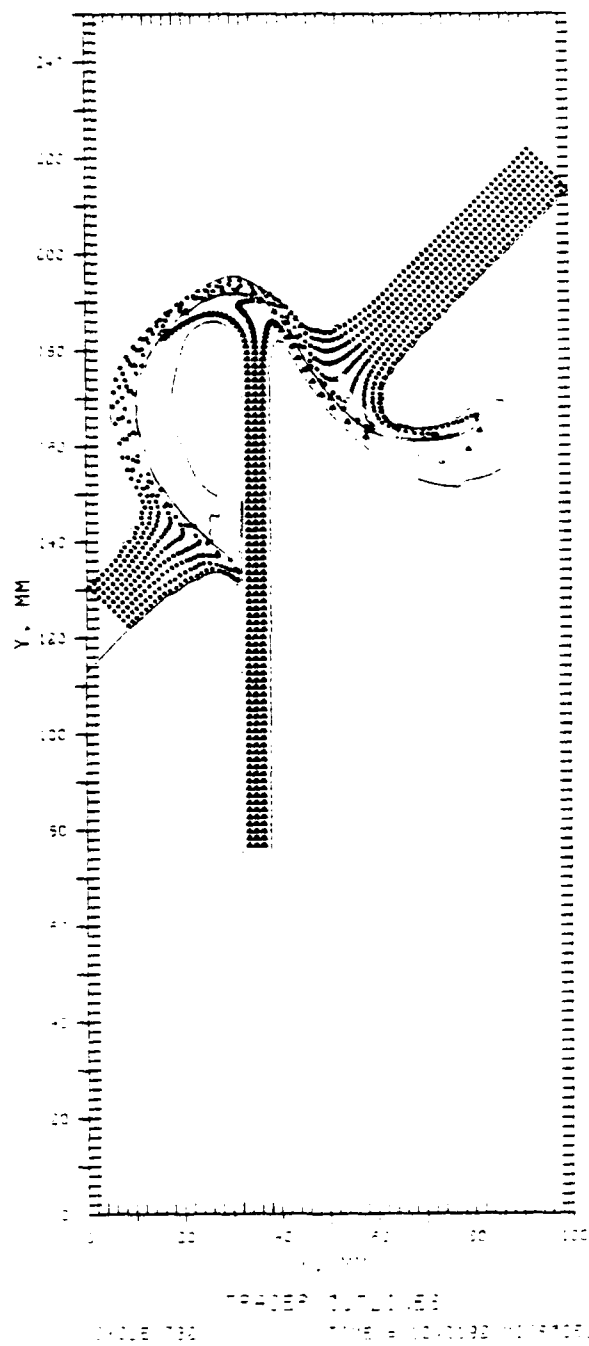


Figure 51. Penetrator-Target Deformation for 45° Oblique Impact

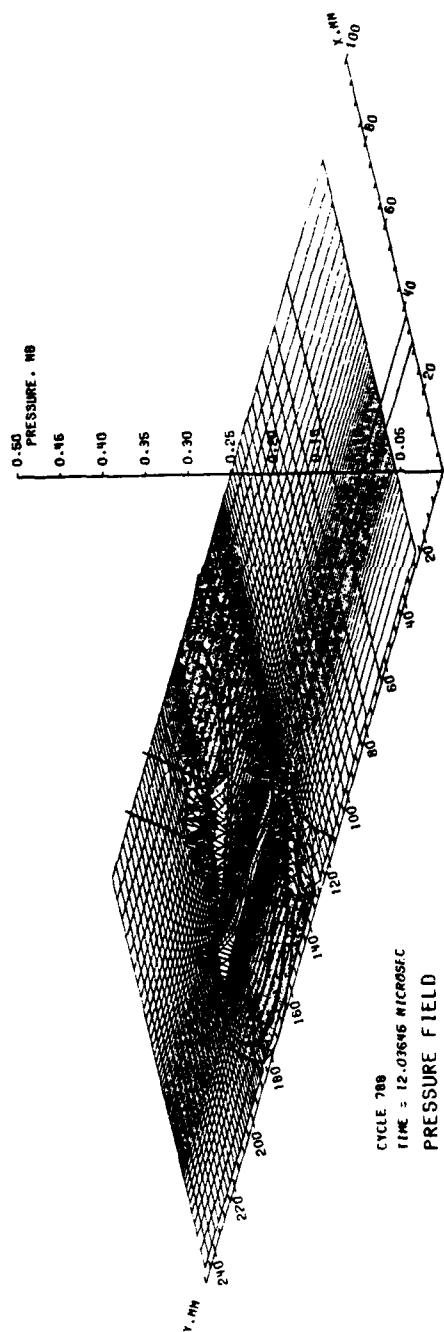


Figure 52. Pressure Field for 45° Oblique Impact

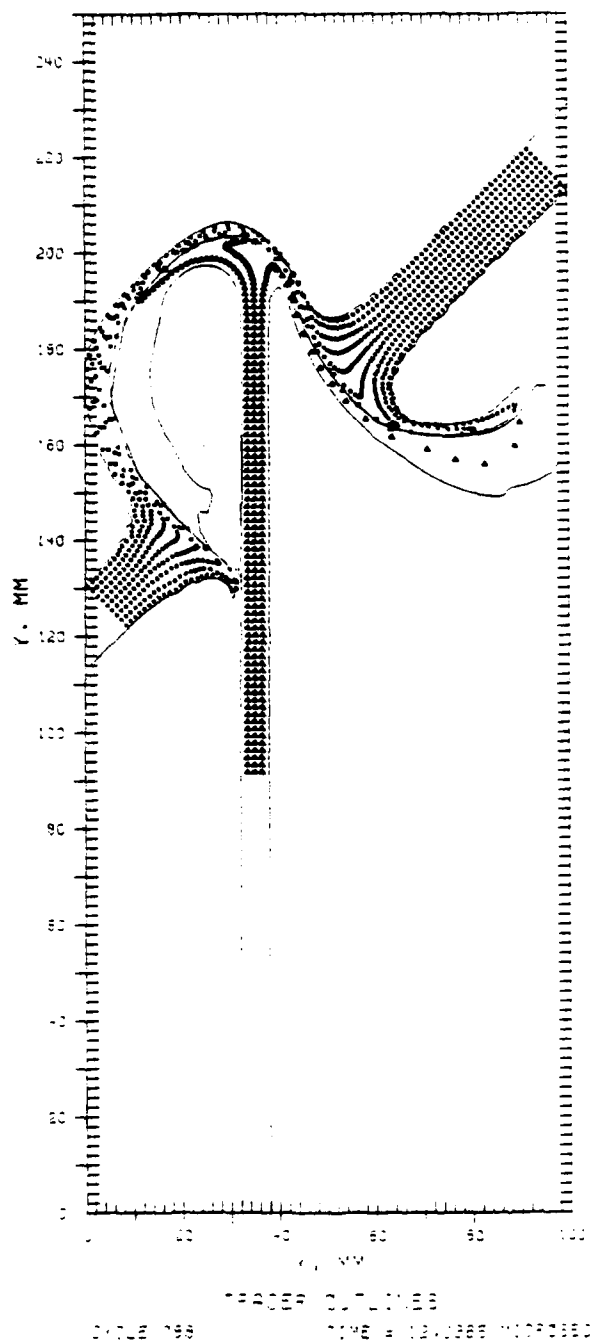


Figure 53. Penetrator-Target Deformation for 45° Oblique Impact

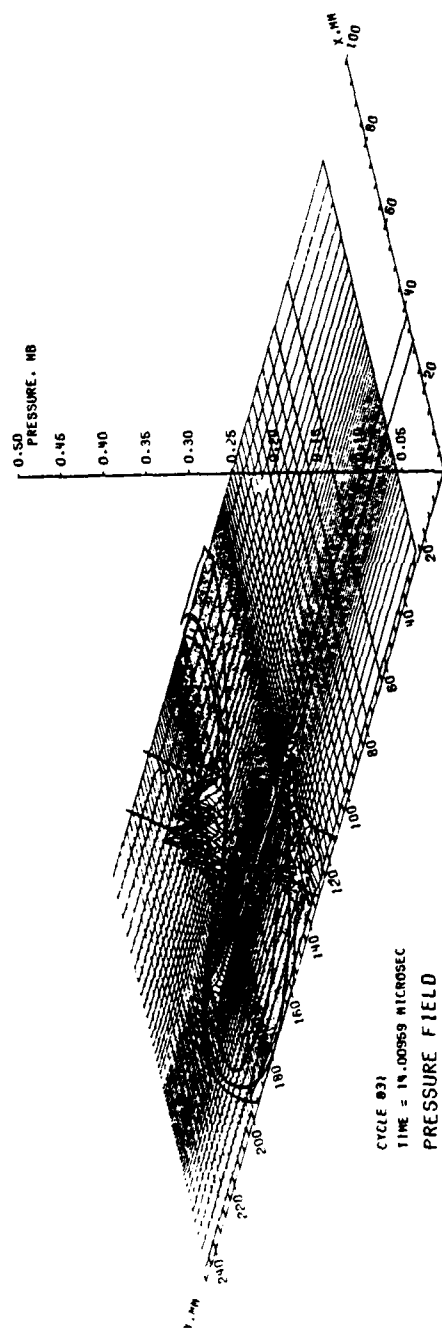


Figure 54. Pressure Field for 45° Oblique Impact

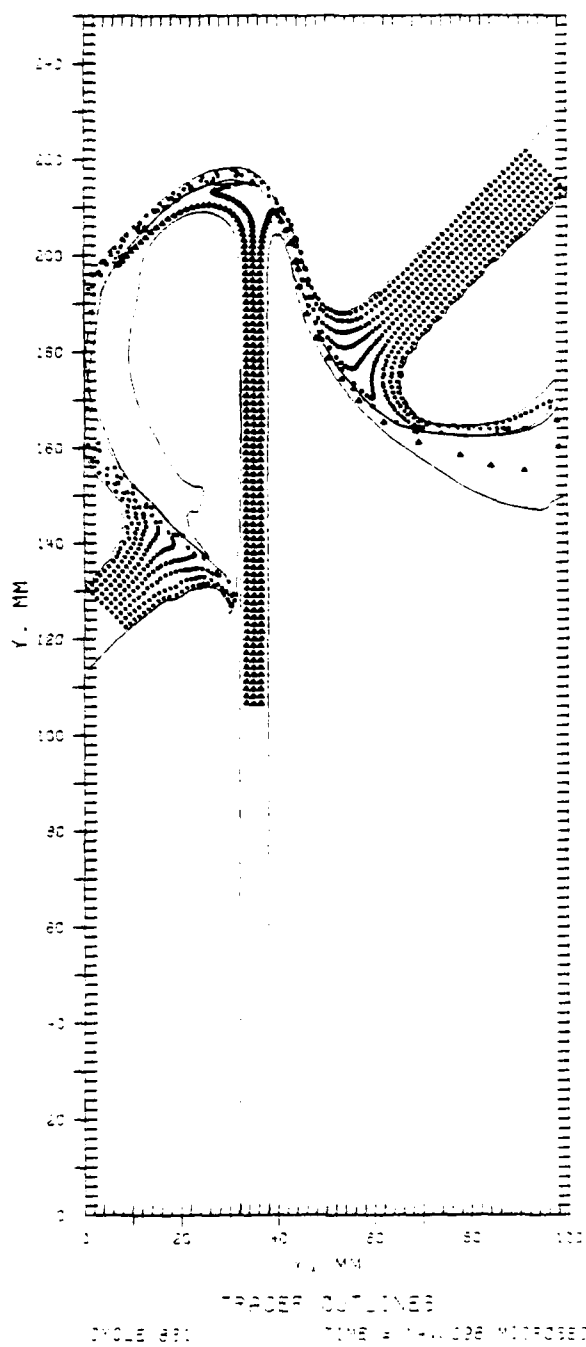


Figure 55. Penetrator-Target Deformation for 45° Oblique Impact

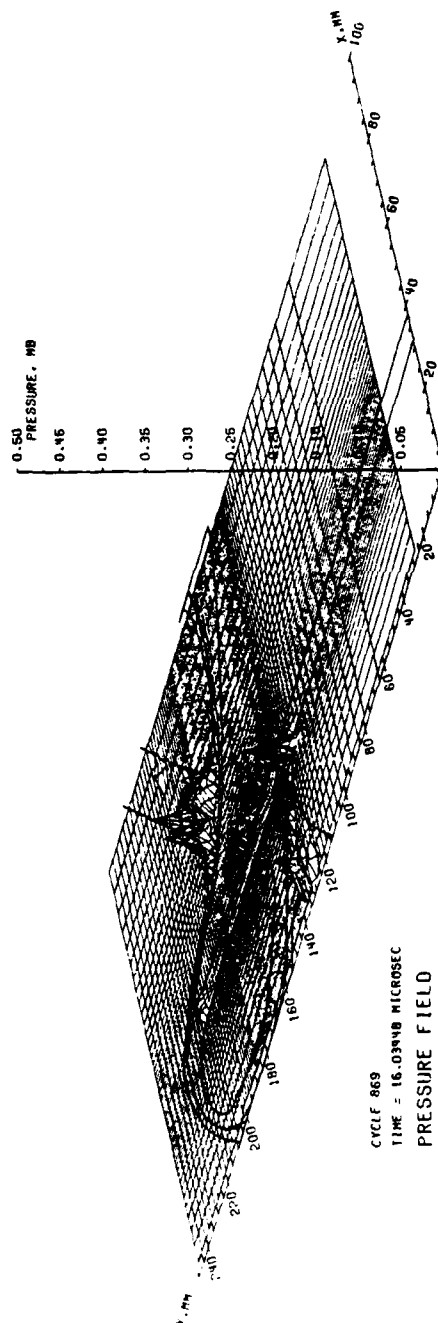


Figure 56. Pressure Field for 45° Oblique Impact

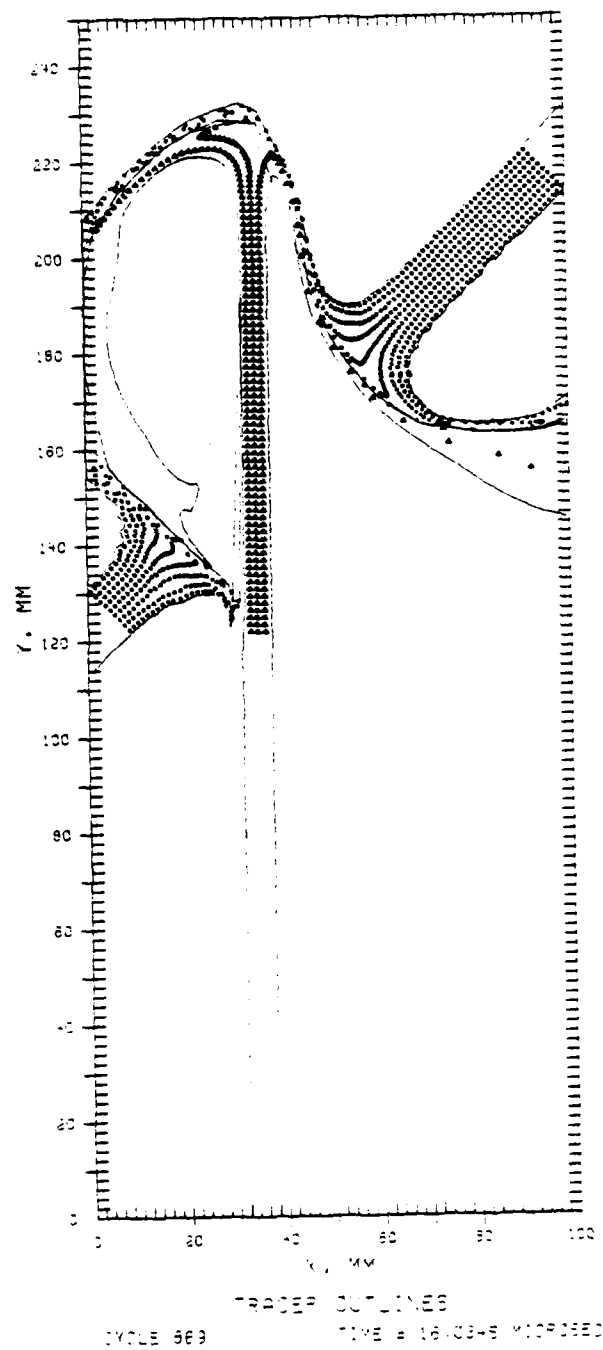


Figure 57. Penetrator-Target Deformation for 45° Oblique Impact

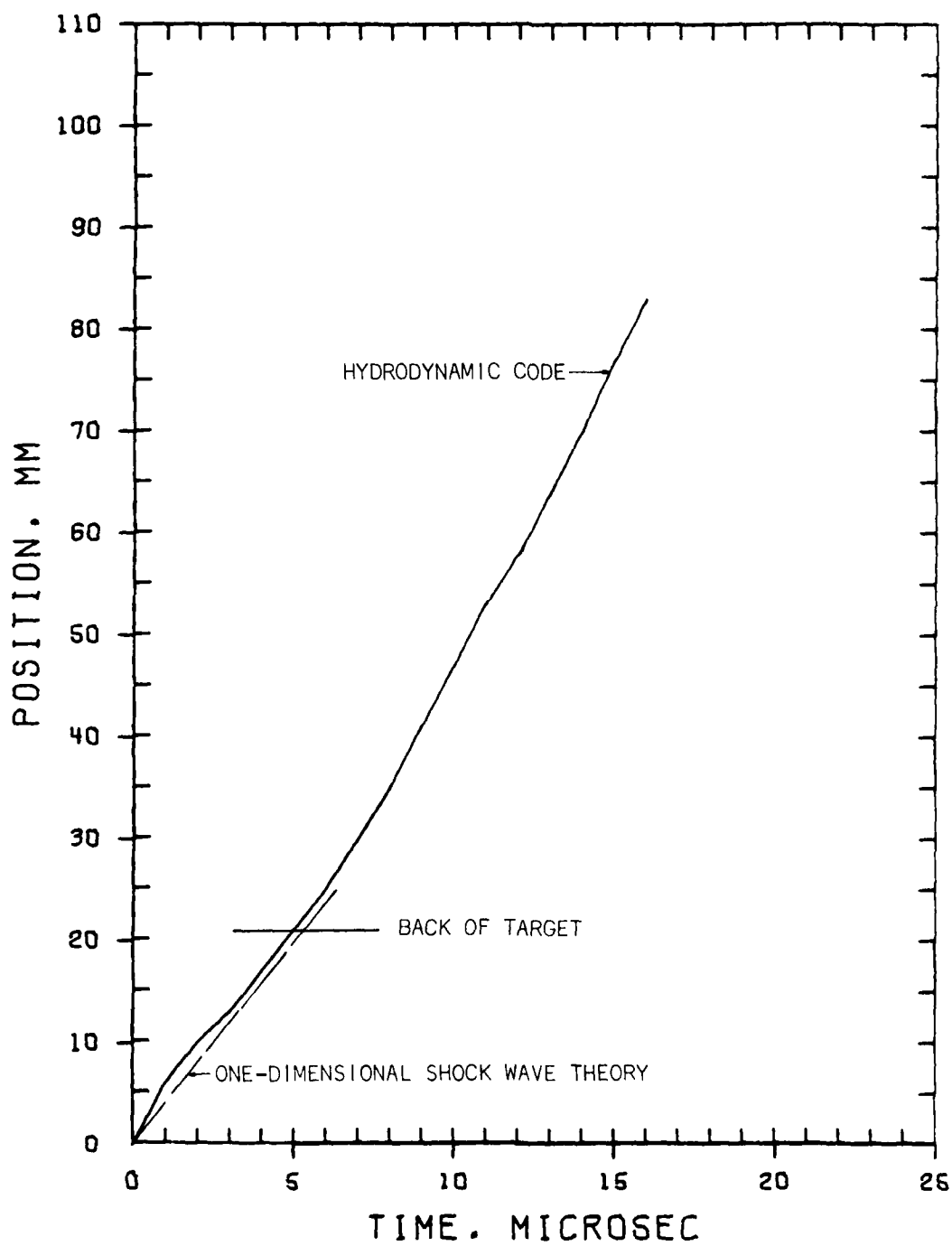


Figure 58. Penetration History for 45° Oblique Impact

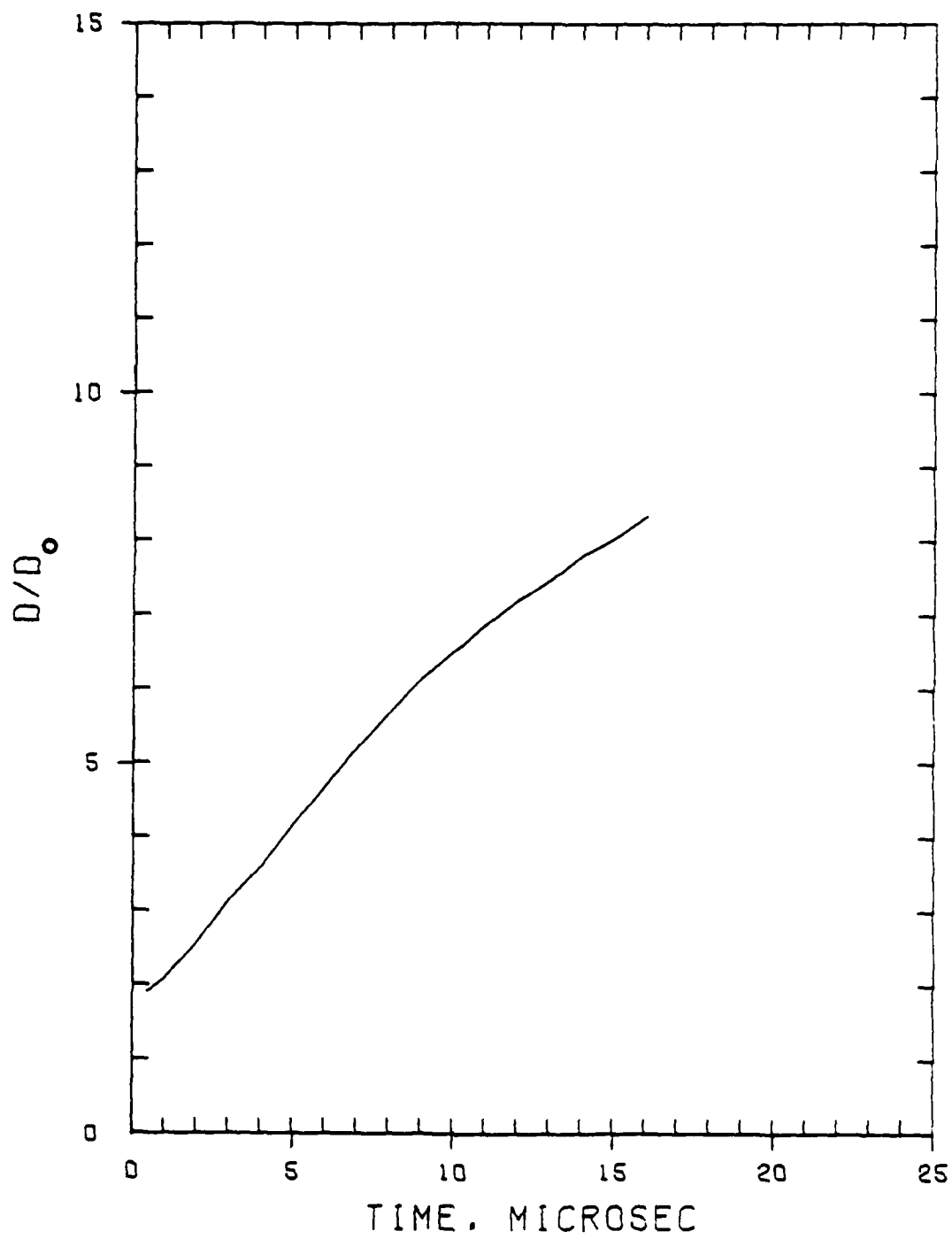


Figure 59. Growth of the Front Face Cut for 45° Oblique Impact

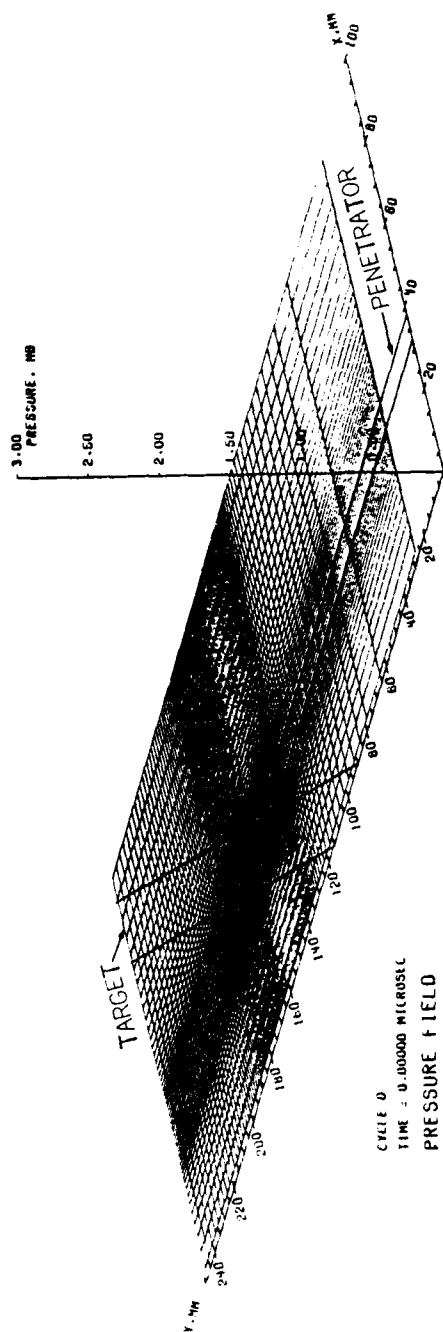


Figure 60. Pressure Field for 60° Oblique Impact

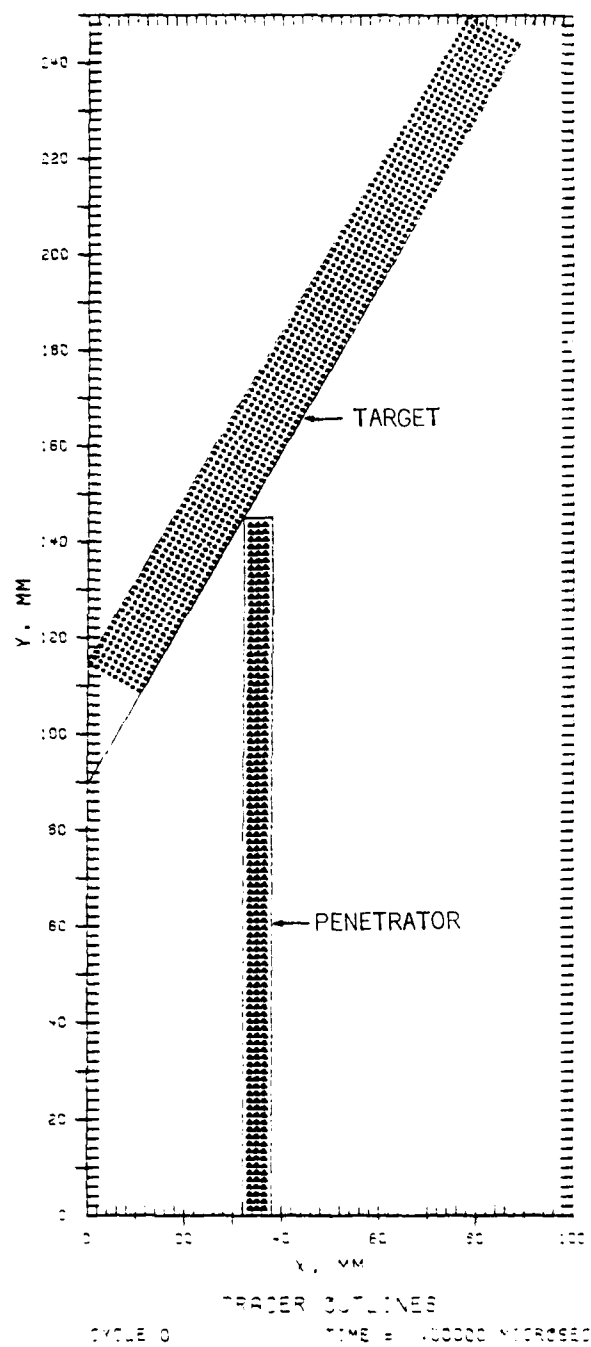


Figure 61. Penetrator-Target Deformation for 60° Oblique Impact

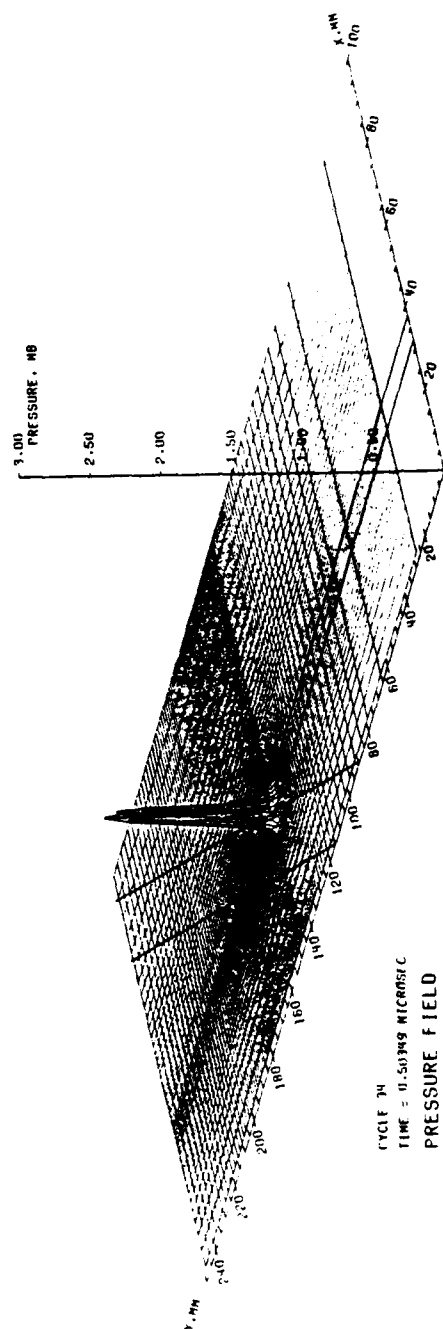


Figure 62. Pressure Field for 60° Oblique Impact

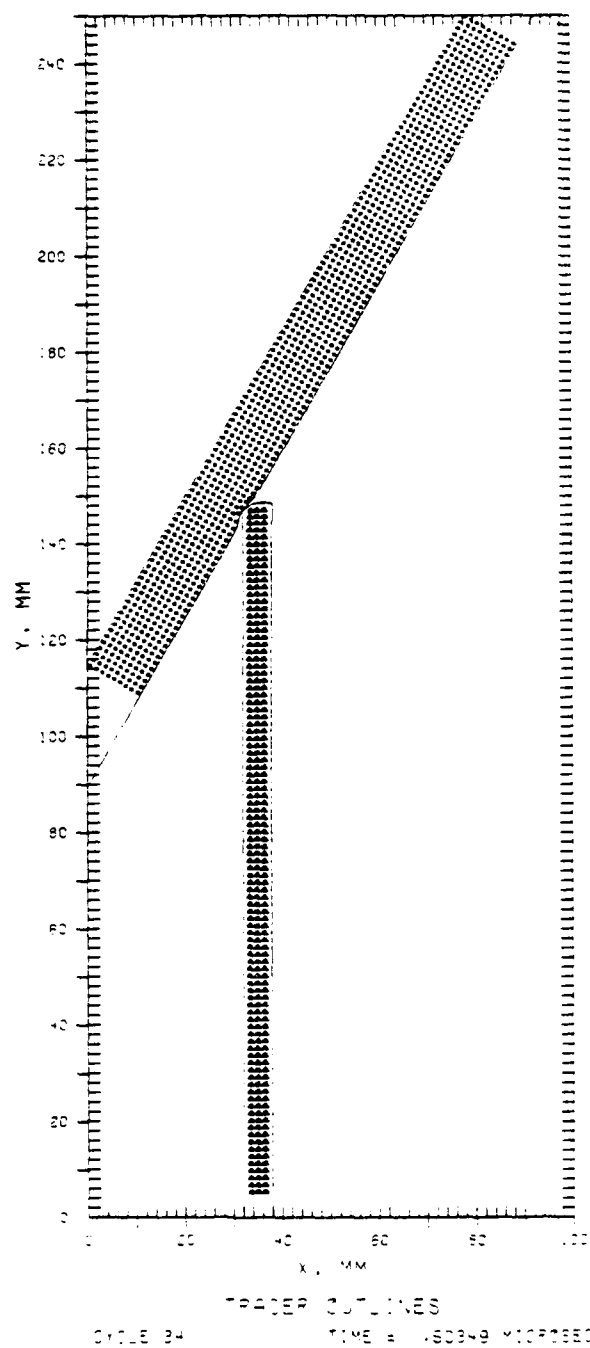


Figure 63. Penetrator-Target Deformation for 60° Oblique Impact

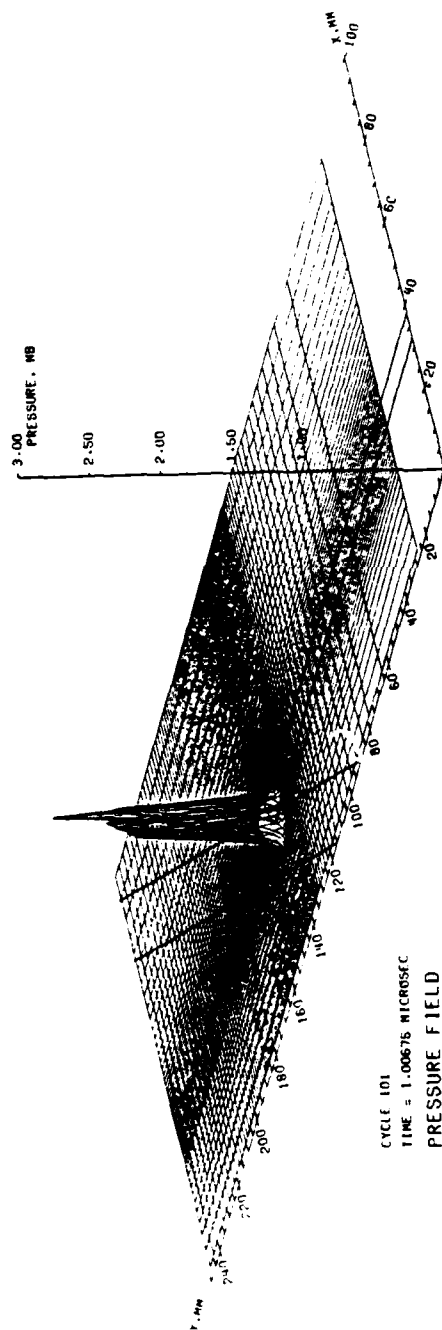


Figure 64. Pressure Field for 60° Oblique Impact

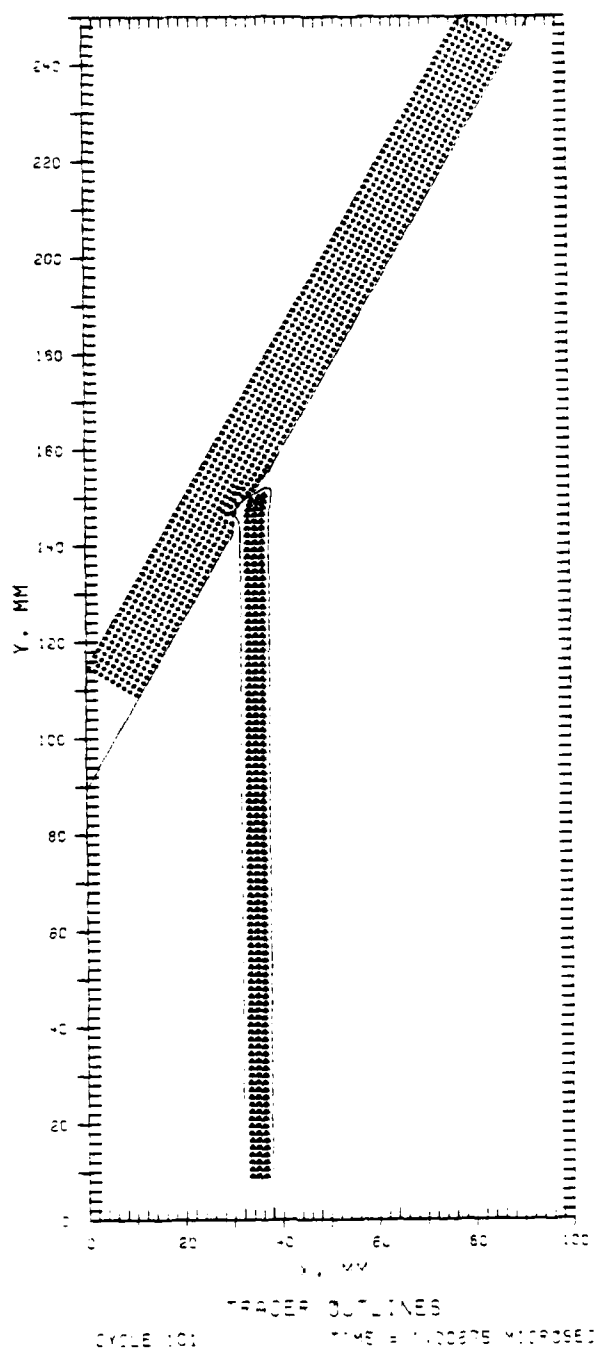


Figure 65. Penetrator-Target Deformation for 60° Oblique Impact

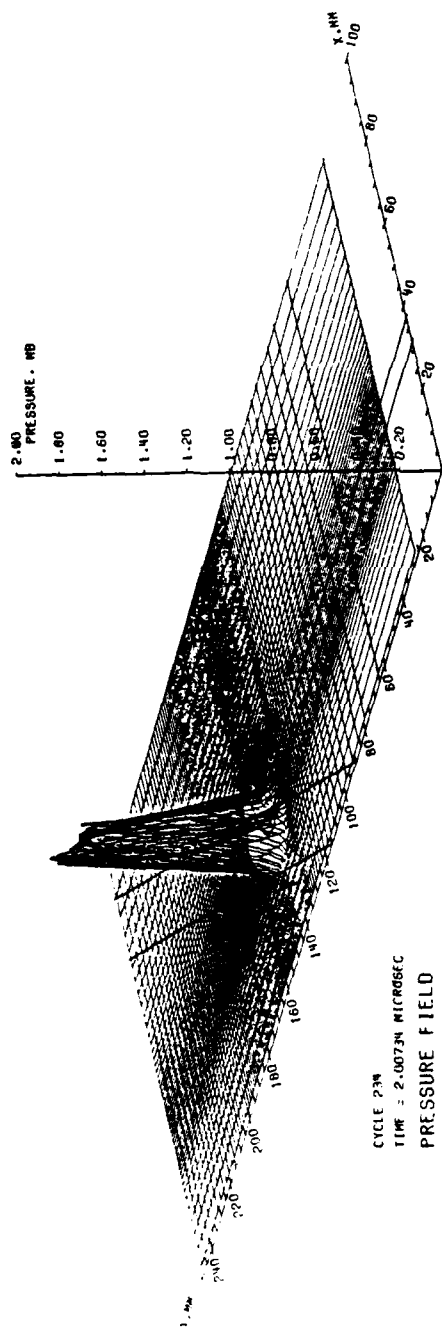


Figure 66. Pressure Field for 60° Oblique Impact

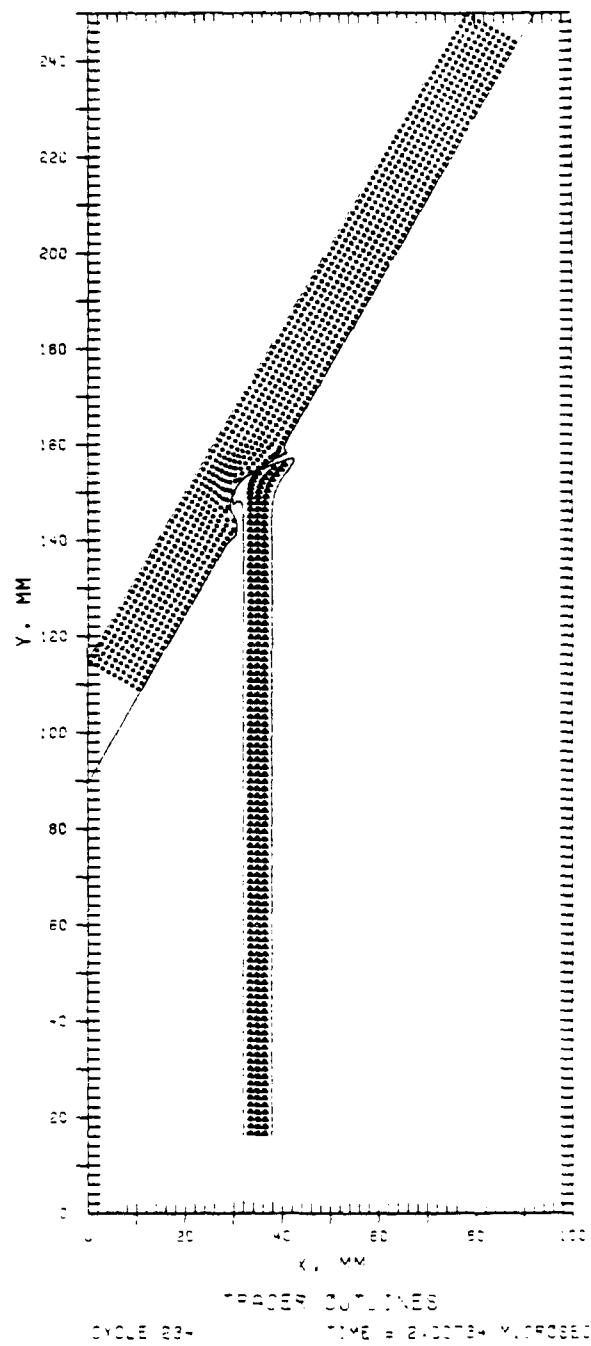


Figure 67. Penetrator-Target Deformation for 60° Oblique Impact

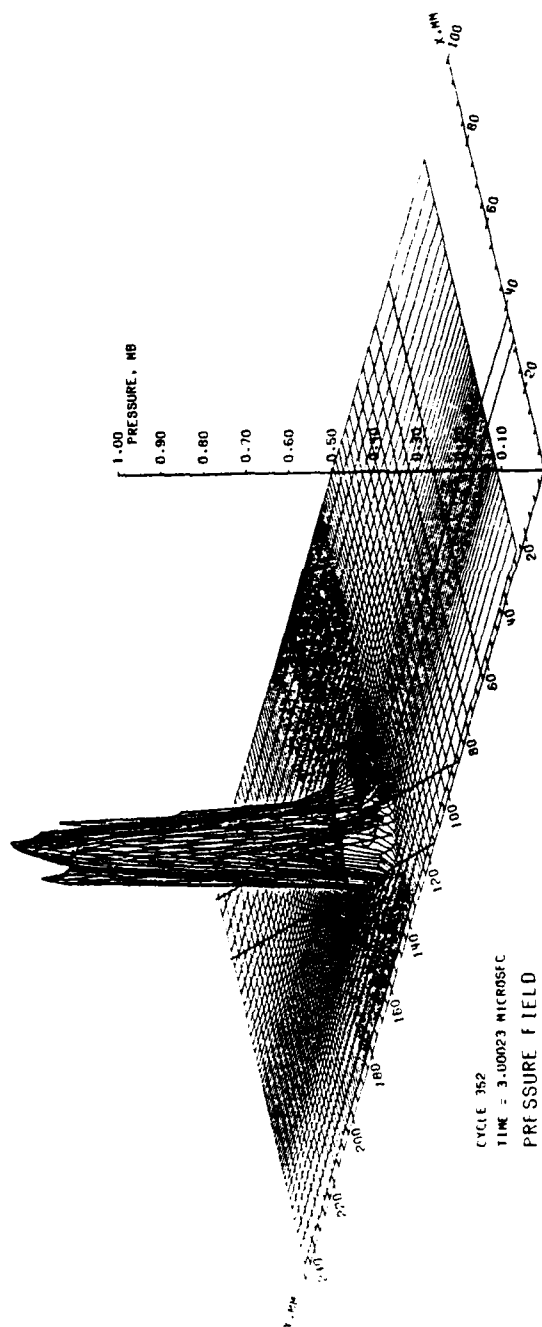


Figure 68. Pressure Field for 60° Oblique Impact

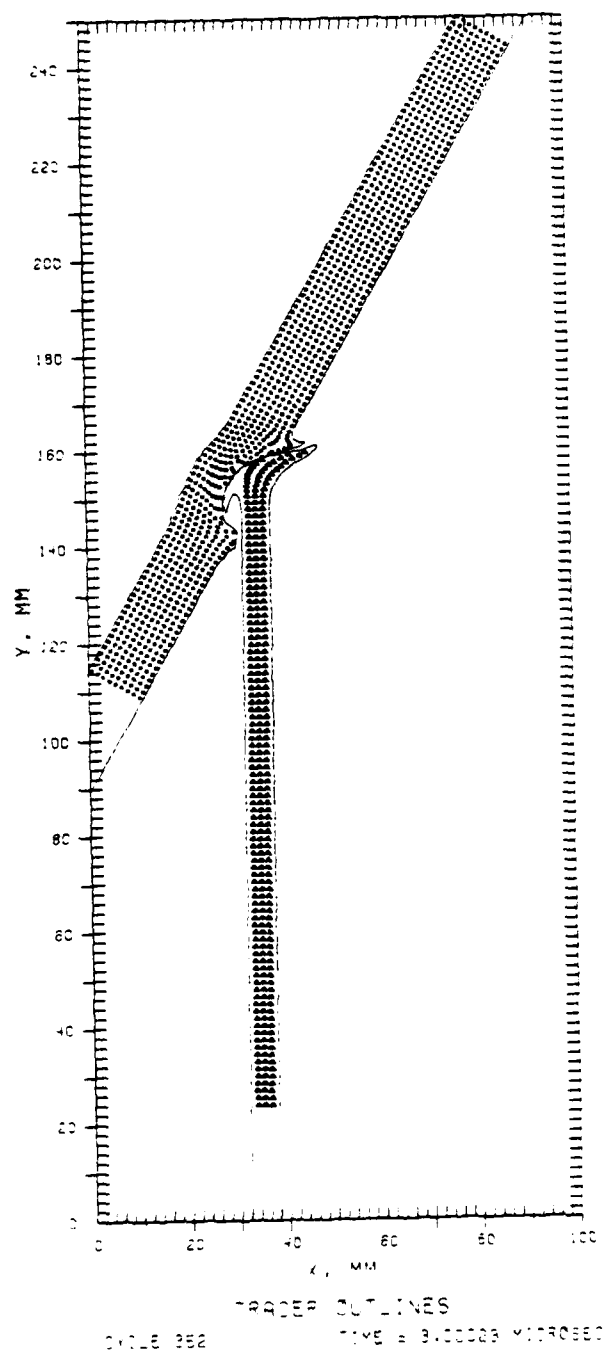


Figure 69. Penetrator-Target Deformation for 60° Oblique Impact

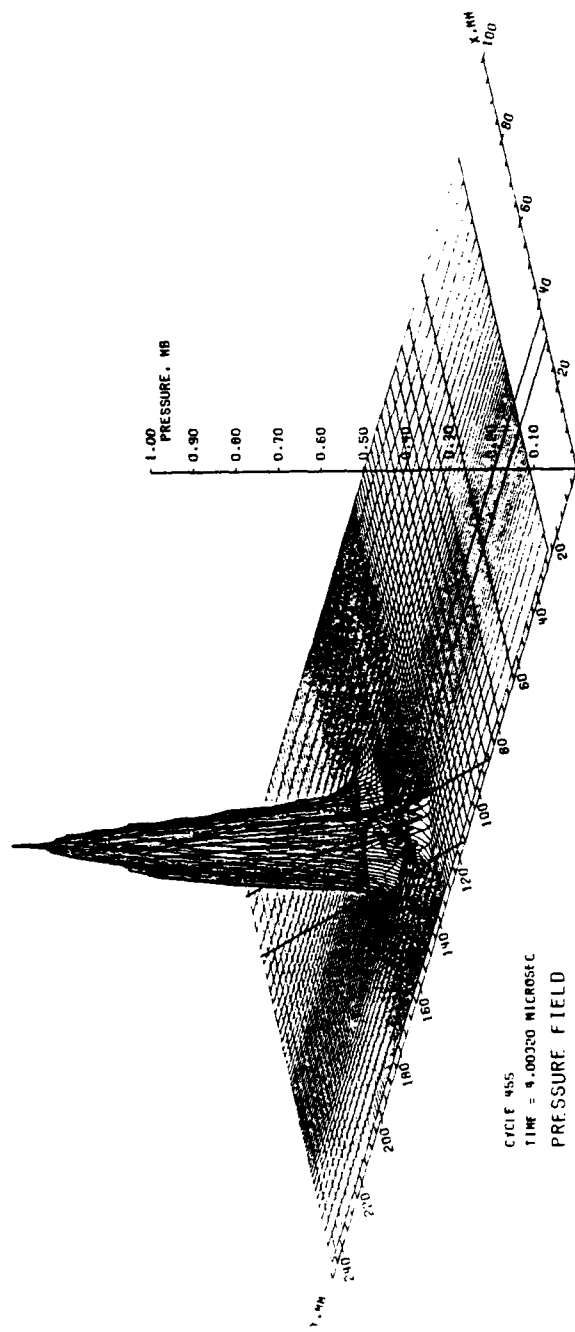


Figure 70. Pressure Field for 60° Oblique Impact

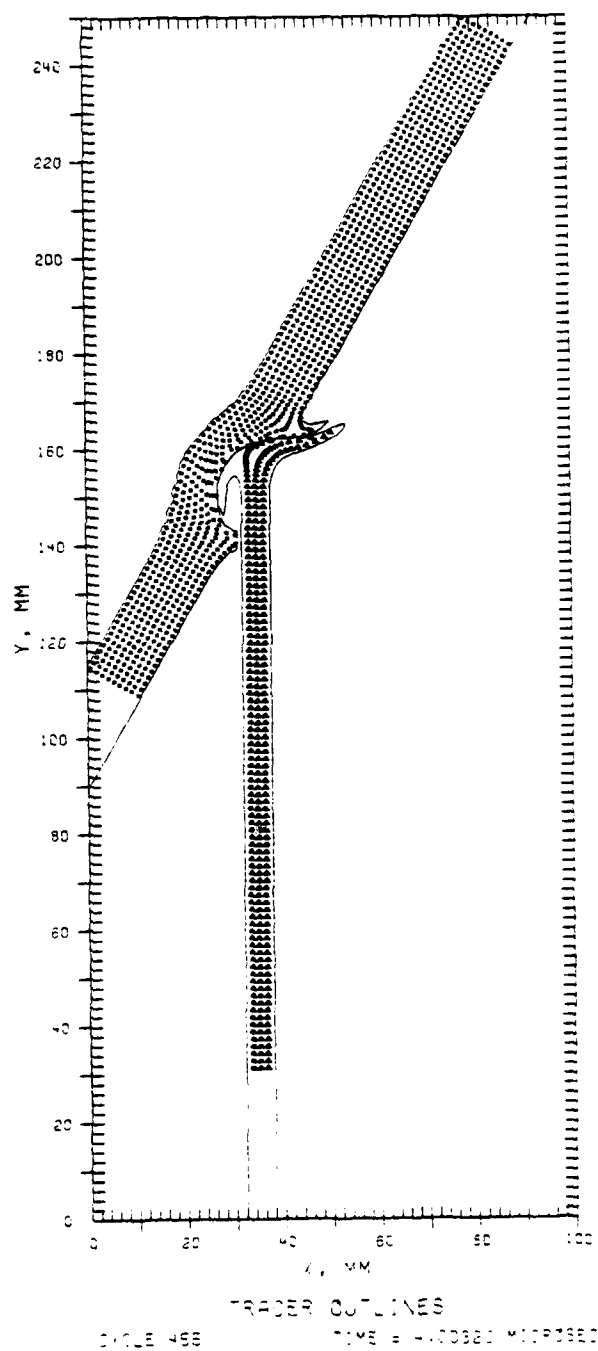


Figure 71. Penetrator-Target Deformation for 60° Oblique Impact

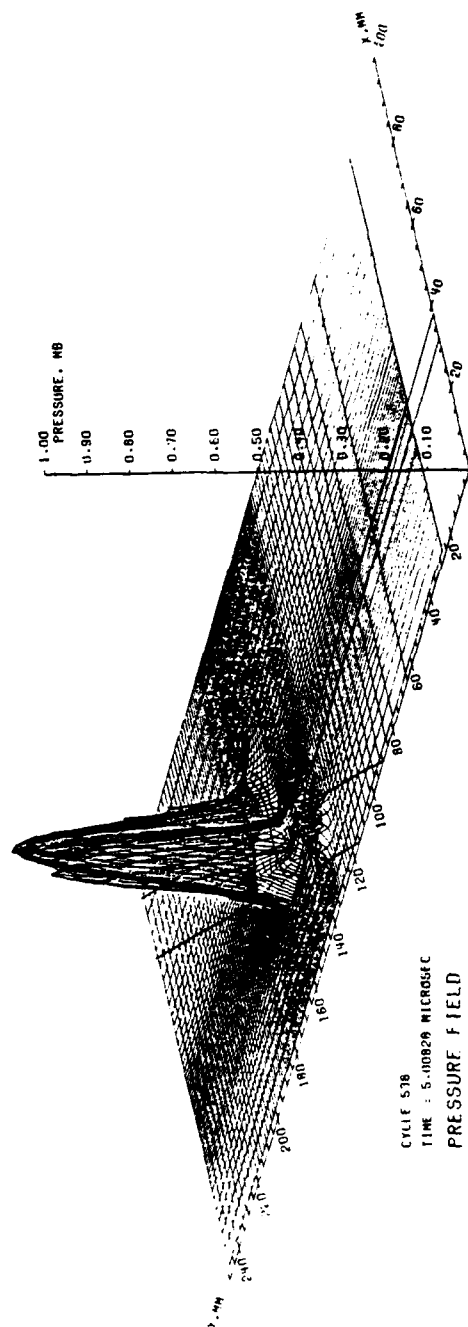


Figure 72. Pressure Field for 60° Oblique Impact

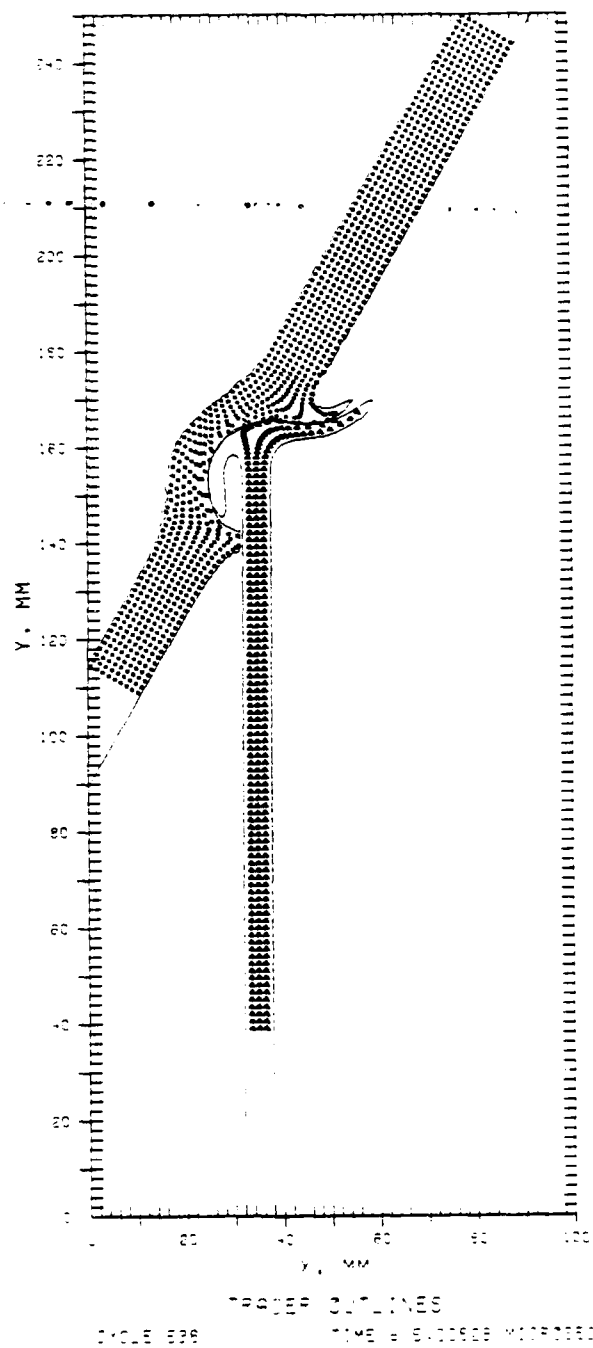


Figure 73. Penetrator-Target Deformation for 60° Oblique Impact

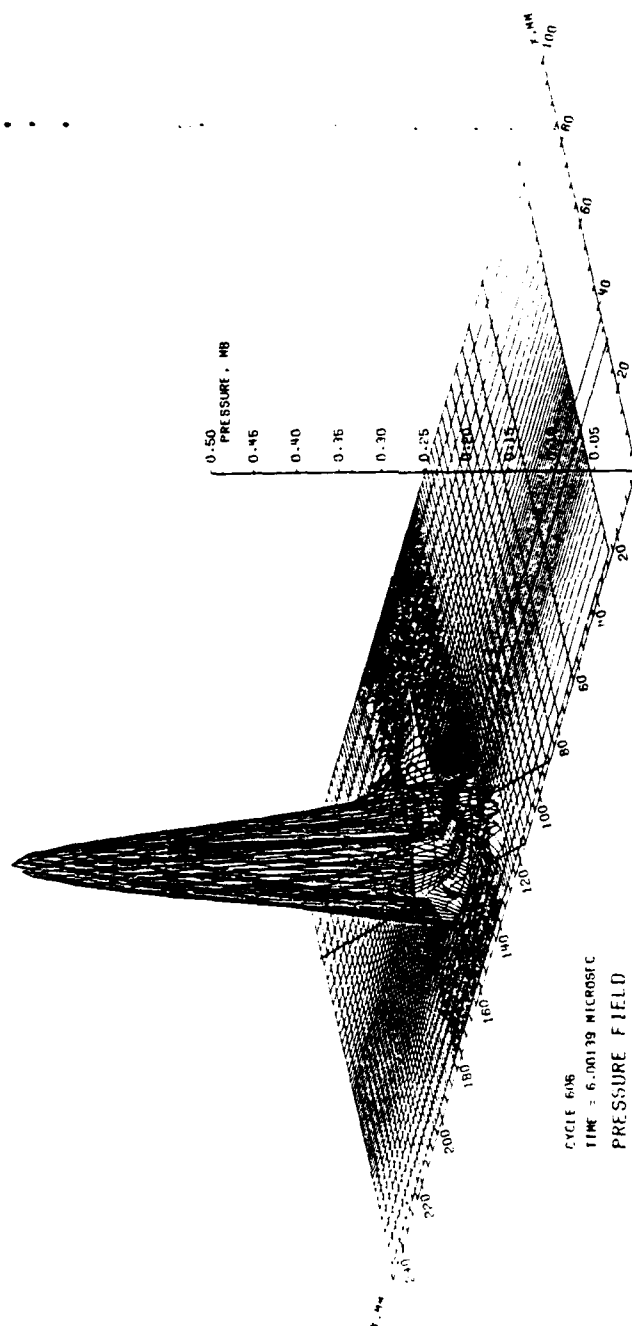


Figure 74. Pressure Field for 60° Oblique Impact

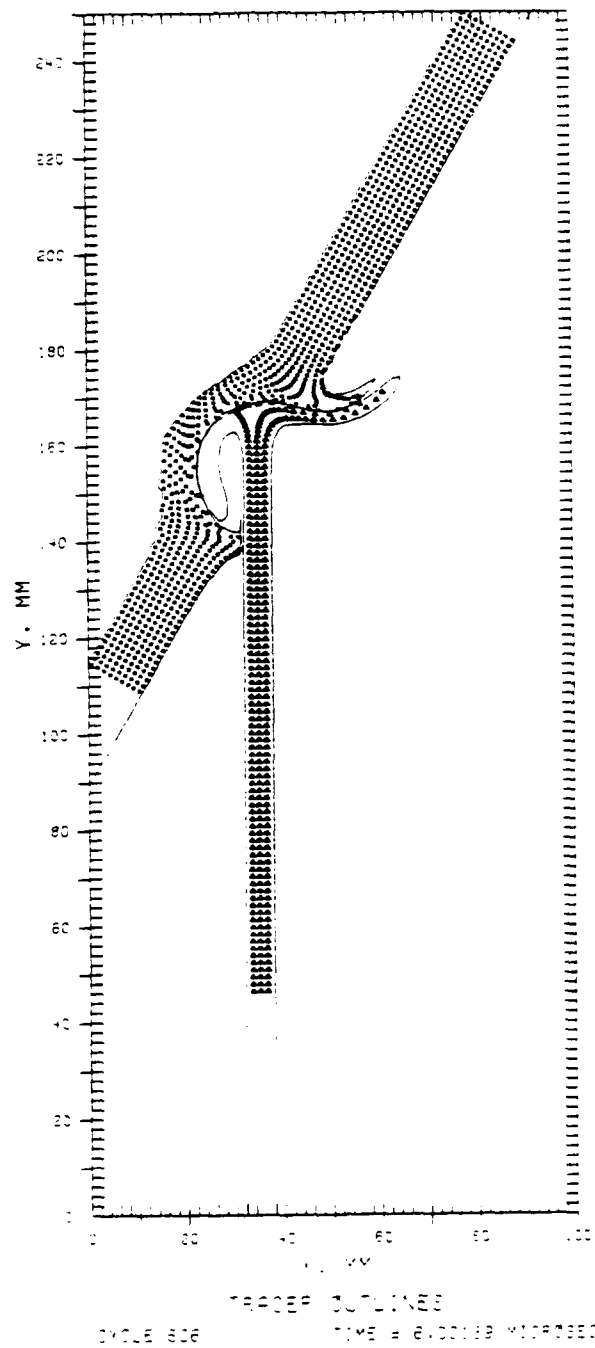


Figure 75. Penetrator-Target Deformation for 60° Oblique Impact

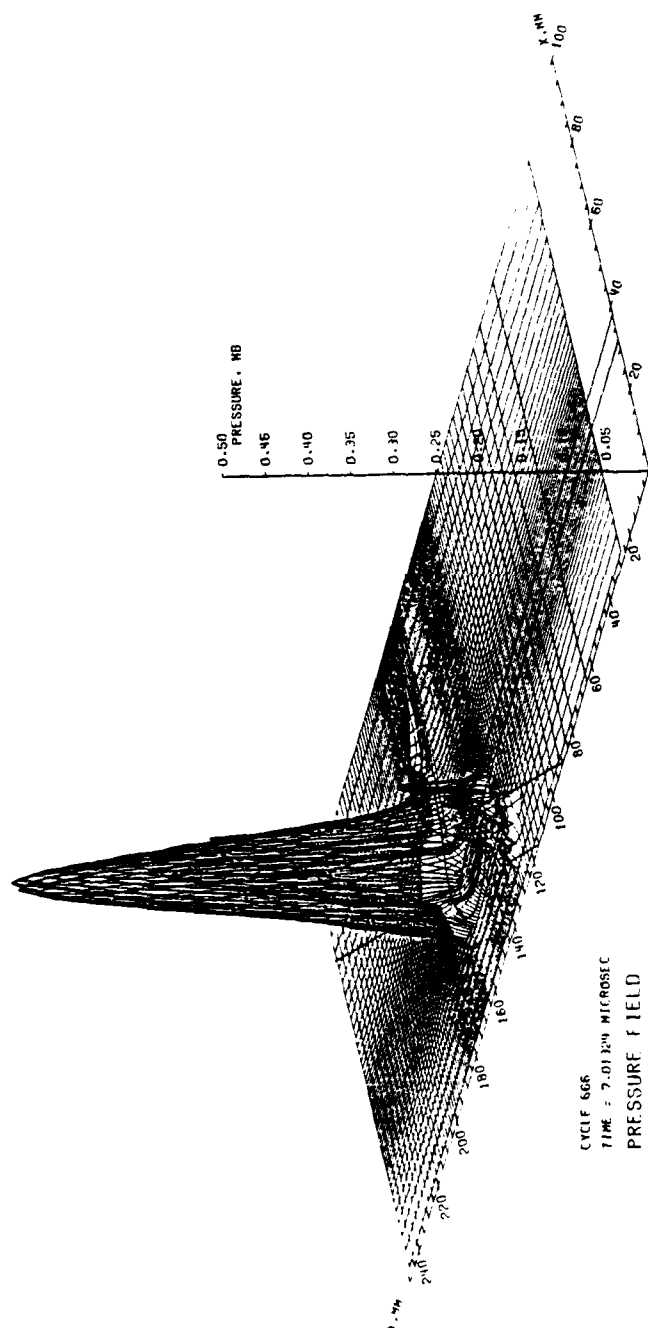


Figure 76. Pressure Field for 60° Oblique Impact

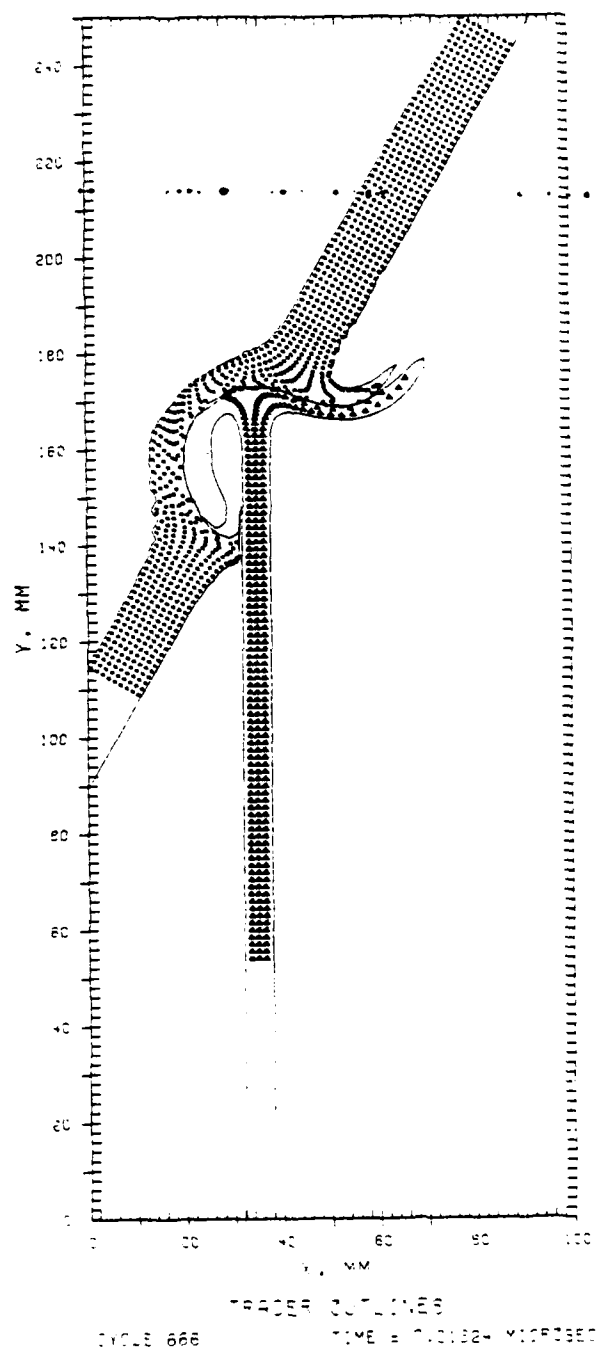


Figure 77. Penetrator-Target Deformation for 60° Oblique Impact

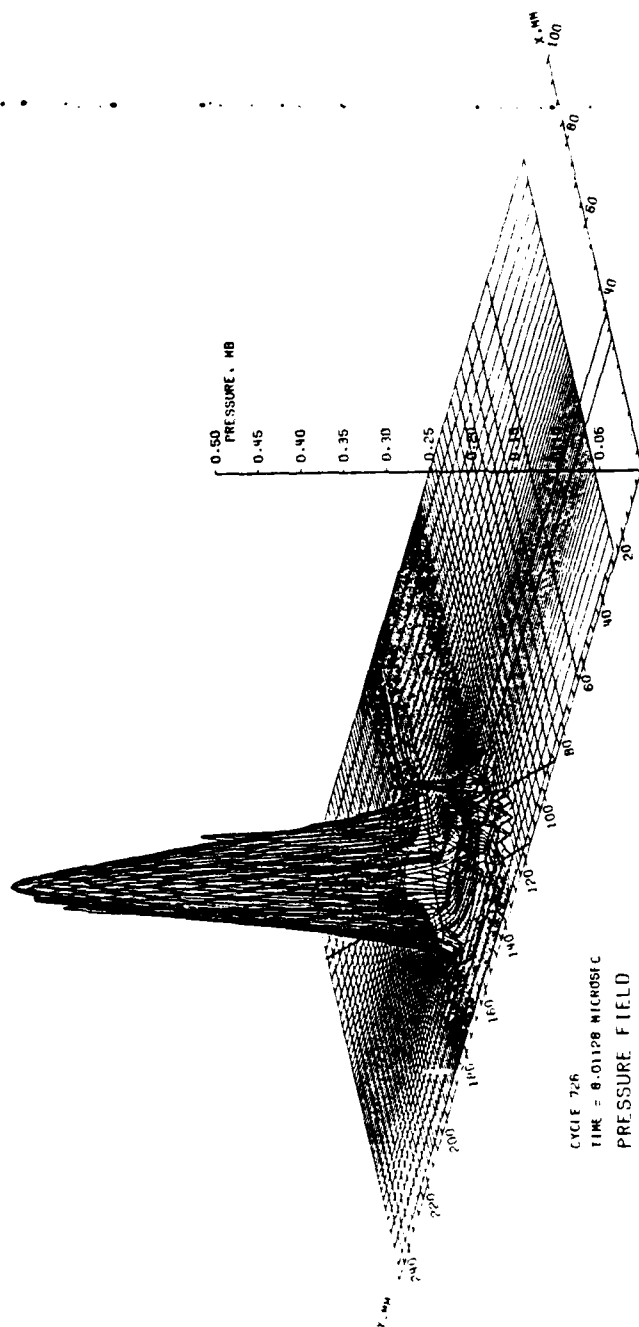


Figure 78. Pressure Field for 60° Oblique Impact

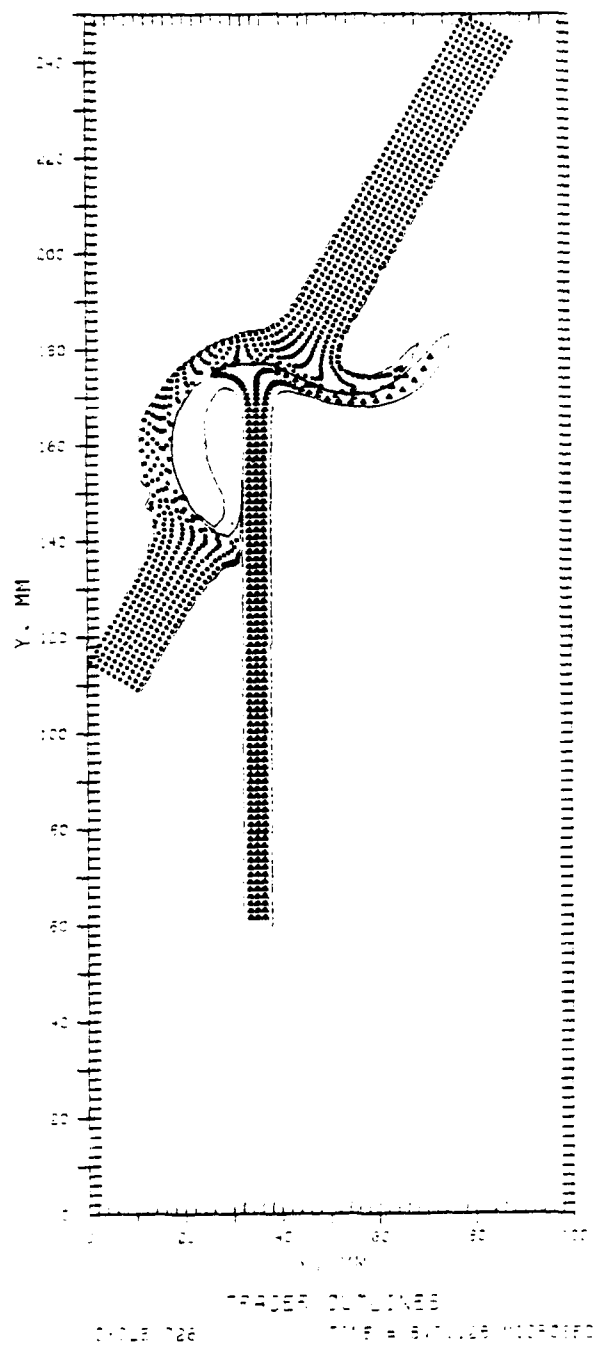


Figure 79. Penetrator-Target Deformation for 60° Oblique Impact

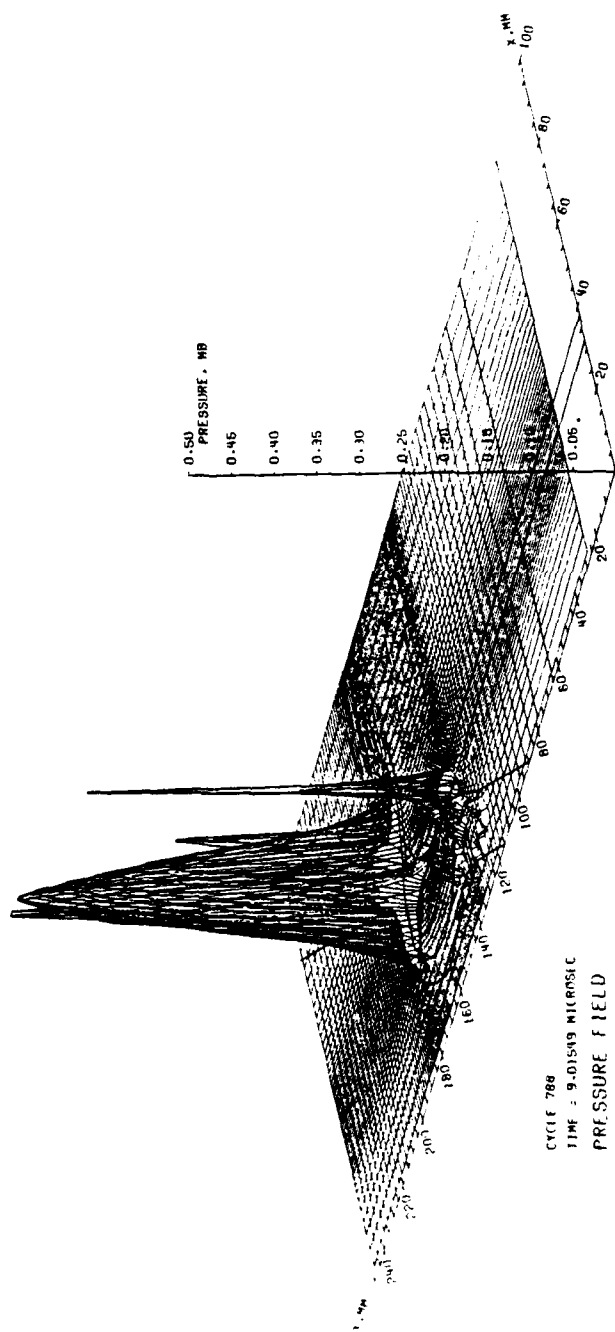


Figure 80. Pressure Field for 60° Oblique Impact

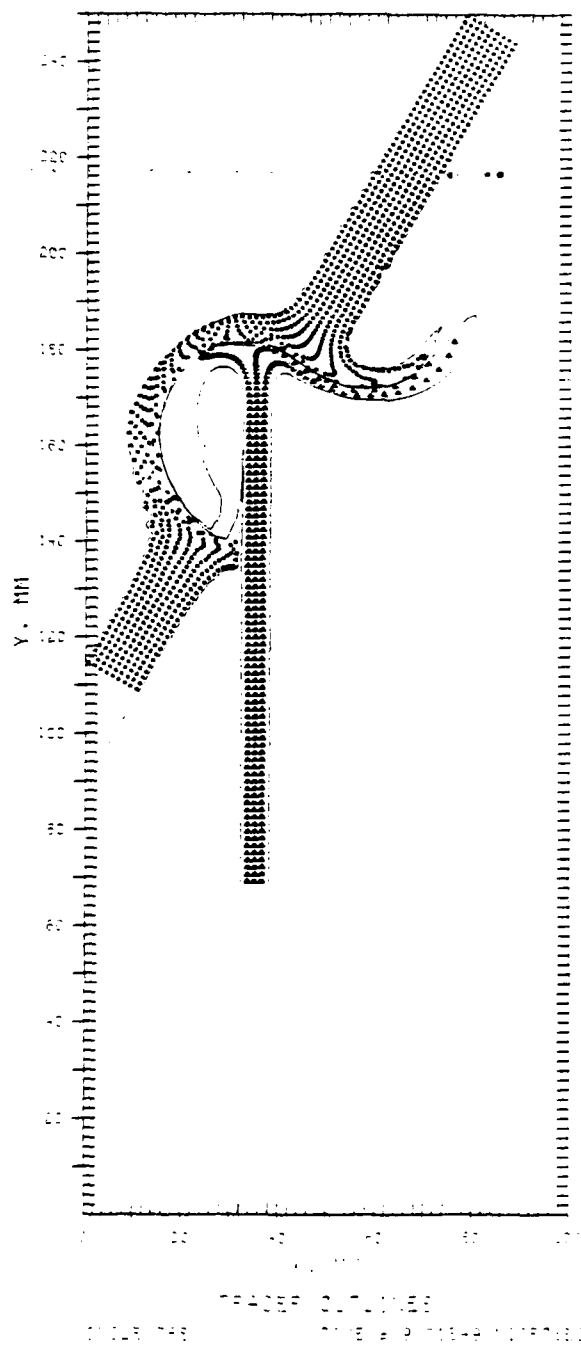


Figure 81. Penetrator-Target Deformation for 60° Oblique Impact

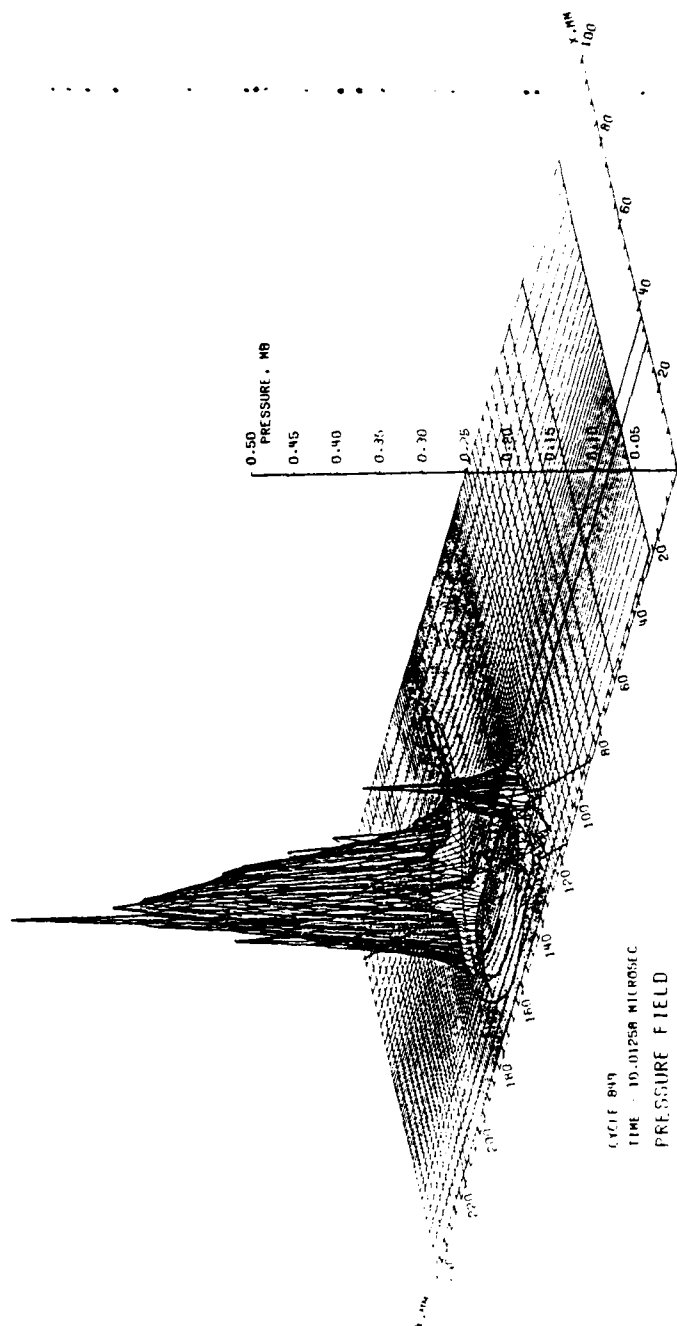


Figure 82. Pressure Field for 60° Oblique Impact

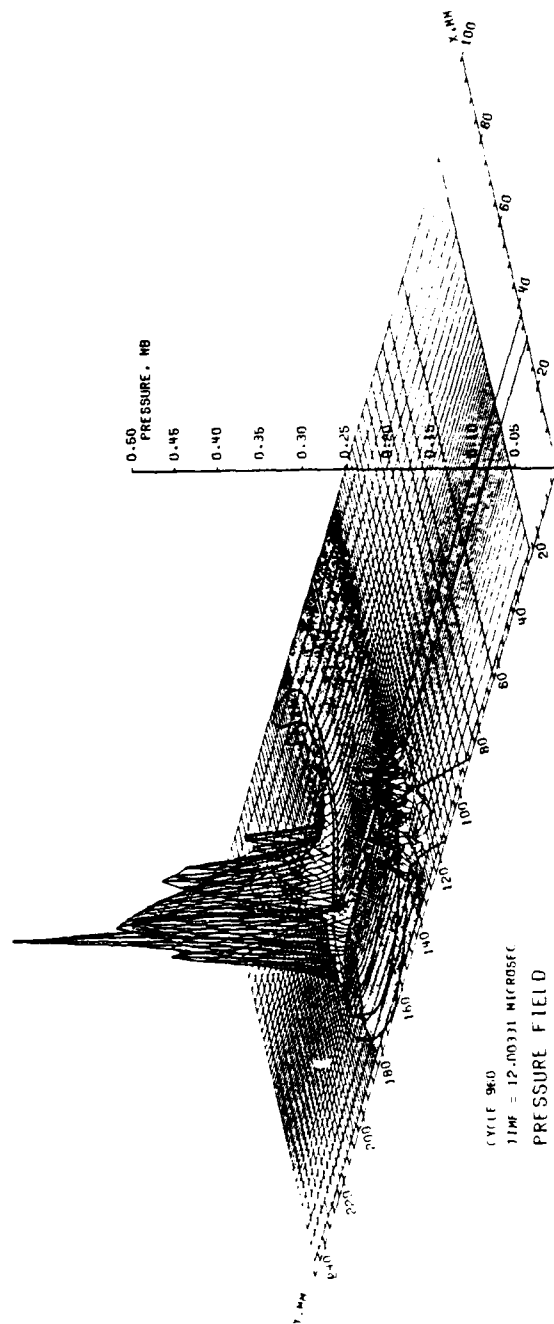


Figure 84. Pressure Field for 60° Oblique Impact

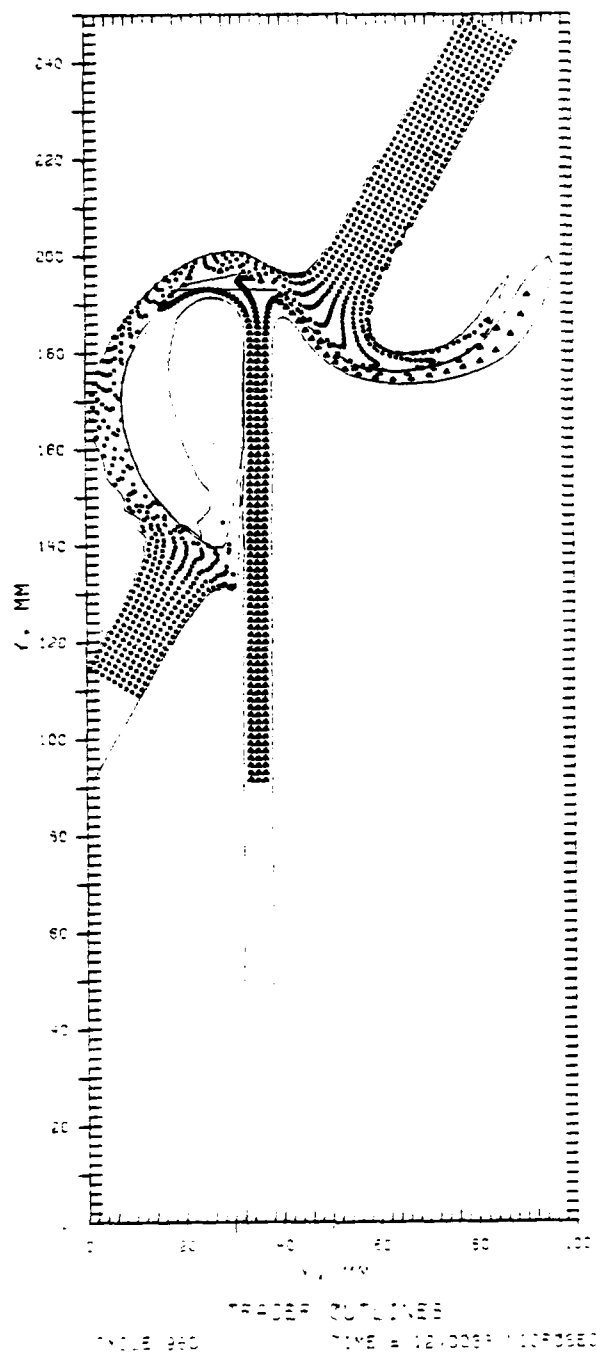


Figure 85. Penetrator-Target Deformation for 60° Oblique Impact

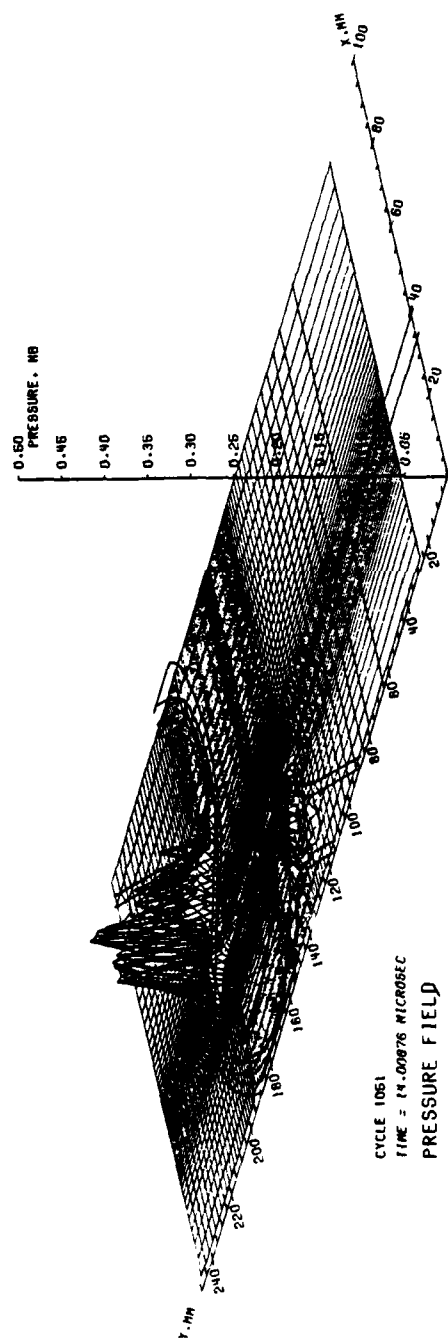


Figure 86. Pressure Field for 60° Oblique Impact

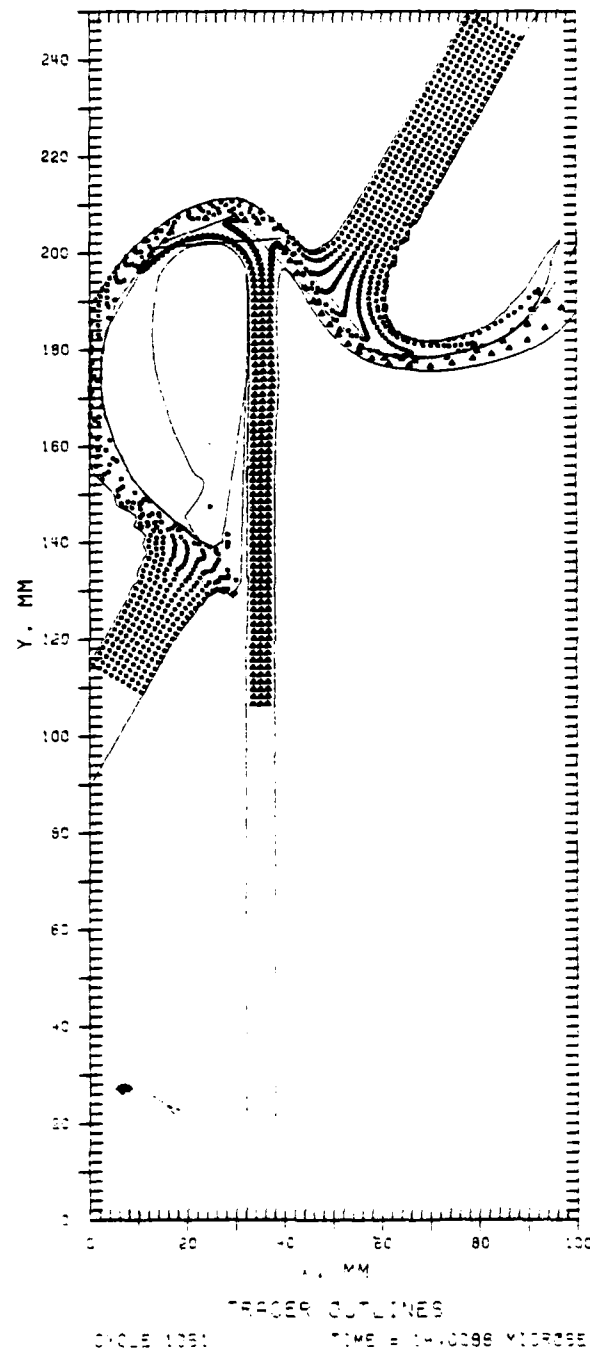


Figure 87. Penetrator-Target Deformation for 60° Oblique Impact

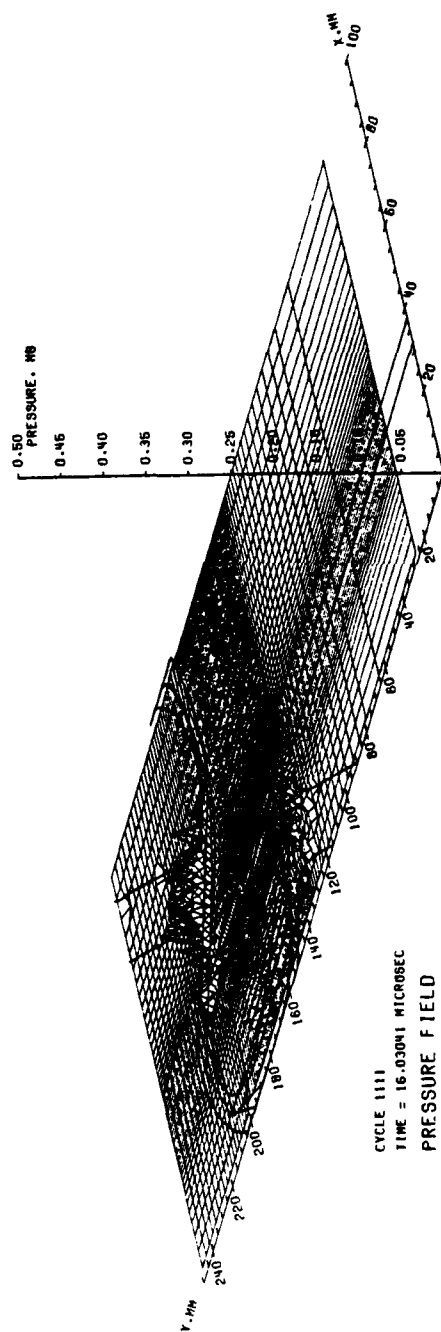


Figure 88. Pressure Field for 60° Oblique Impact

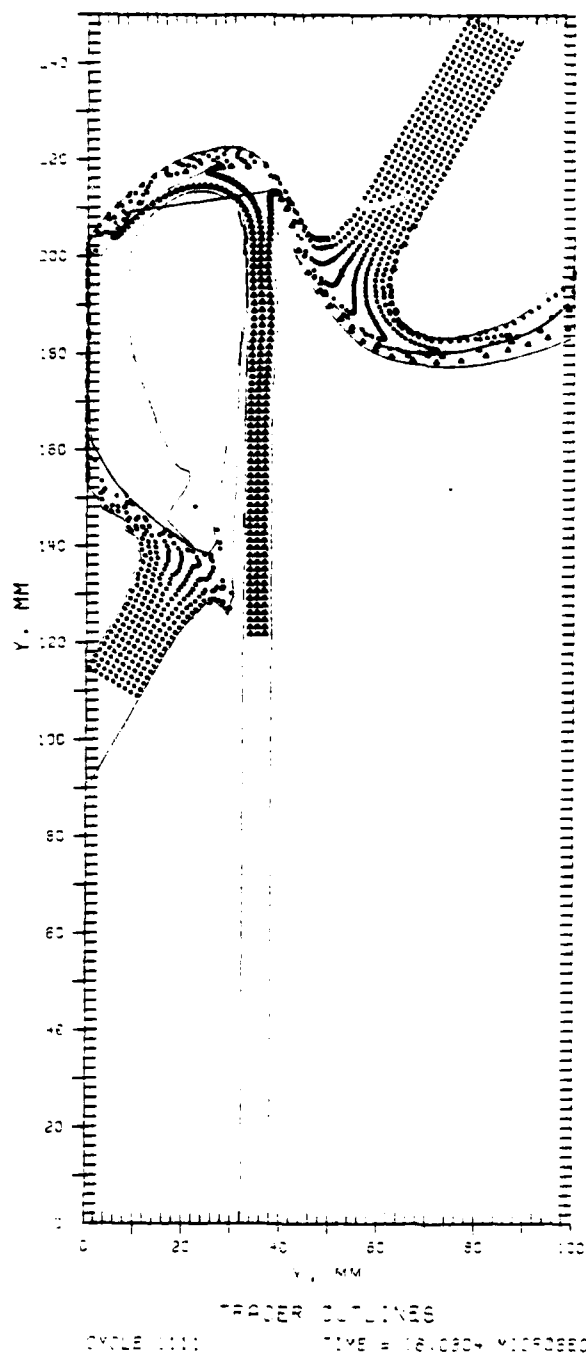


Figure 89. Penetrator-Target Deformation for 60° Oblique Impact

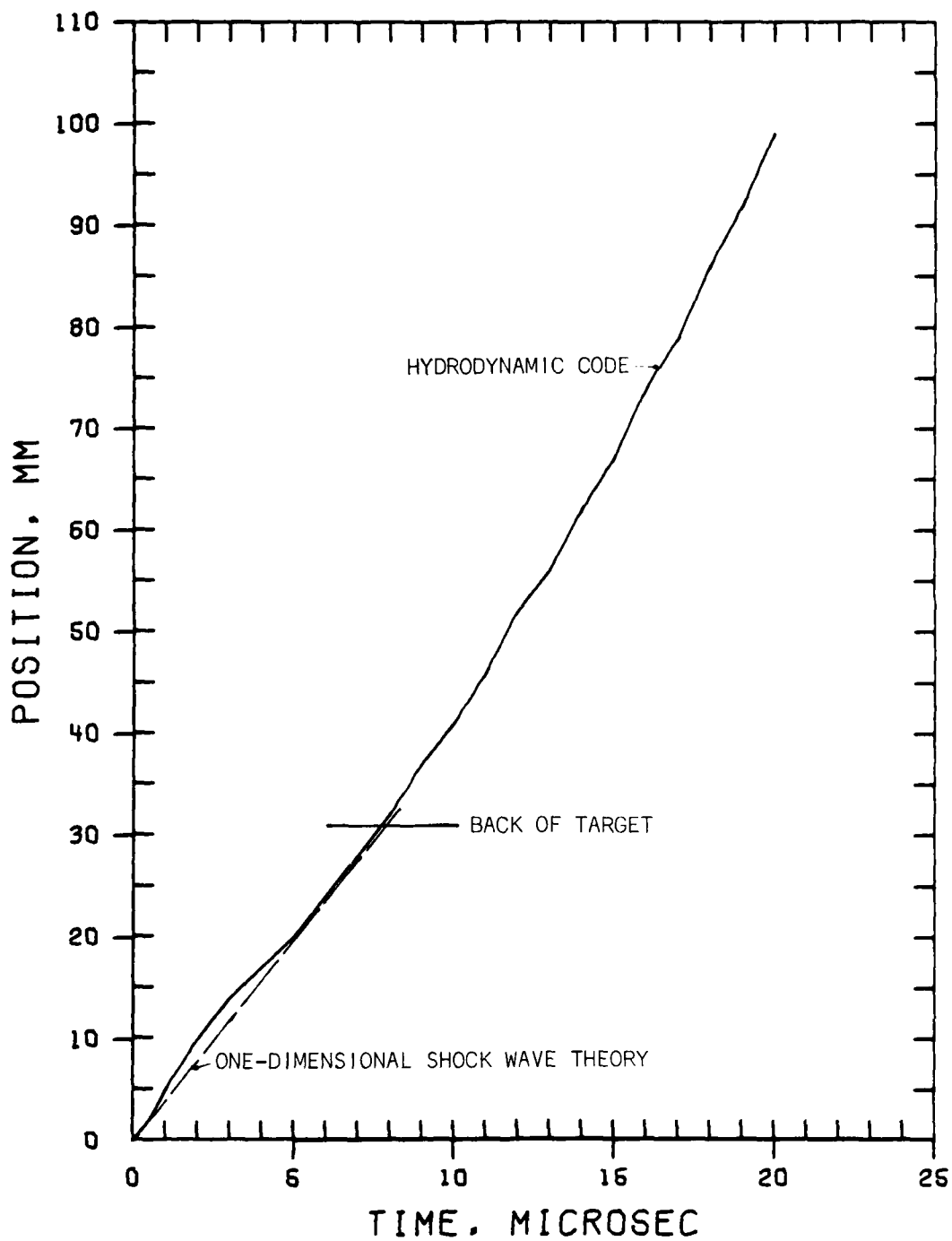


Figure 90. Penetration History for 60° Oblique Impact

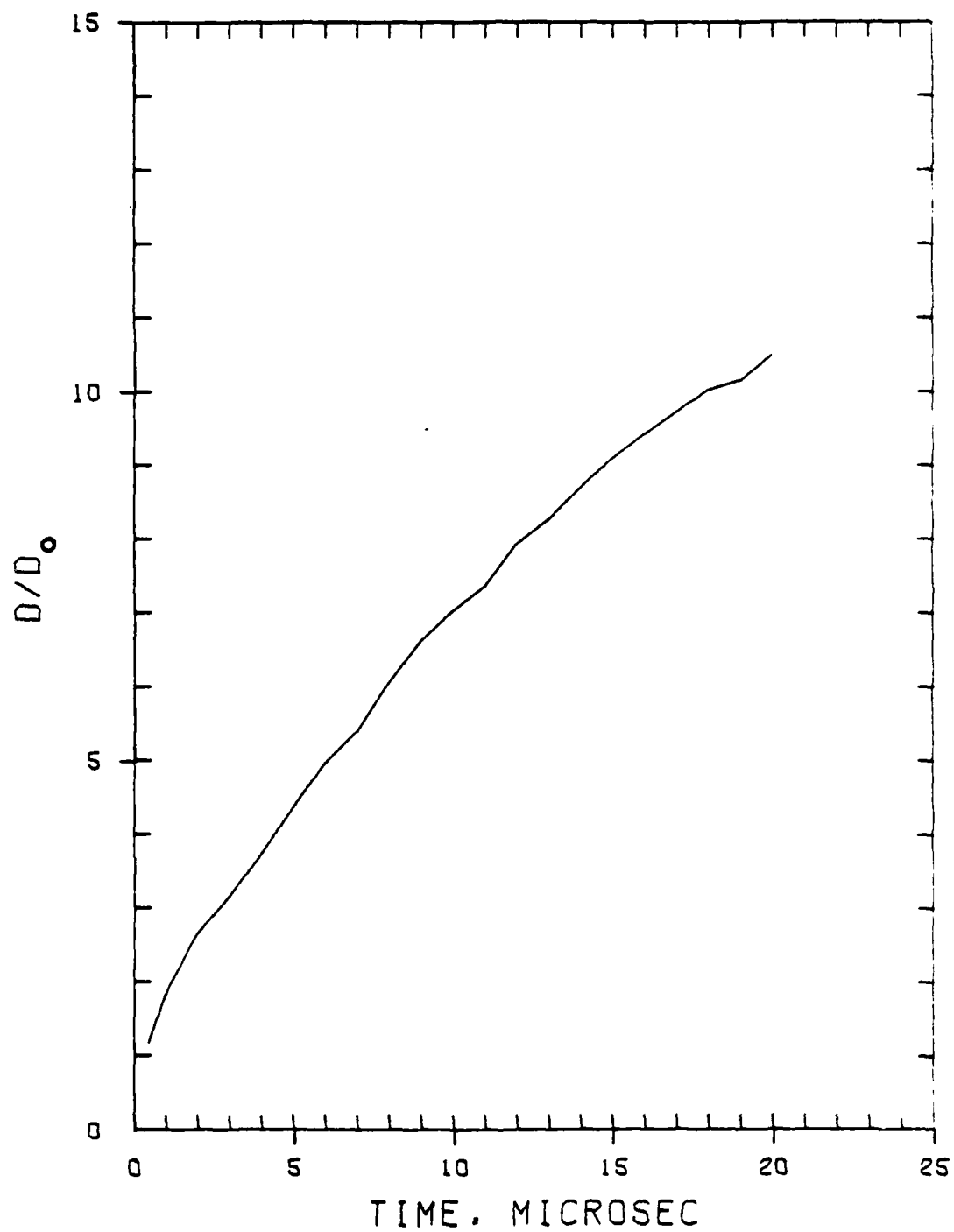


Figure 91. Growth of the Front Face Cut for 60° Oblique Impact

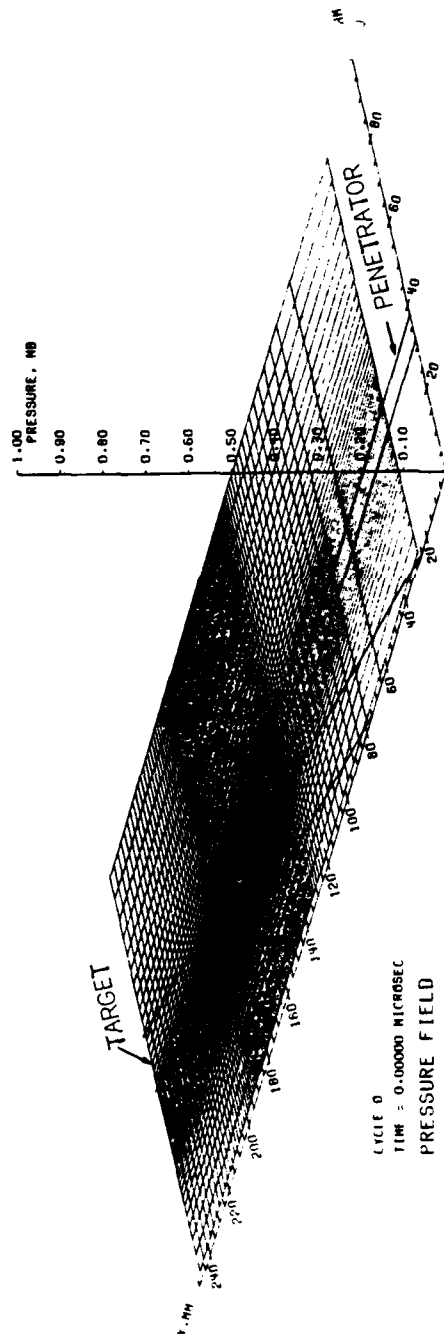


Figure 92. Pressure Field for 75° Oblique Impact

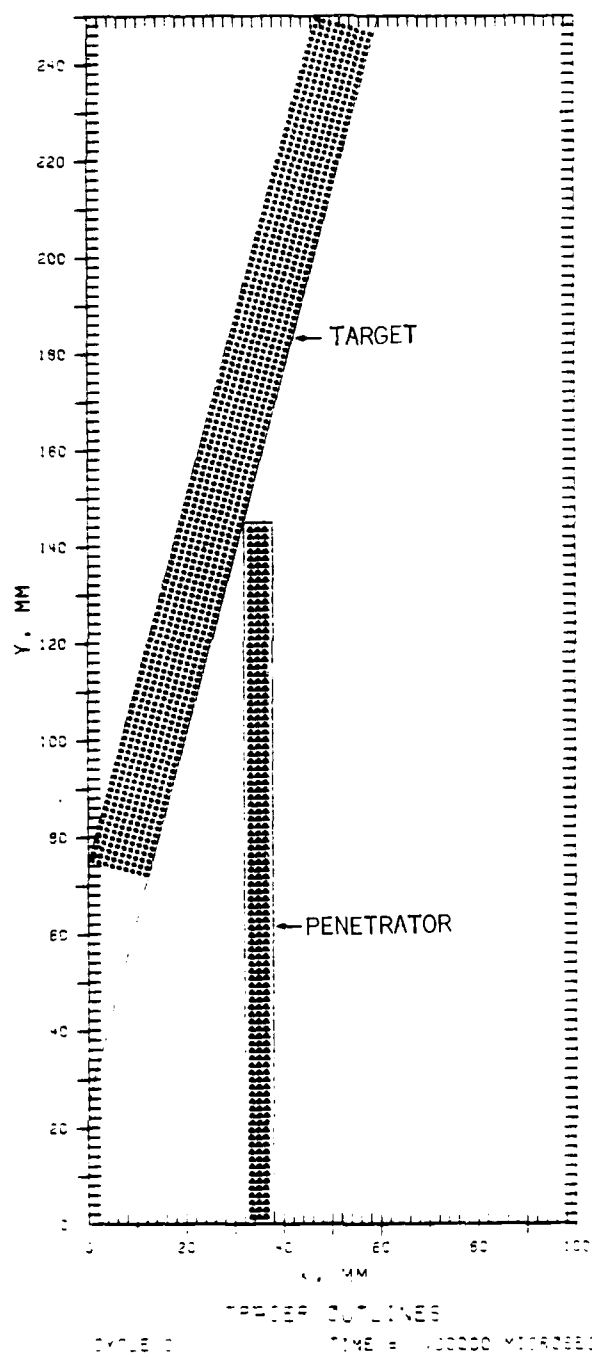


Figure 93. Penetrator-Target Deformation for 75° Oblique Impact

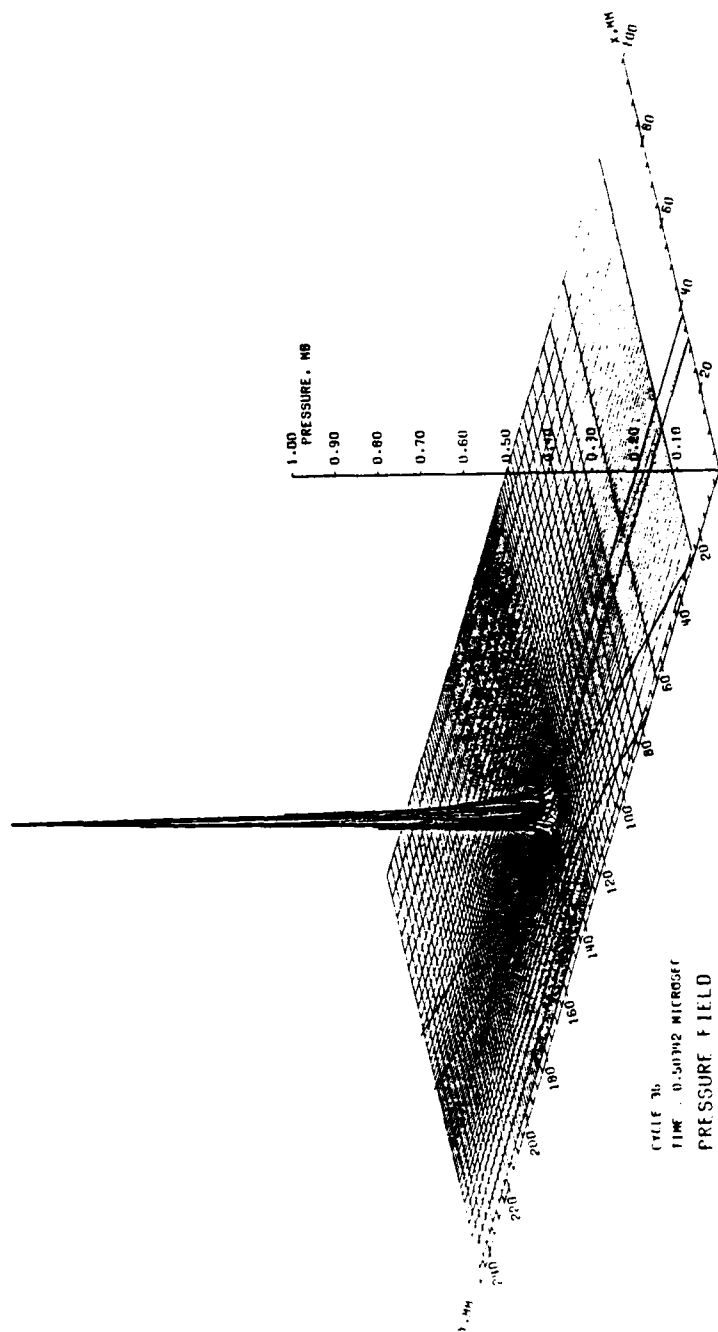


Figure 94. Pressure Field for 75° Oblique Impact

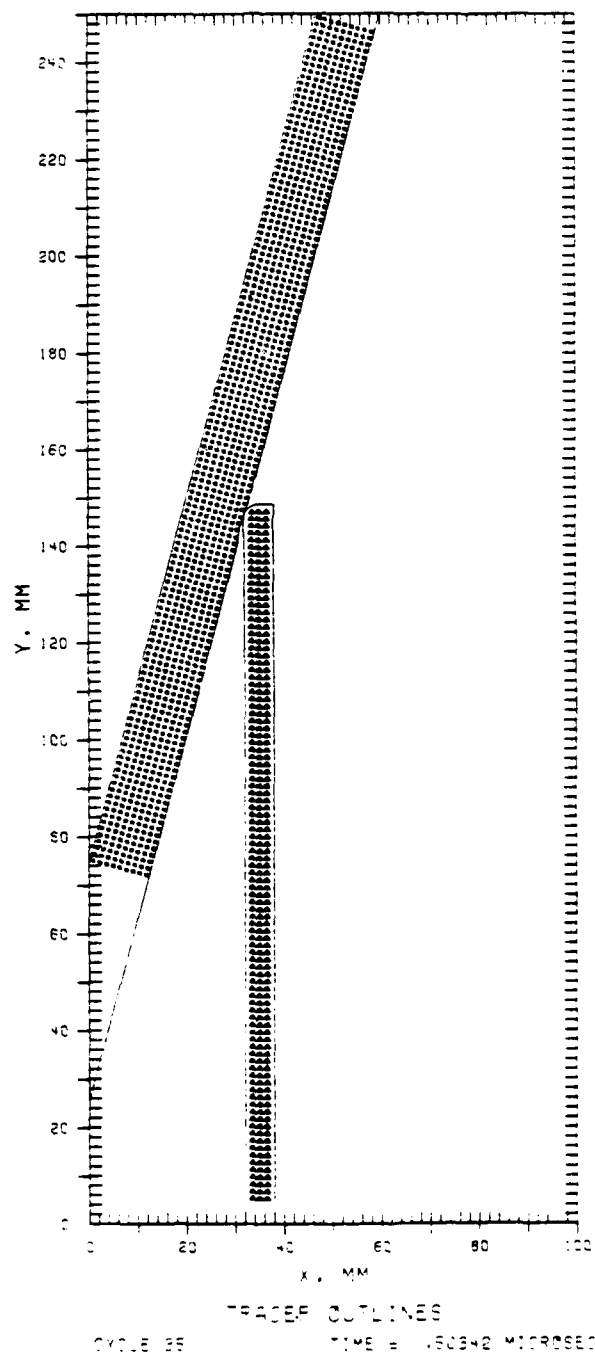


Figure 95. Penetrator-Target Deformation for 75° Oblique Impact

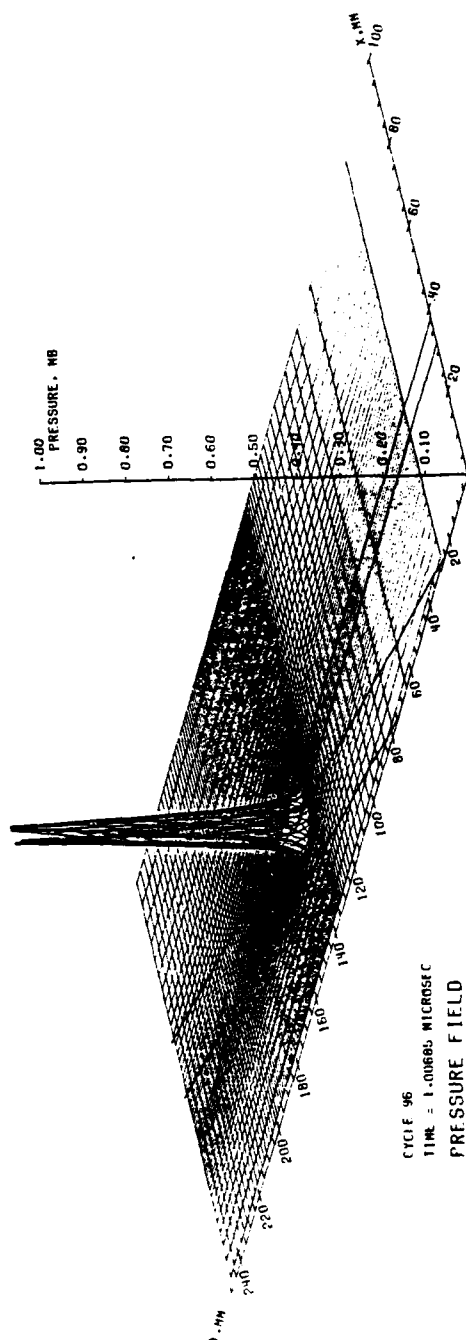


Figure 96. Pressure Field for 75° Oblique Impact

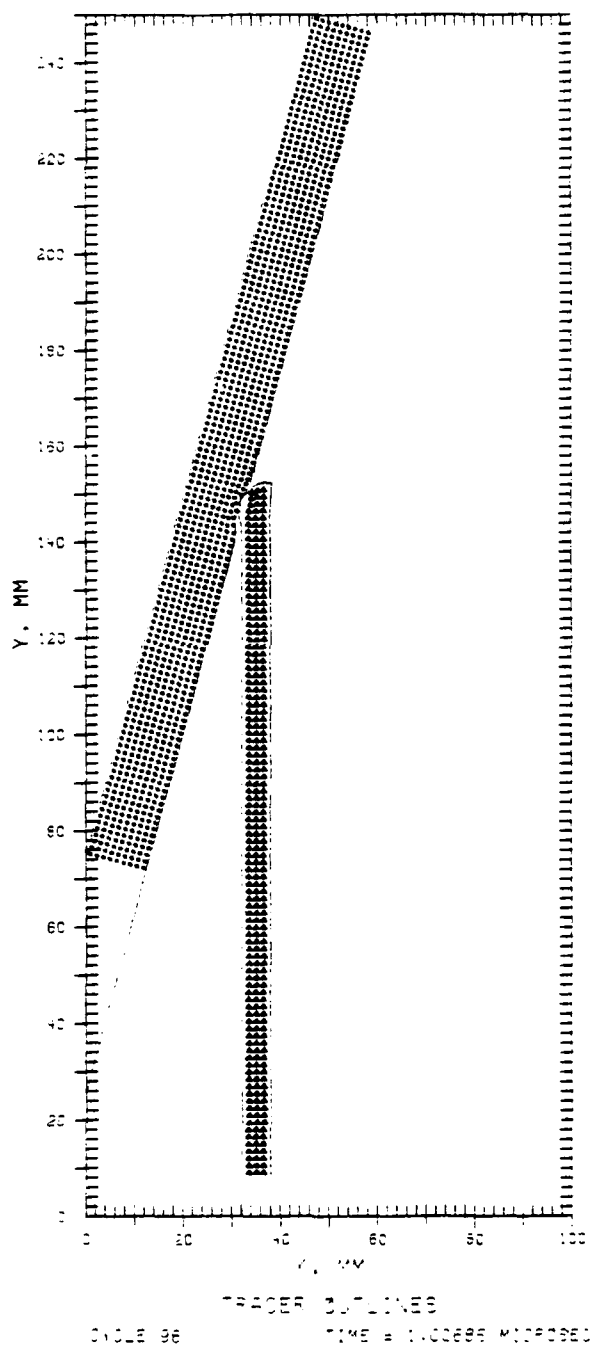


Figure 97. Penetrator-Target Deformation for 75° Oblique Impact

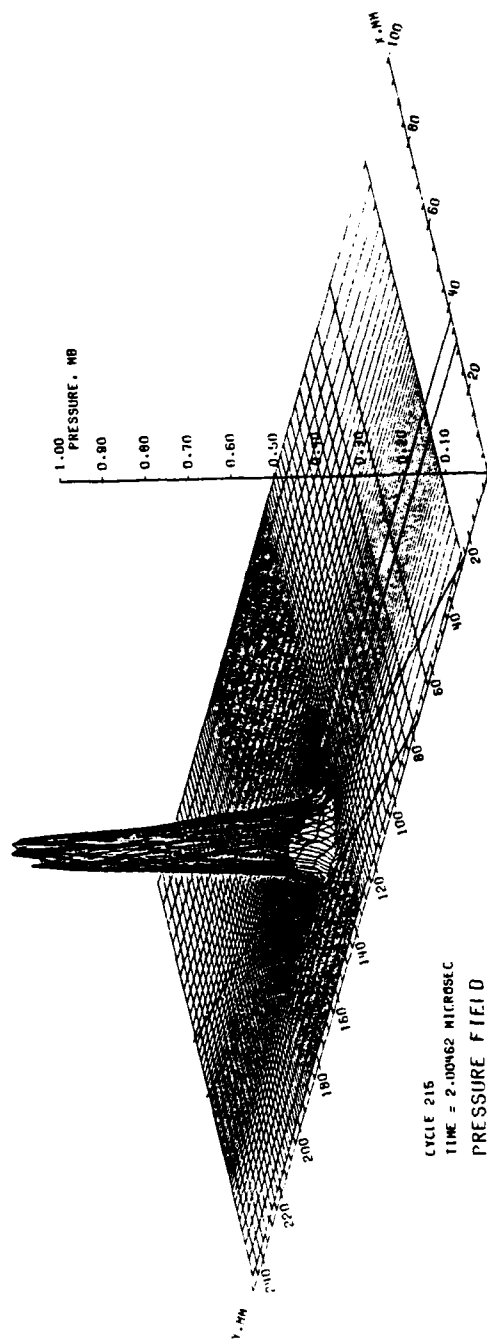
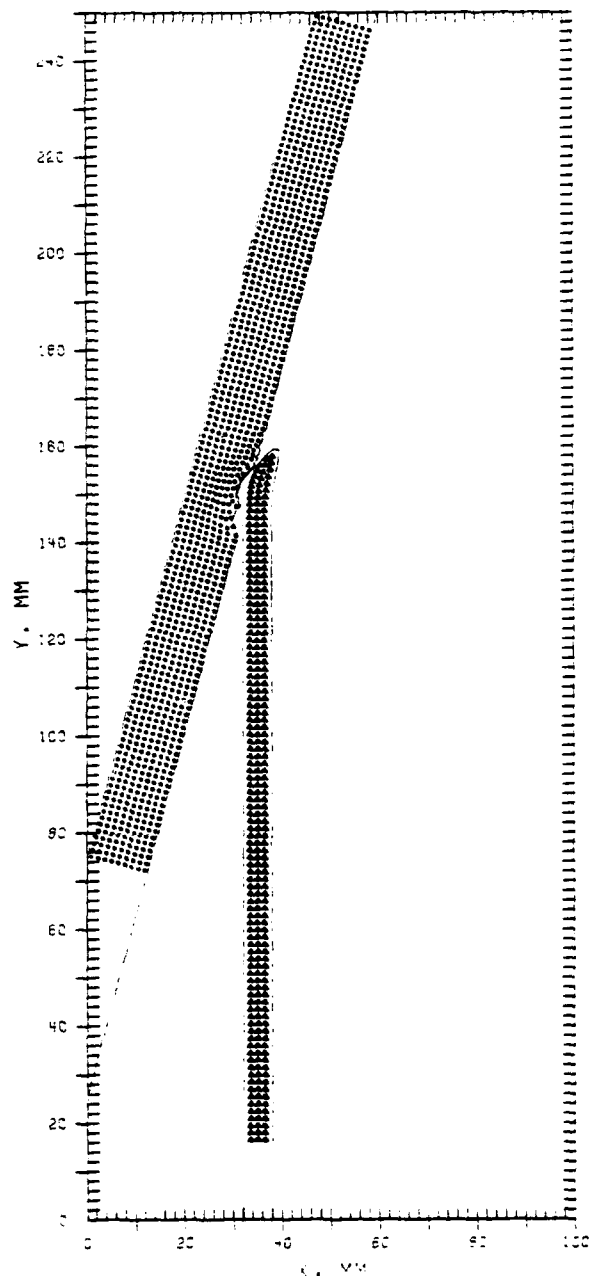


Figure 98. Pressure Field for 75° Oblique Impact



TRACER OUTLINES
 CYCLE 215 TIME = 2.00+60 MICROSEC

Figure 99. Penetrator-Target Deformation for 75° Oblique Impact

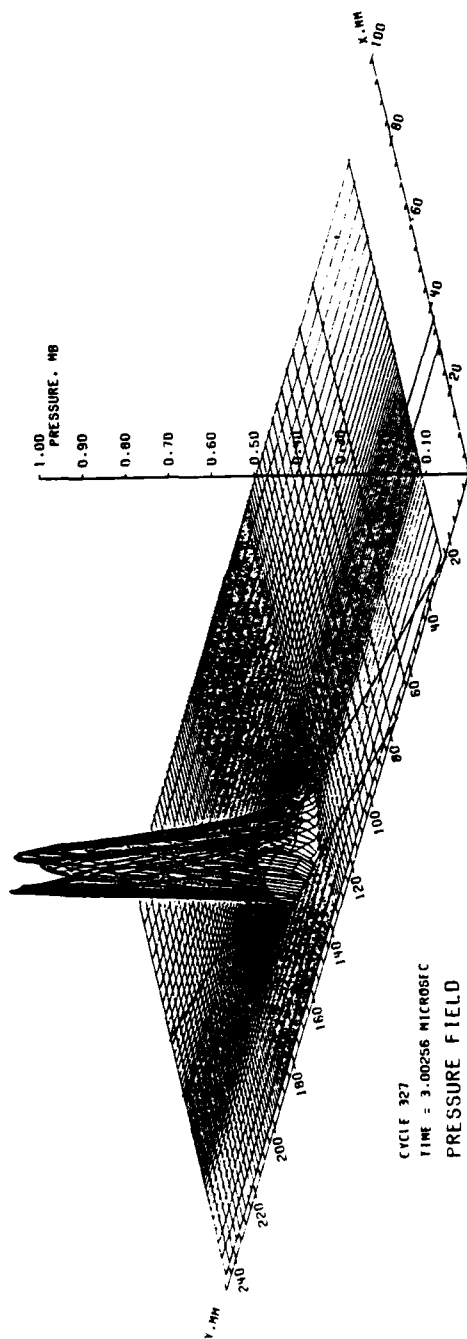


Figure 100. Pressure Field for 75° Oblique Impact

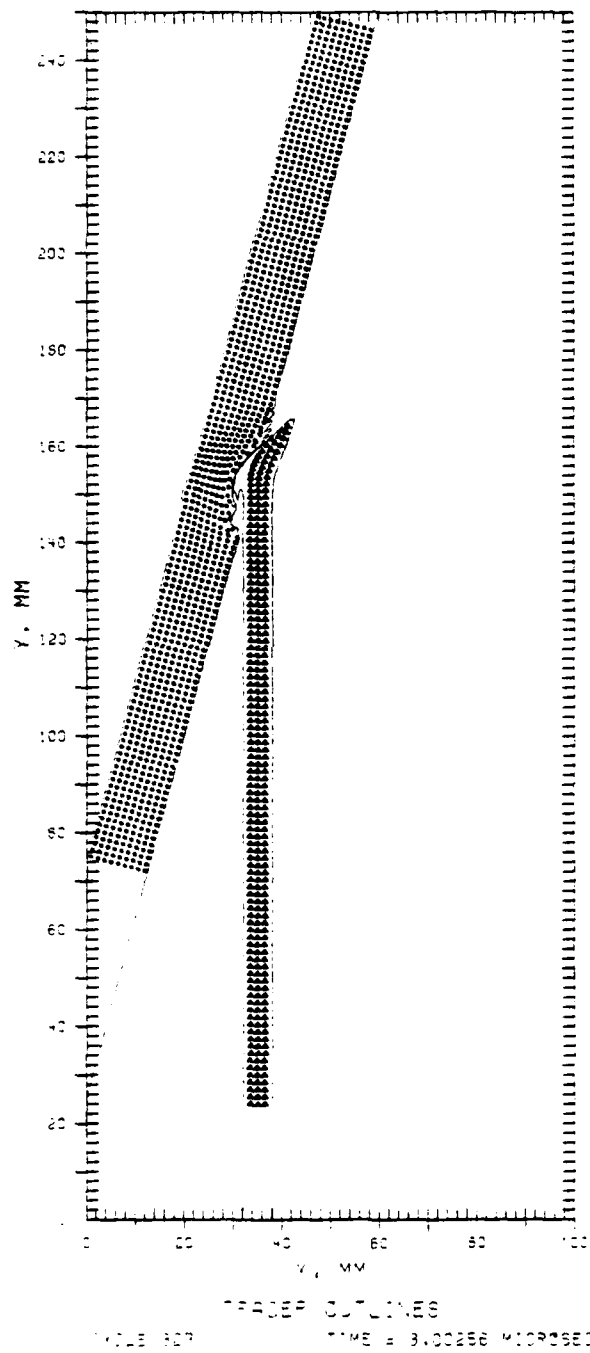


Figure 101. Penetrator-Target Deformation for 75° Oblique Impact

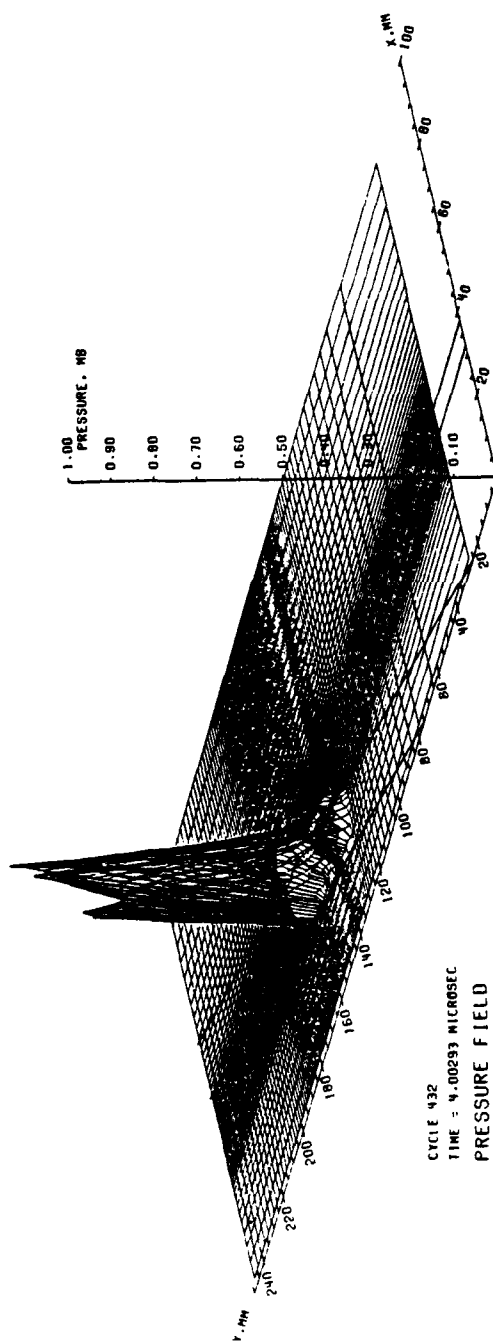


Figure 102. Pressure Field for 75° Oblique Impact

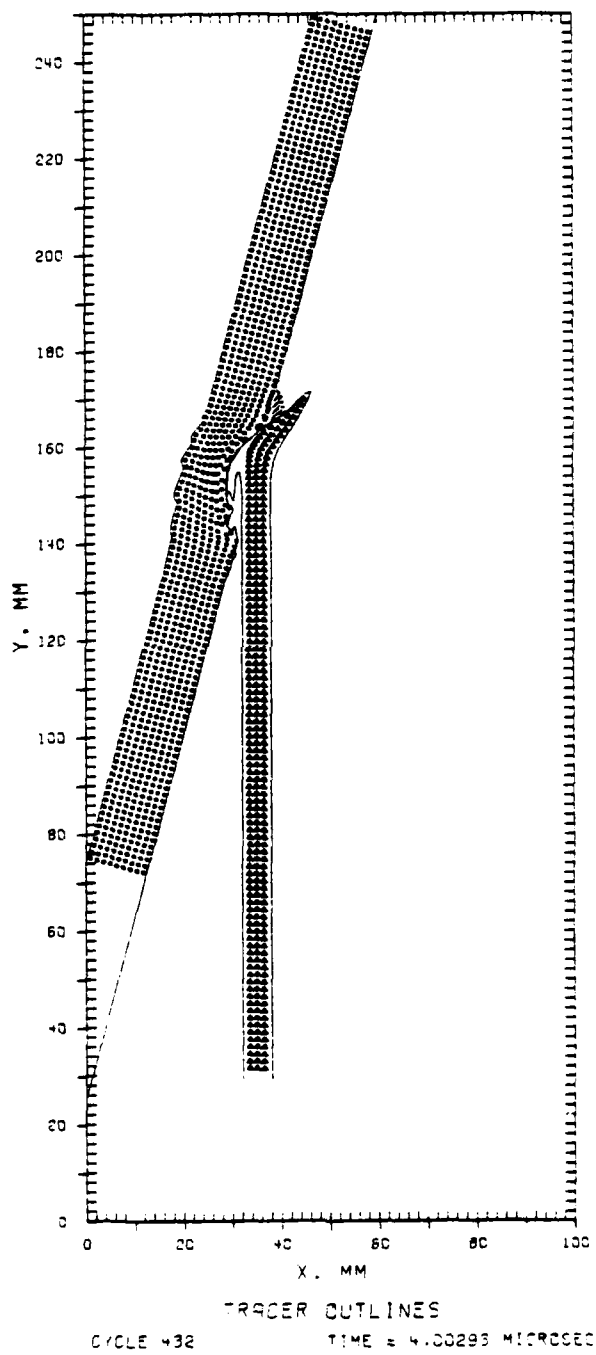


Figure 103. Penetrator-Target Deformation for 75° Oblique Impact

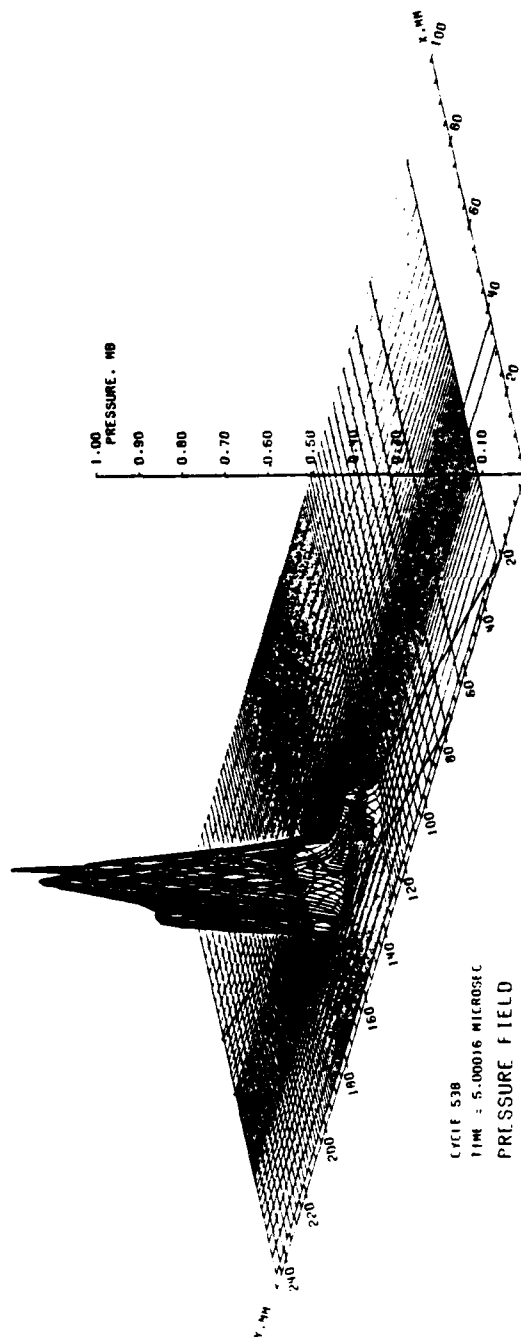


Figure 104. Pressure Field for 75° Oblique Impact

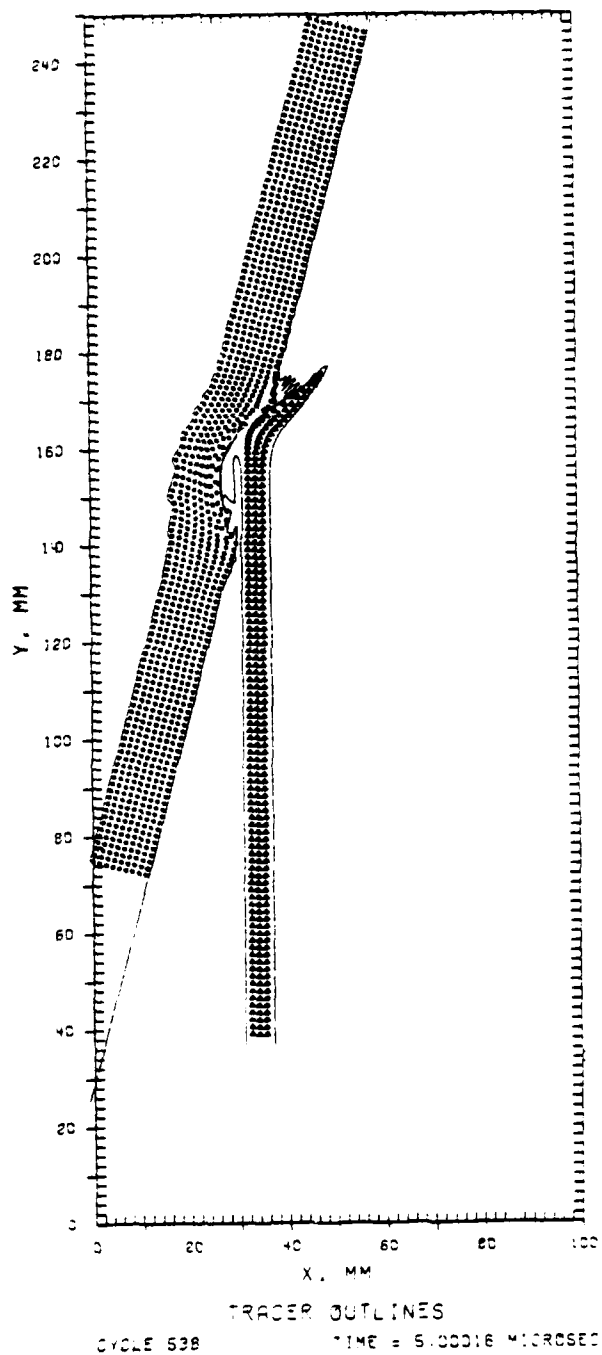


Figure 105. Penetrator-Target Deformation for 75° Oblique Impact

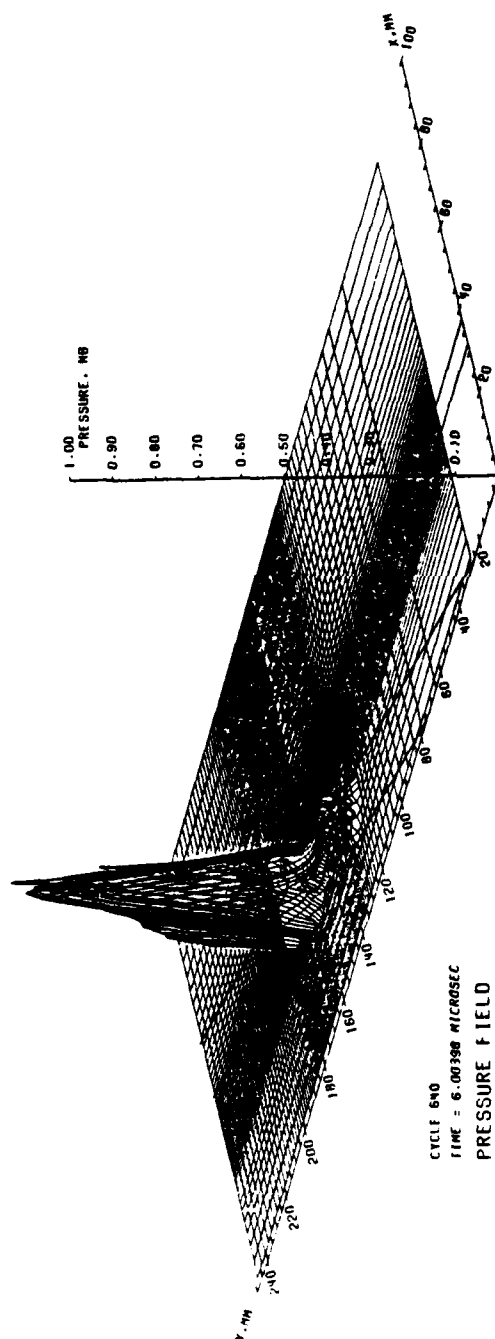


Figure 106. Pressure Field for 75° Oblique Impact

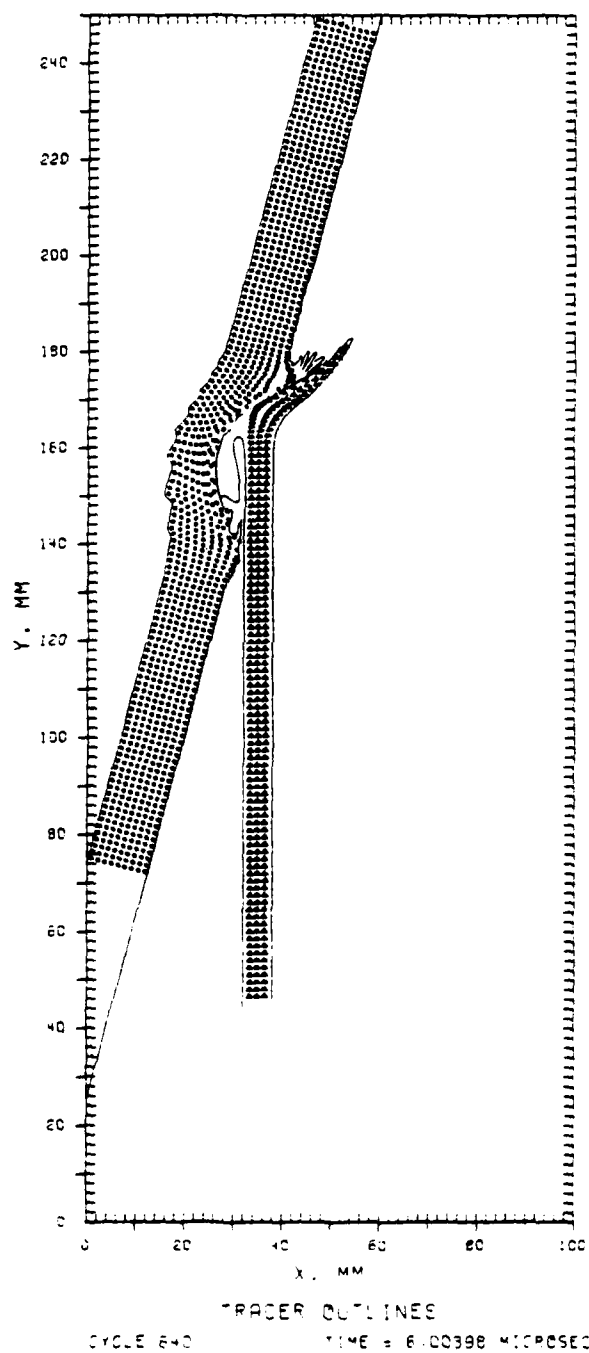


Figure 107. Penetrator-Target Deformation for 75° Oblique Impact

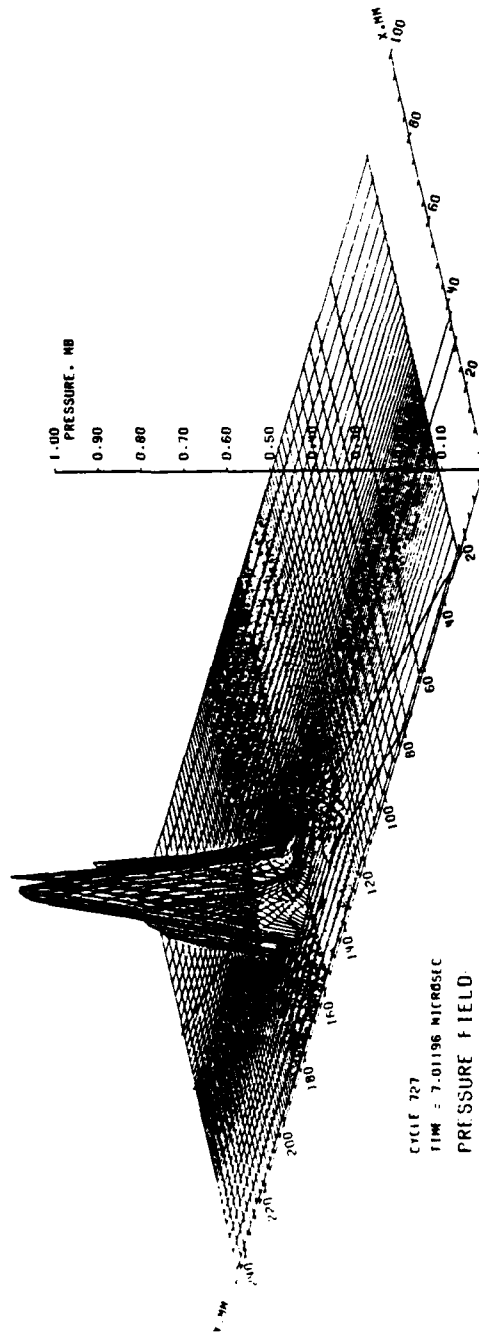


Figure 108. Pressure Field for 75° Oblique Impact

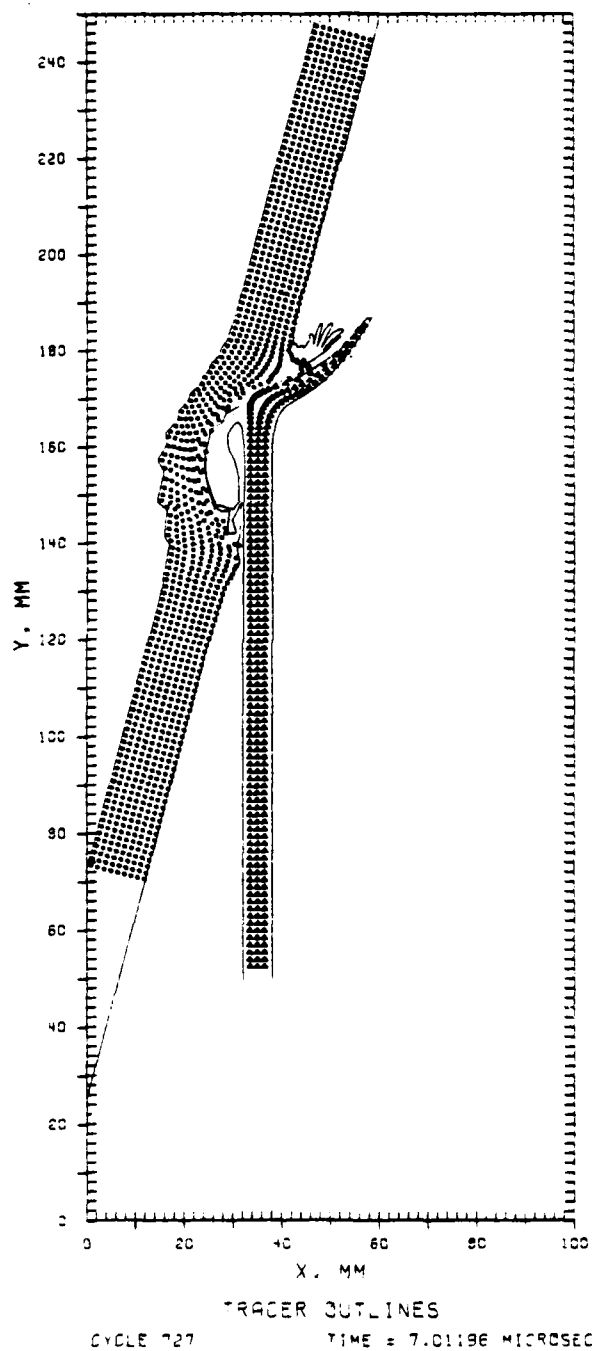


Figure 109. Penetrator-Target Deformation for 75° Oblique Impact

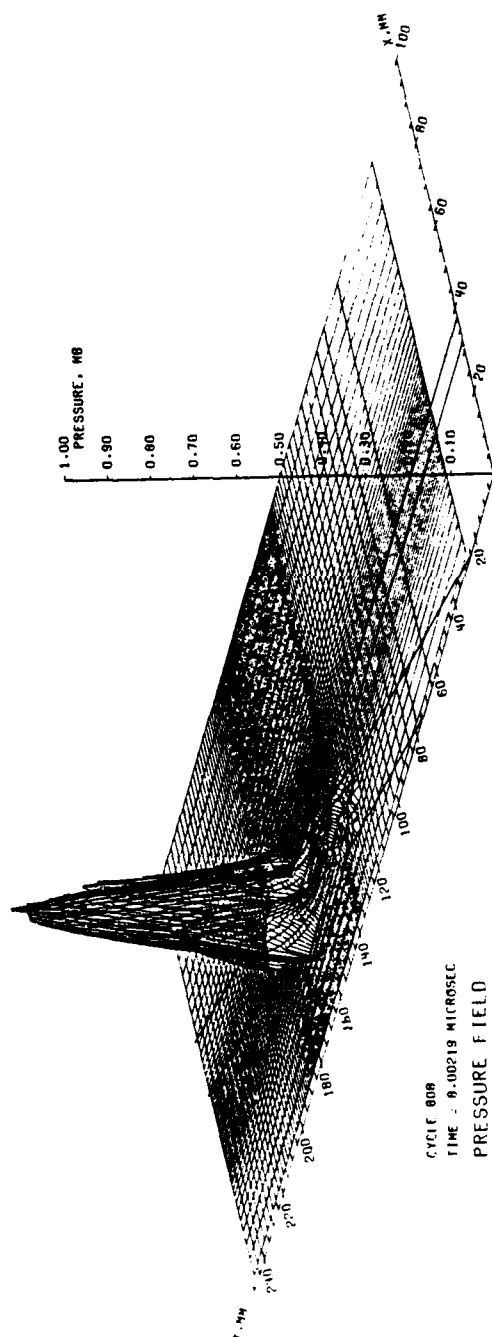


Figure 110. Pressure Field for 75° Oblique Impact

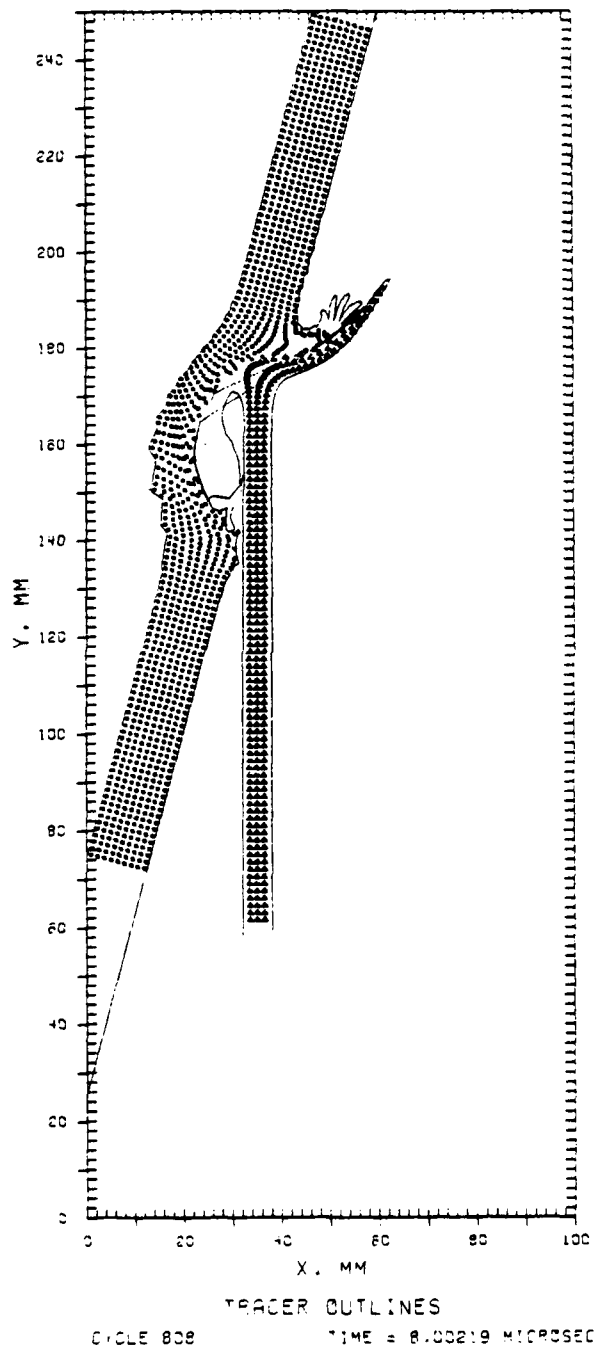


Figure 111. Penetrator-Target Deformation for 75° Oblique Impact

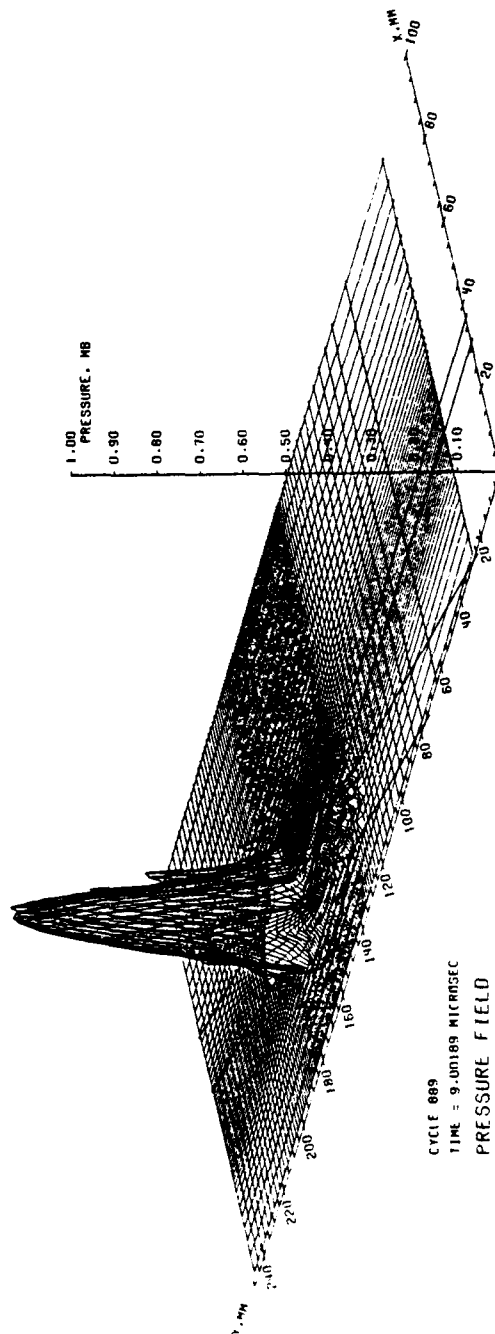


Figure 112. Pressure Field for 75° Oblique Impact

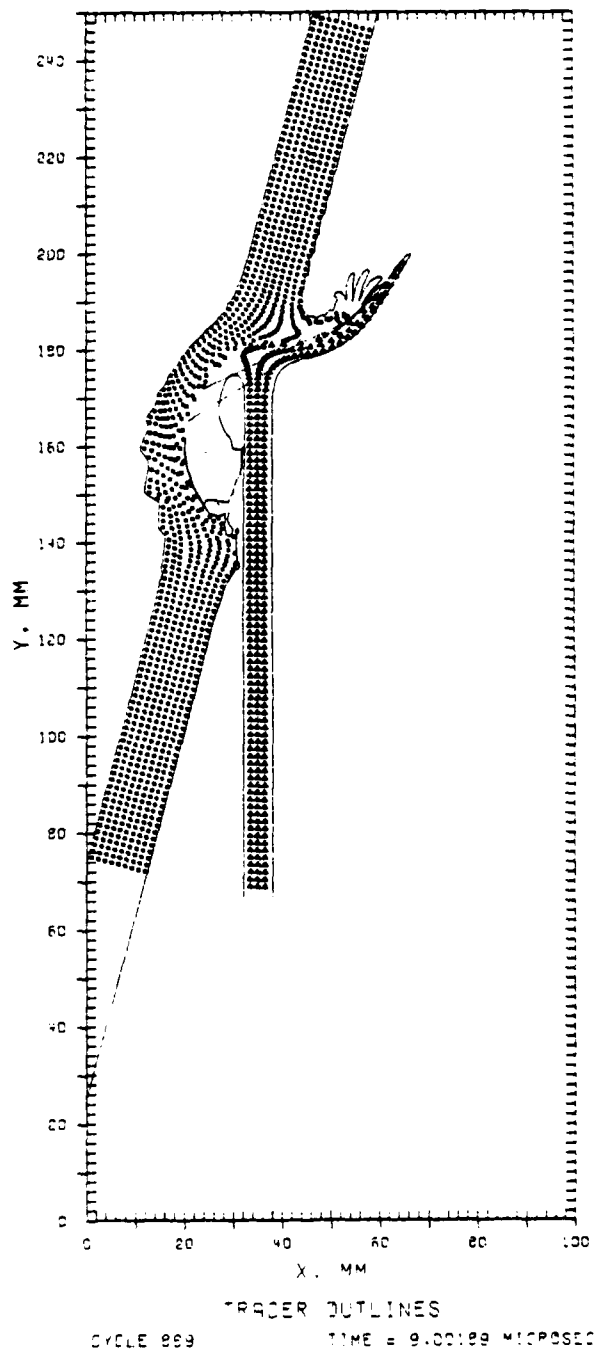


Figure 113. Penetrator-Target Deformation for 75° Oblique Impact

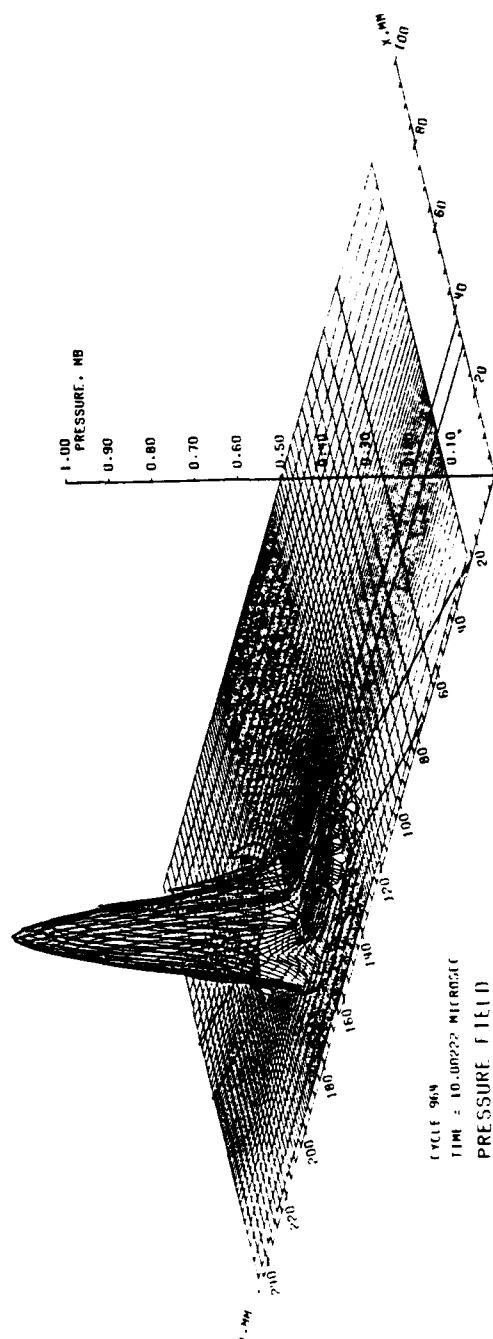


Figure 114. Pressure Field for 75° Oblique Impact

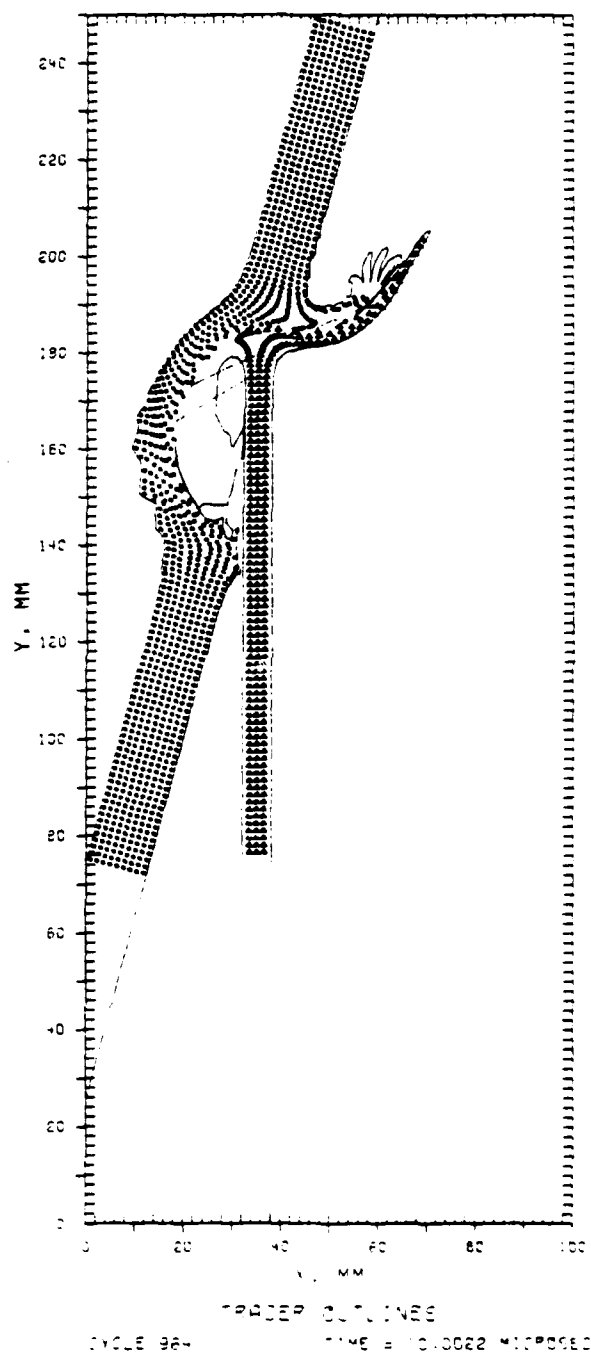


Figure 115. Penetrator-Target Deformation for 75° Oblique Impact

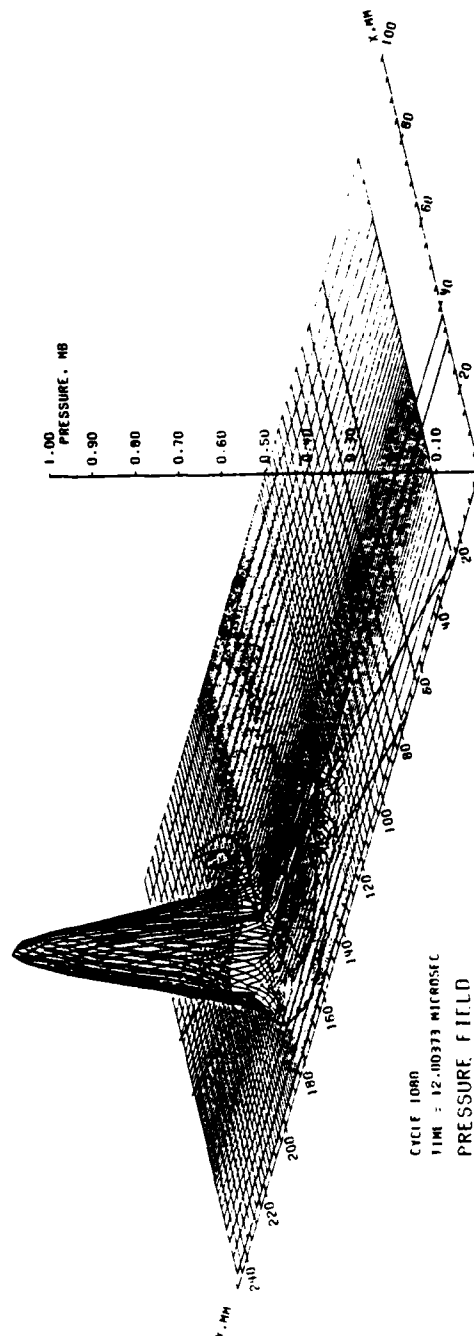


Figure 116. Pressure Field for 75° Oblique Impact

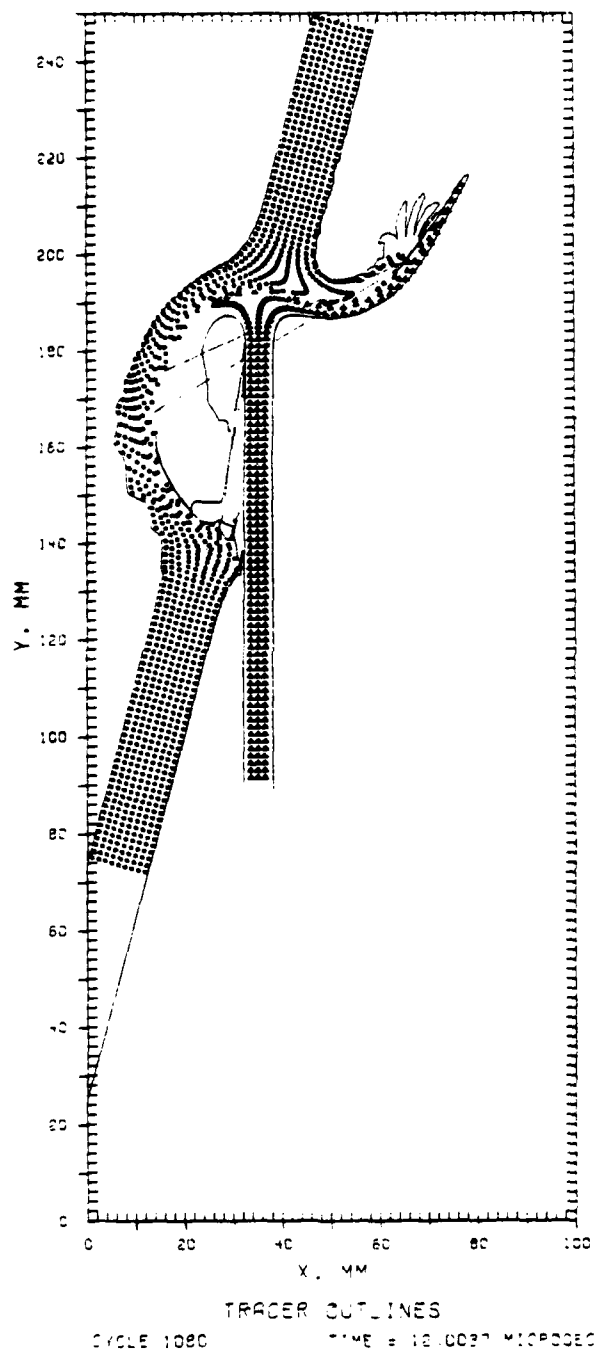


Figure 117. Penetrator-Target Deformation for 75° Oblique Impact

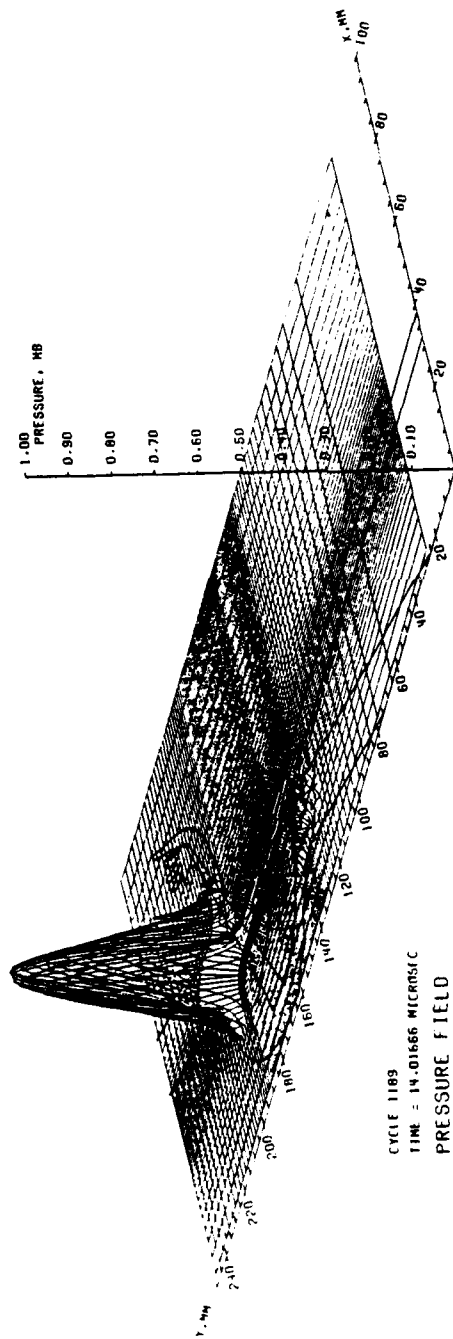


Figure 118. Pressure Field for 75° Oblique Impact

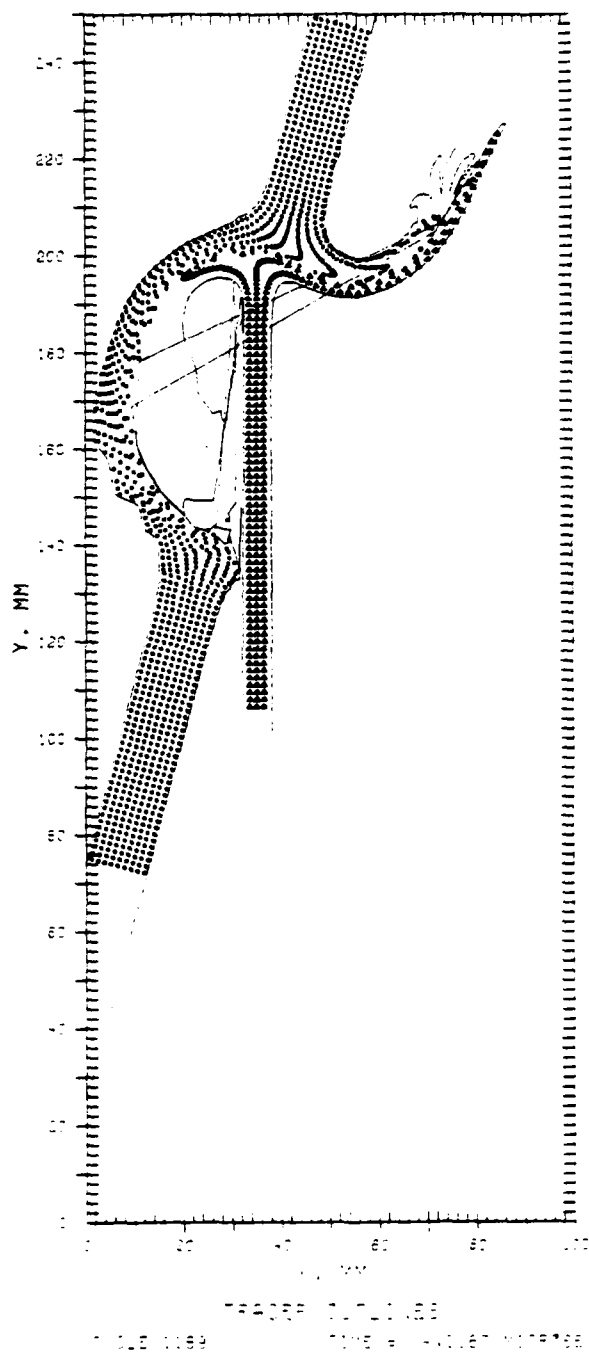


Figure 119. Penetrator-Target Deformation for 75° Oblique Impact

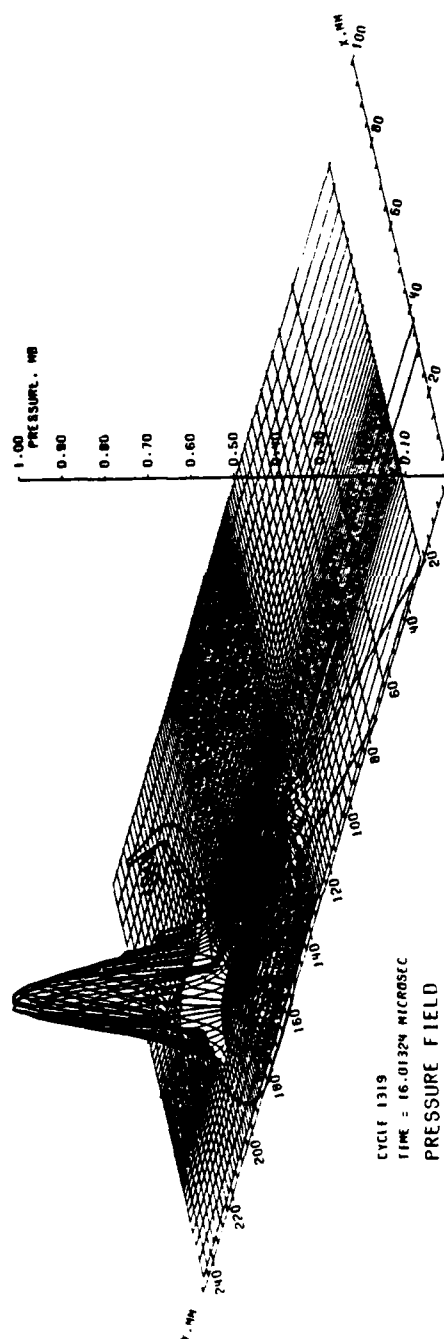


Figure 120. Pressure Field for 75° Oblique Impact

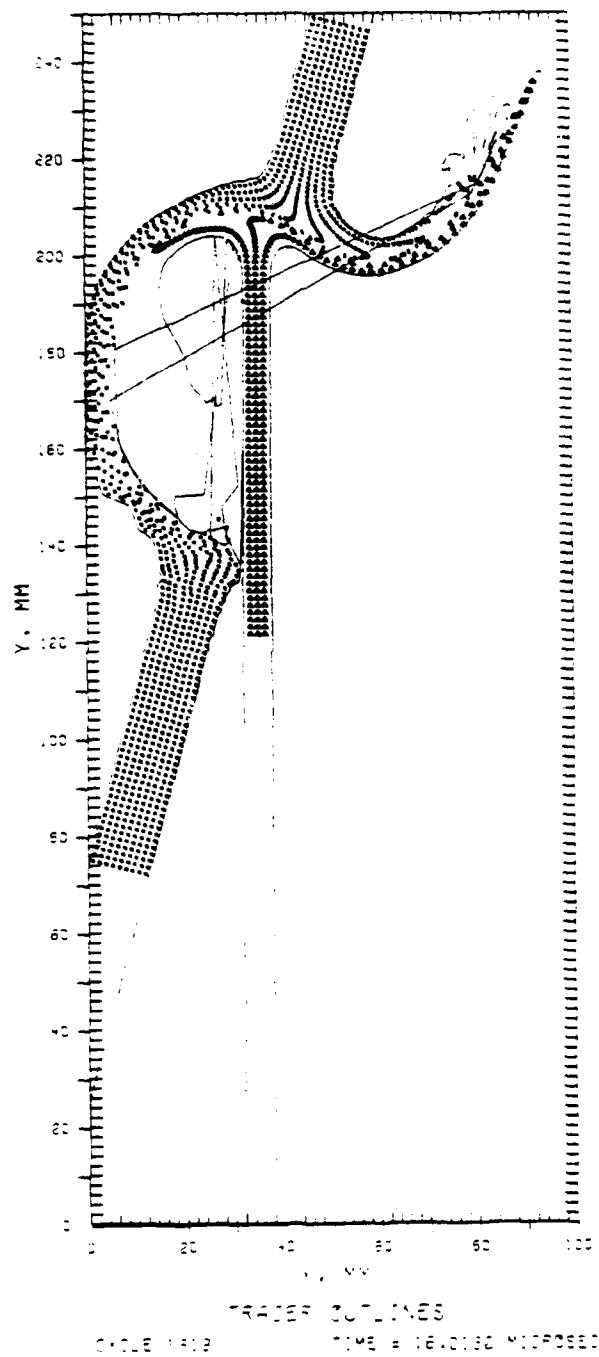


Figure 121. Penetrator-Target Deformation for 75° Oblique Impact

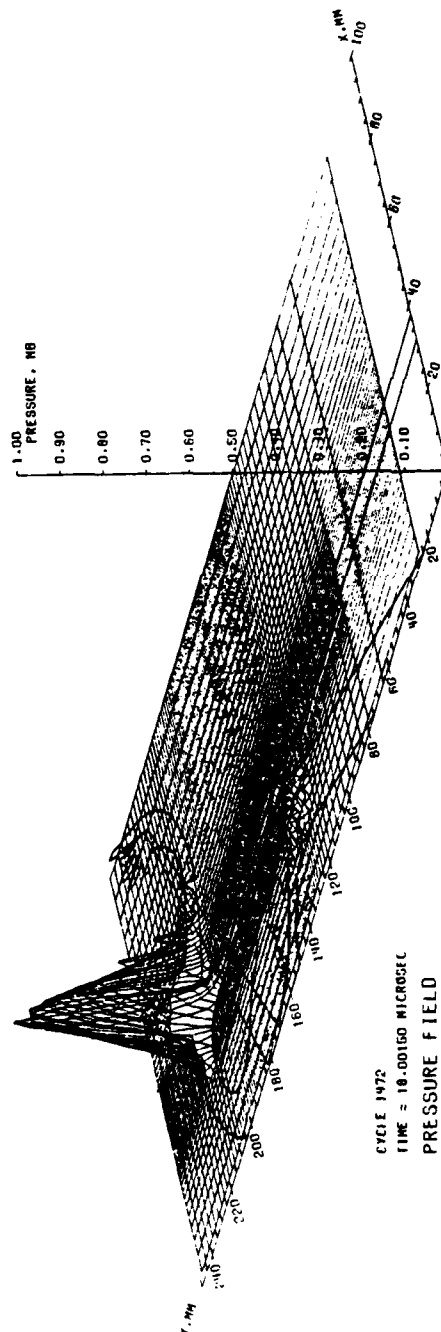


Figure 122. Pressure Field for 75° Oblique Impact

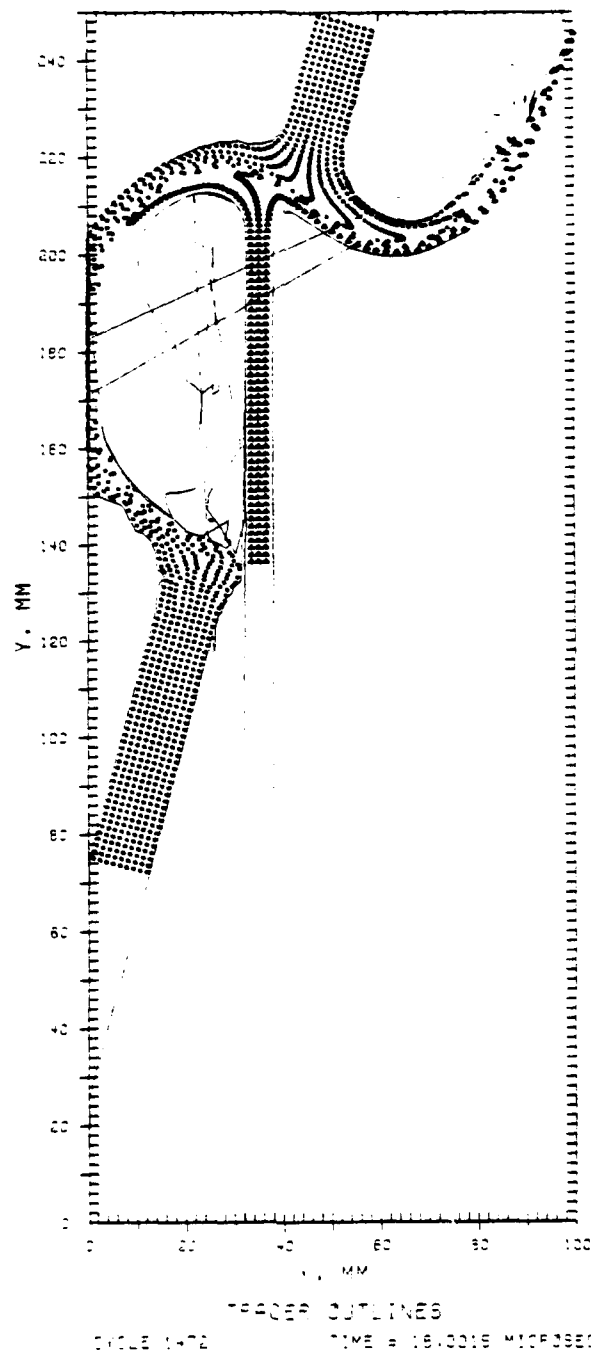


Figure 123. Penetrator-Target Deformation for 75° Oblique Impact

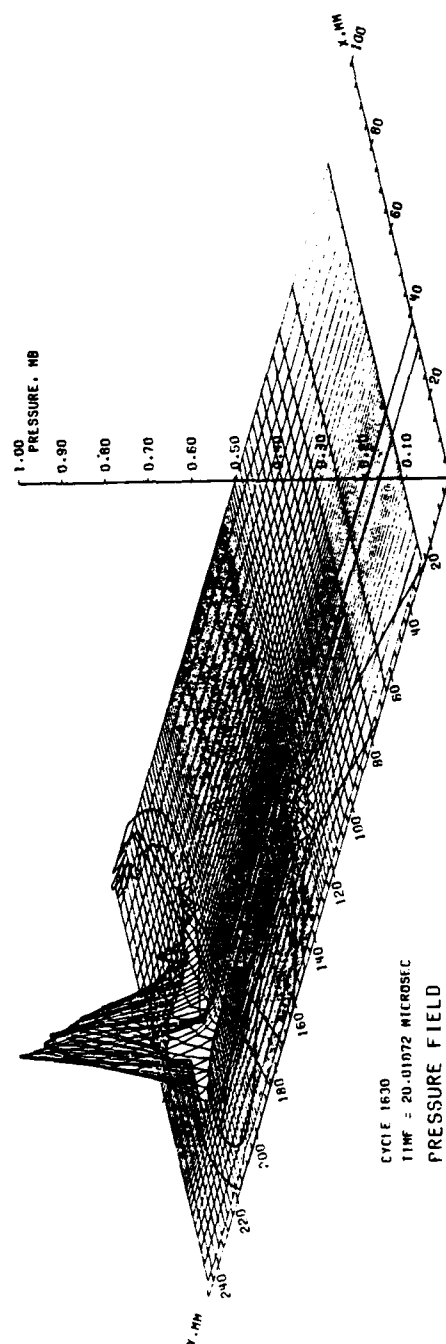


Figure 124. Pressure Field for 75° Oblique Impact

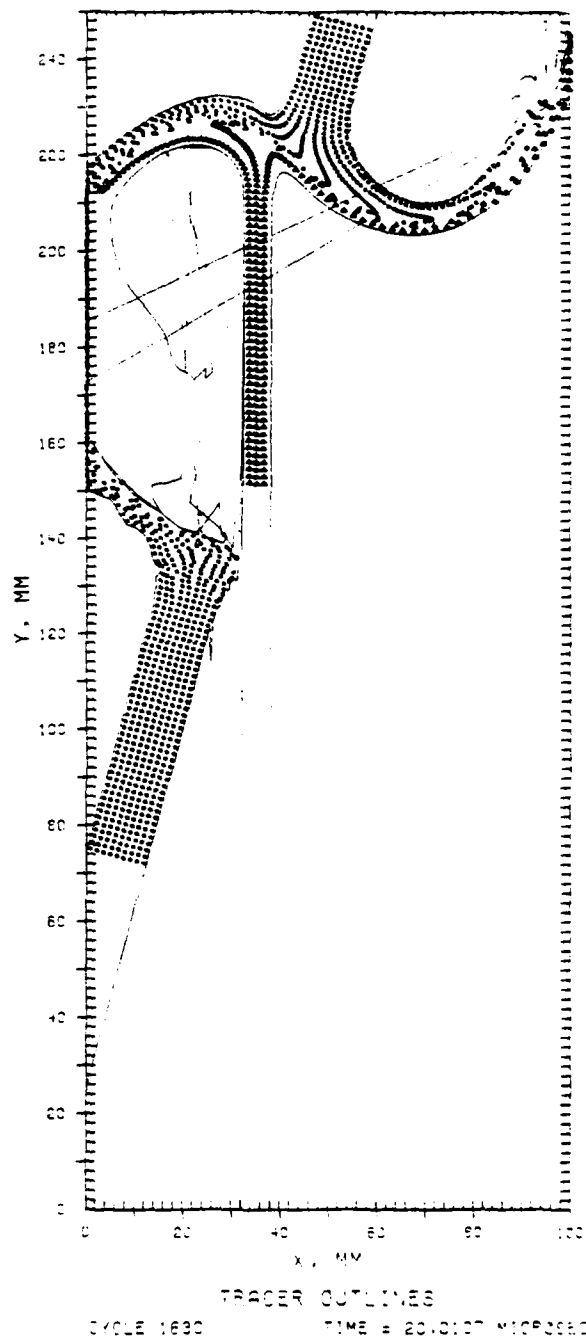


Figure 125. Penetrator-Target Deformation for 75° Oblique Impact

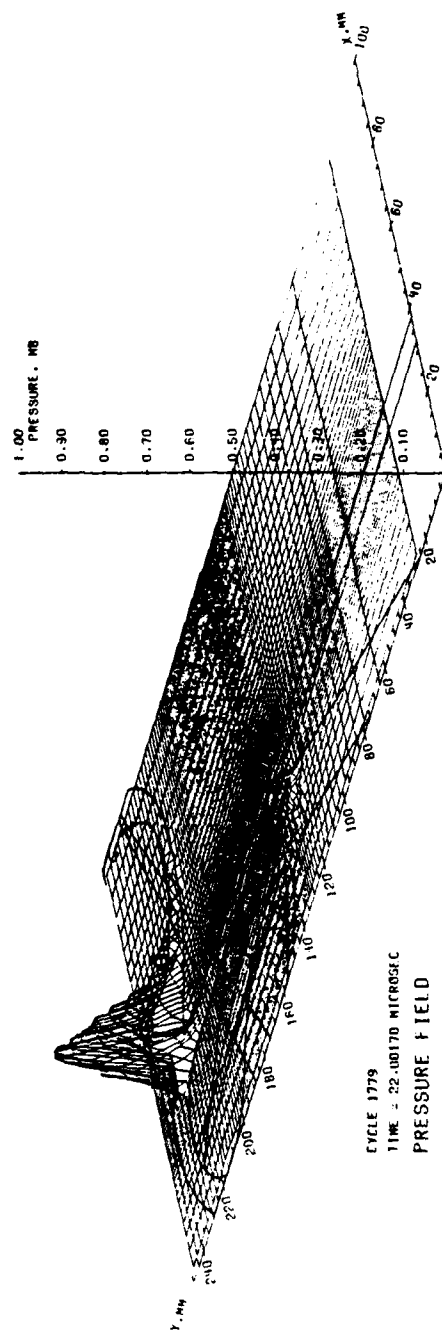


Figure 126. Pressure Field for 75° Oblique Impact

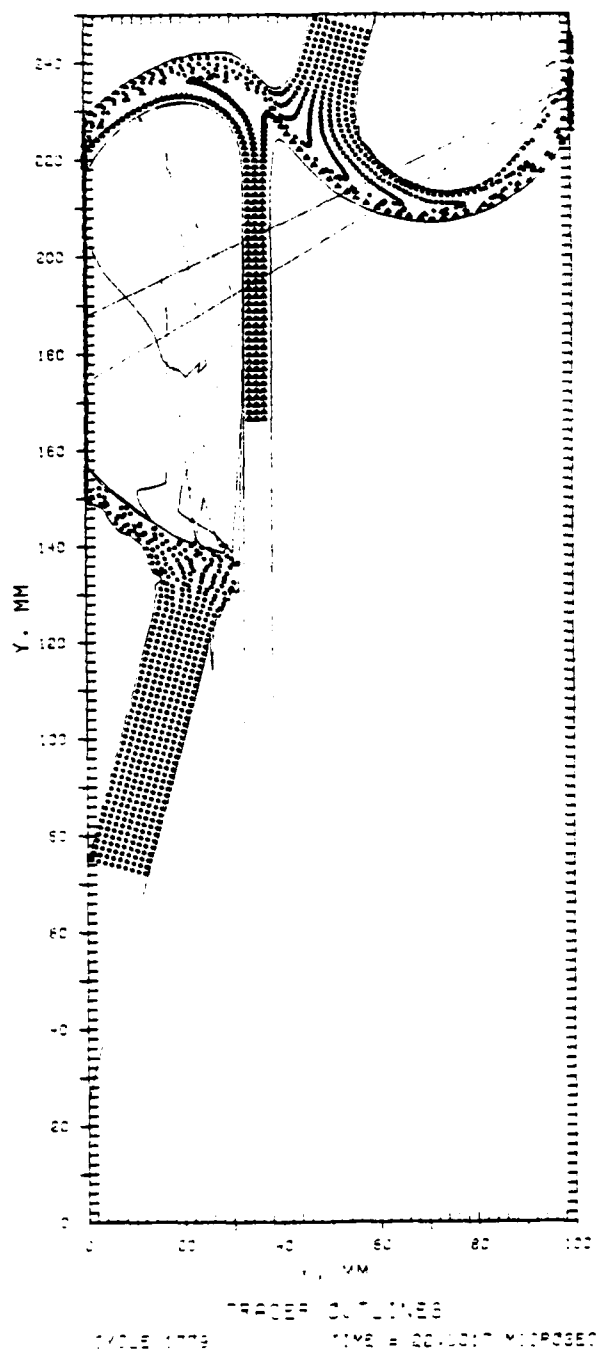


Figure 127. Penetrator-Target Deformation for 75° Oblique Impact

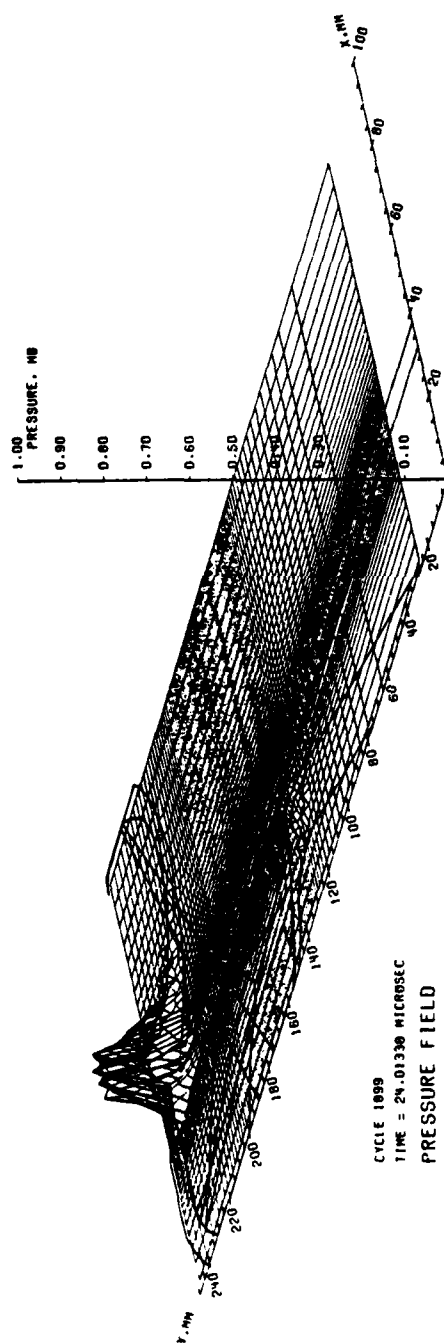


Figure 128. Pressure Field for 75° Oblique Impact

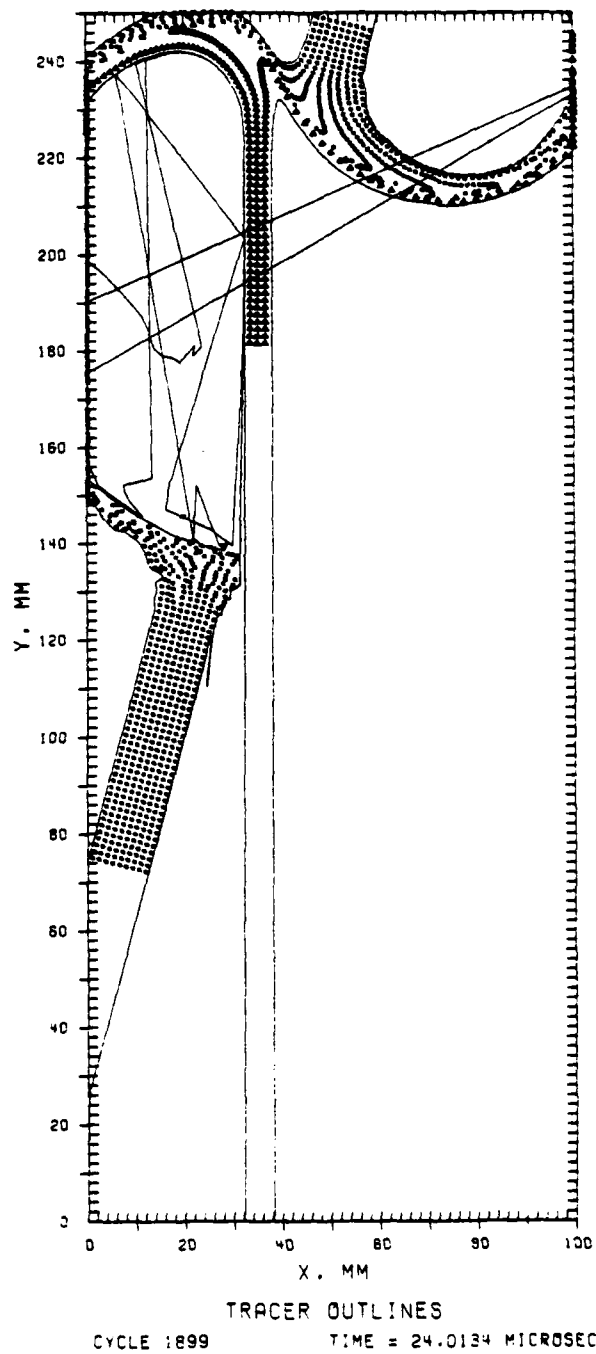


Figure 129. Penetrator-Target Deformation for 75° Oblique Impact

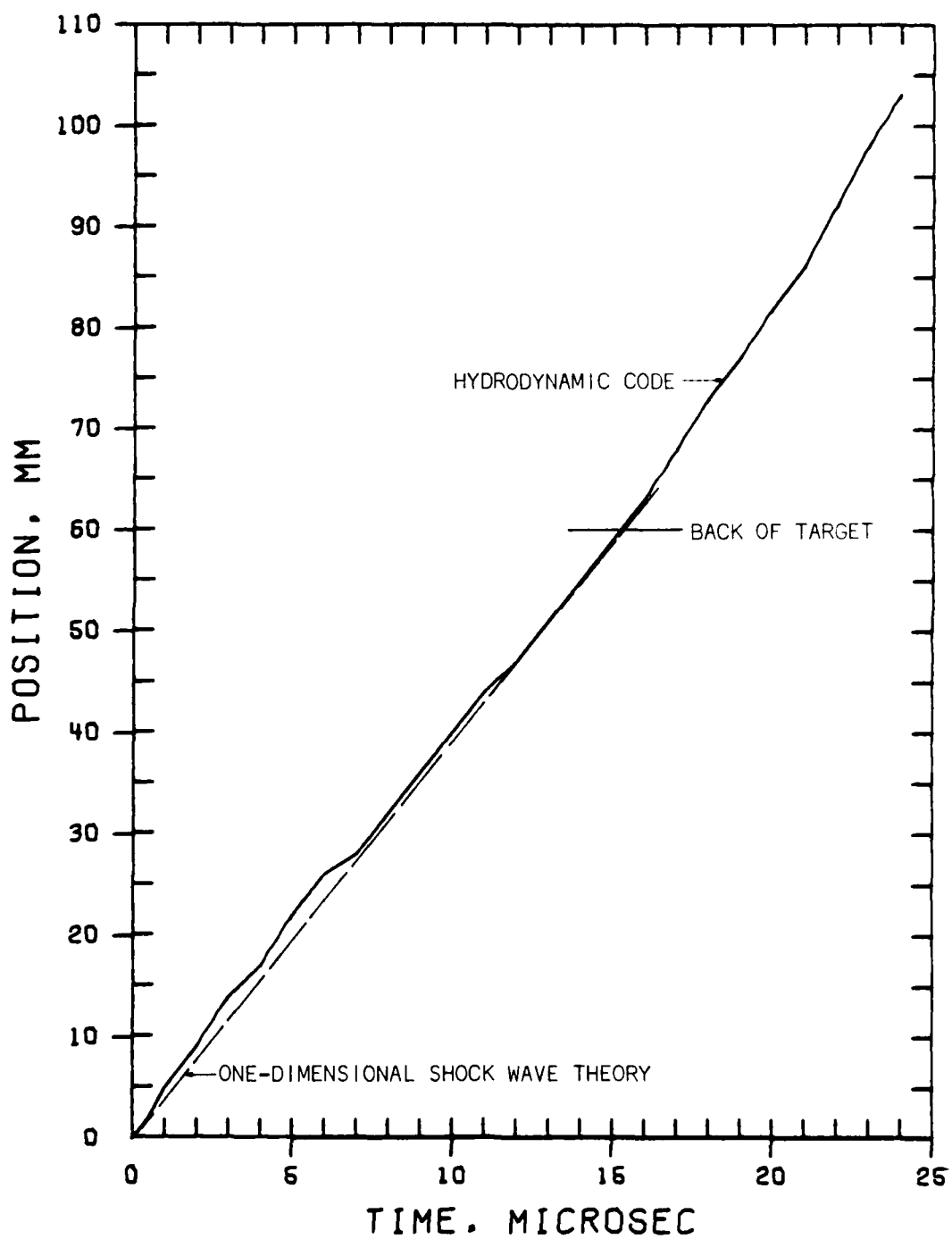


Figure 130. Penetration History for 75° Oblique Impact

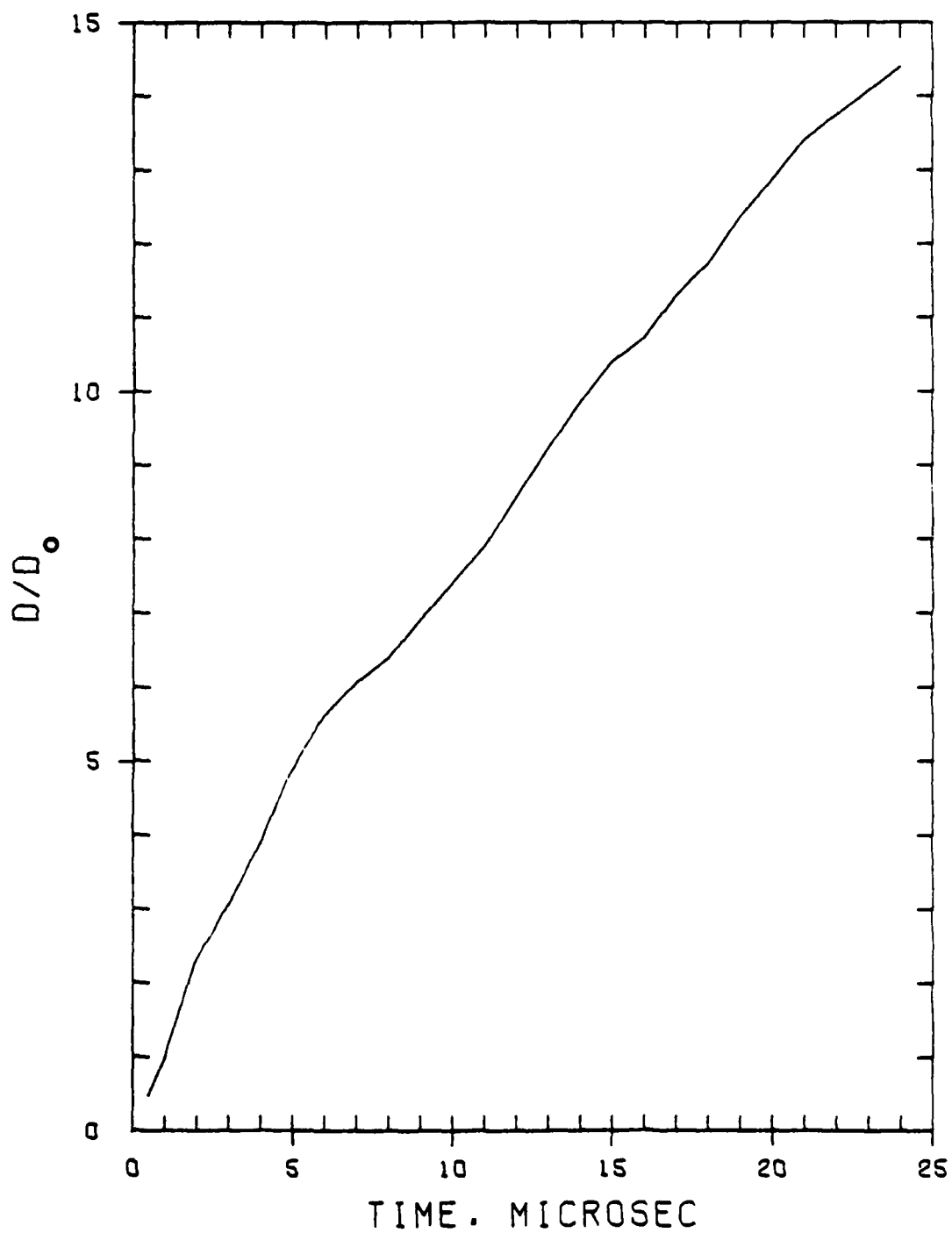


Figure 131. Growth of the Front Face Cut for 75° Oblique Impact

DISTRIBUTION LIST

<u>No. of Copies</u>	<u>Organization</u>	<u>No. of Copies</u>	<u>Organization</u>
12	Commander Defense Documentation Center ATTN: DDC-TCA Cameron Station Alexandria, VA 22314	1	Commander US Army Mobility Equipment Research & Development Cmd ATTN: DRDME-WC Fort Belvoir, VA 22060
1	Commander US Army Materiel Development and Readiness Command ATTN: DRCDMA-ST 5001 Eisenhower Avenue Alexandria, VA 22333	1	Commander US Army Armament Materiel Readiness Command ATTN: DRSAR-LEP-L, Tech Lib Rock Island, IL 61299
1	Commander US Army Aviation Research and Development Command ATTN: DRSAR-E 12th and Spruce Streets St. Louis, MO 63166	3	Commander US Army Armament Research and Development Command ATTN: DRDAR-TSS (2 cys) Mr. J. Pearson Dover, NJ 07801
1	Director US Army Air Mobility Research and Development Laboratory Ames Research Center Moffett Field, CA 94035	1	Commander US Army Harry Diamond Labs ATTN: DRXDO-TI 2800 Powder Mill Road Adelphi, MD 20783
1	Commander US Army Electronics Command ATTN: DRSEL-RD Fort Monmouth, NJ 07703	1	Commander US Army Materials and Mechanics Research Center ATTN: Tech Lib Watertown, MA 02172
1	Commander US Army Missile Research and Development Command ATTN: DRDMI-R Redstone Arsenal, AL 35809	1	Director US Army TRADOC Systems Analysis Activity ATTN: ATAA-SL, Tech Lib White Sands Missile Range NM 88002
1	Commander US Army Tank Automotive Research & Development Cmd ATTN: DRDTA-RWL Warren, MI 48090	1	Assistant Secretary of the Army (R&D) ATTN: Asst for Research Washington, DC 20310

DISTRIBUTION LIST

<u>No. of Copies</u>	<u>Organization</u>	<u>No. of Copies</u>	<u>Organization</u>
2	Chief of Naval Research Department of the Navy ATTN: Code 427 Code 470 Washington, DC 20325	1	US Air Force Academy ATTN: Code FJS-RL (NC) Tech Lib Colorado Springs, CO 80940
2	Commander Naval Air Systems Command ATTN: Code AIR-310 Code AIR-350 Washington, DC 20360	1	AFWL (SUL) Kirtland AFB, NM 87116
1	Commander Naval Ordnance Systems Command ATTN: Code ORD-0332 Washington, DC 20360	1	AFAL (AVW) Wright-Patterson AFB, OH 45433
1	Commander Naval Surface Weapons Center ATTN: DX-21, Lib Br. Dahlgren, VA 22448	1	AFLC (MMWMC) Wright-Patterson AFB, OH 45433
1	Commander Naval Surface Weapons Center ATTN: Code 730, Lib Silver Spring, MD 20910	1	Director National Aeronautics and Space Administration Langley Research Center Langley Station Hampton, VA 23365
1	Commander Naval Weapons Center ATTN: Code 45, Tech Lib China Lake, CA 93555	2	Director Lawrence Livermore Laboratory ATTN: Mr. M. Wilkins Dr. C. Godfrey P. O. Box 808 Livermore, CA 94550
1	Commander Naval Research Laboratory Washington, DC 20375	1	Computer Code Consultants ATTN: Mr. W. Johnson 527 Glencrest Drive Solana Beach, CA 92075
1	USAF (AFRDDA) Washington, DC 20330	3	Honeywell, Inc. Government and Aerospace Products Division ATTN: Mr. J. Blackburn Dr. G. Johnson Mr. R. Simpson 600 Second Street, NE Hopkins, MN 55343
1	AFSC (SDW) Andrews AFB Washington, DC 20331		

DISTRIBUTION LIST

<u>No. of Copies</u>	<u>Organization</u>	<u>No. of Copies</u>	<u>Organization</u>
1	Physics International Corp ATTN: Mr. L. Behrmann 2700 Merced Street San Leandro, CA 94577	1	Southwest Research Institute Dept of Mechanical Sciences ATTN: Mr. A. Wenzel 8500 Culebra Road San Antonio, TX 78228
1	Sandia Laboratories ATTN: Dr. L. Bertholf Albuquerque, NM 87115	2	University of California Los Alamos Scientific Lab ATTN: Dr. J. M. Walsh Tech Lib P. O. Box 1663 Los Alamos, NM 87545
1	Shock Hydrodynamics ATTN: Dr. L. Zernow 4710 Vineland Avenue North Hollywood, CA 91602		
1	Systems, Science, and Software ATTN: Dr. R. Sedgwick P. O. Box 1620 La Jolla, CA 92037		<u>Aberdeen Proving Ground</u> Marine Corps Ln Ofc Dir, USAMSAA
1	Drexel Institute of Technology Wave Propagation Research Center ATTN: Prof. P. Chou 32nd & Chestnut Streets Philadelphia, PA 19104		